1960

Monte Carlo determination of neutron capture distributions in thin iron and water regions

Clayton Wilbur Watson
Iowa State University

Mic 60-5895

WATSON, Clayton Wilbur. MONTE CARLO DETERMINATION OF NEUTRON CAPTURE DISTRIBUTIONS IN THIN IRON AND WATER REGIONS.

Iowa State University of Science and Technology
Ph.D., 1960
Physics, general

University Microfilms, Inc., Ann Arbor, Michigan

MONTE CARLO DETERMINATION OF NEUTRON CAPTURE DISTRIBUTIONS IN THIN IRON AND WATER REGIONS

by

Clayton Wilbur Watson

A Dissertation Submitted to the
Graduate Faculty in Partial Fulfillment of
The Requirements for the Degree of
DOCTOR OF PHILOSOPHY

Major Subject: Nuclear Engineering

Approved:

Signature was redacted for privacy.
In Charge of Major Work

Signature was redacted for privacy.
Head of Major Department

Signature was redacted for privacy.
Dean of Graduate College

Iowa State University
Of Science and Technology
Ames, Iowa

1960

TABLE OF CONTENTS

ABSTRACT

The accurate prediction of the spatial distribution of neutron capture rates in nuclear reactor shields and structural members is important in reactor design but, normally, is not possible with the usual mathematical techniques. Designers typically depend upon approximate methods bolstered by experiment and by previous experience.

Because of the probabilistic nature of the physical processes involved in the attenuation and capture of neutrons in reactor components, the Monte Carlo method offers a promising calculational tool with which to attack such problems. The present paper presents the methods used and the results obtained in a Monte Carlo study with an IBM-650 digital computer of the spatial distribution of neutron captures in a series of six alternating semi-infinite slabs of iron and water, from a neutron source located at one face of the slab array.

The capture data were obtained in the form $p(x)$ = the capture probability at the position x per unit x per incident source neutron, where x is the distance into the slab array as measured along the slab normal. The following functions were fitted to the capture probability data:

First layer in the array (an iron layer): $p(x) = \alpha e^{\beta x}$

Other iron layers: $p(x) = \alpha \cosh \beta(x-x_o)$

Water layers: $p(x) = A + Bx + Cx^2$

where x = zero at the left face of each layer. Empirical correlations of the parameters (α, β, x_o, A, B, C) were obtained as a function of source energy, between 0.01 Mev and 4.5 Mev, for two geometries: 1) all slab thicknesses equal ½", and 2) all slab thicknesses equal 1".

Large resonances in the iron total cross section affected the capture distributions. Streaming of neutrons through the iron layers and into the water layers occurred for source energies near the large 25 kev anti-resonance in the iron total cross section. The resulting increase in the thermalization rates led to increased capture rates in the array. A smaller, opposite effect (reduced capture rates) was observed for source energies near the positive resonance at 0.03 Mev in the iron total cross section.

The most important variables in determining the capture rates were the source energy and the thicknesses of the water layers. The capture distributions appeared to be relatively insensitive to changes in the source angular spectrum.

Reflection and transmission fractions were obtained as a function of source energy for the two geometries. The effect of the 25 kev anti-resonance in the iron total cross section was clearly evident in the reflection data. The angular distribution of the reflected neutrons closely approximated a cosine angular distribution, while the transmission angular spectra were somewhat more peaked in the forward direction.

Known physical characteristics of the attenuation and capture processes were used to improve the Monte Carlo estimates. The results obtained exhibited predictable qualitative characteristics to a very satisfactory degree. All of the features that would be expected in the capture curves, on the basis of physical considerations, were present in the final capture curves obtained.

The rigorous determination of the statistical uncertainty of the capture curves and correlations was not practical; however, upper limit estimates were obtained and these were small enough so that the results were considered to be meaningful.

It was found to be more efficient to feed the random input data into the IBM-650 on cards than to calculate these data internally. The random input data consisted of random digits from the RAND table of 1 million random digits, random exponential deviates from a table of 300,000 such deviates calculated for this study, and cosines of angles that are random on $(0, 2\pi)$, from a table of 150,000 such cosines calculated for this study.

INTRODUCTION

Energetic nuclear radiations emanate from the core of an operating nuclear reactor. A wide variety of difficult and often critically important reactor design problems is concerned with the attenuation and absorption of these radiations in shields to exclude the radiations from areas of the reactor plant in which they would be destructive to materials or dangerous to personnel.

Certain components of the plant must be subjected to high radiation levels because of their particular function in the reactor complex. Examples of such components include core structures, core-containing vessels, "thermal shields" which typically protect the core vessel from core radiations, and the various shield structures themselves.

The attenuation and absorption of nuclear radiations in these materials cause internal heating and attendant thermal stresses so that the determination of rates of absorption of nuclear radiations in reactor components, particularly in structural members, becomes quite important. The magnitude and spatial distribution of heating produced by nuclear radiations in these members must be determined accurately for efficient design.

The accurate prediction of radiation heating rates in reactor structural members is normally not possible with the usual mathematical techniques. This is particularly true if

the specific radiation field of concern is composed of neutrons, with various spectra of energy and direction of travel. No satisfactory method exists at present for calculating the distribution of neutrons in materials with dimensions that are small compared with the neutron mean free path in the material. This is the usual case in reactor structural members and certain shielding components, e.g. the thermal shields mentioned earlier. Designers typically depend upon approximate methods bolstered by experiment and previous experience.

Neutrons in a nuclear reactor deposit energy in (nonfissile) materials through which they pass by three mechanisms: (1) elastic collisions in which a portion of the neutron's kinetic energy is transferred to the nuclei of the medium by billiard-ball type collisions, (2) inelastic collisions in which part of the neutron's kinetic energy is transformed into excitation energy of the bombarded nucleus, which then decays to the ground state by emission of gamma rays, (3) capture of the neutron by the nucleus, the binding energy of the neutron being given off in the form of gamma rays. The energy involved in this latter so-called radiative capture reaction is usually larger than that in the other two reactions.

The neutron capture process is significant only at low neutron energies; however, low energy or "thermal" neutrons are predominant in most present-day reactors. Furthermore, most neutron shields depend, for their shielding effect, upon

lowering the energy of the incident neutrons to thermal values (moderation) whereupon the neutrons are captured by the shield media. Therefore, heating effects produced by neutron capture in reactor shields and structural members are of considerable importance in reactor technology.

The present study deals with the determination of neutron capture distributions in multiregion structures of iron and water. Iron was chosen for this study because of its obvious importance as a structural material. Water was chosen because of its widespread use in the reactor field both as moderator and as coolant. Iron and water are used together in such areas as: thermal shields, core structures, heat exchangers, and coolant and steam piping.

The difficulties encountered in attempting to describe the attenuation and capture of neutrons through thin multiregion configurations arise not in describing the microscopic processes that are involved, but rather in trying to predict the net macroscopic averages or effects of these microscopic processes. The types of interactions that a neutron may undergo in reactor materials are known, as are, for the most part, the probability distributions for changes in the state variables (position, energy, direction of travel) of a neutron at each interaction.[1] Mathematical difficulties arise when

[1]It should be pointed out that these microscopic probability laws for neutron interactions and accompanying state changes are the most that can be "known" about the transport of a neutron since the phenomena are entirely probabilistic in nature.

one tries to translate these random events into equations for predicting the average effects of many, many such events. These difficulties are compounded if the system being considered consists of several regions of different materials in which the microscopic probabilities (measured by the so-called interaction cross sections) vary with position as well as with the energy of the neutrons.

Because of the probabilistic nature of neutron interactions with matter, the Monte Carlo method offers considerable promise as a means of attacking difficult problems in neutron transport. Monte Carlo techniques have been used successfully in a number of such problems in the nuclear reactor field (1), (2), (3). The advent of larger and faster computing machines and increasing familiarity of workers in the field with the method may establish Monte Carlo as a standard calculational tool in nuclear reactor design.

The field of Monte Carlo originated during the early and mid 1940's apparently as a result of suggestions advanced by J. von Neumann and S. Ulam at Los Alamos. Virtually nothing appeared in the open literature concerning Monte Carlo until about 1949. In June of that year, the first symposium on Monte Carlo was held in Los Angeles under the sponsorship of the RAND Corporation and the National Bureau of Standards, with the cooperation of the Oak Ridge National Laboratory. The proceedings of that conference were published by the NBS

in 1951 (4).

Dr. A. S. Householder of ORNL makes the following statement concerning Monte Carlo in the foreword to these proceedings,

> "The Monte Carlo method may briefly be described as the device of studying an artificial stochastic model of a physical or mathematical process. The device is certainly not new. Moreover, the theory of stochastic processes has been a subject of study for quite some time, and the novelty in the Monte Carlo method does not lie here. The novelty lies rather in the suggestion that where an equation arising in a non-probabilistic context demands a numerical solution not easily obtainable by standard numerical methods, there may exist a stochastic process with distributions or parameters which satisfy the equation, and it may actually be more efficient to construct such a process and compute the statistics than to attempt to use those standard methods.
>
> "Simple and natural as this suggestion seems, once it is made, someone had to make it first in a voice loud enough to attract notice. The voices seem to have been chiefly those of Ulam and von Neumann, though Enrico Fermi . . . also contributed."

Many of the techniques found under the label of Monte Carlo in the literature are not new to statisticians. They have used similar methods for many years in survey sampling and model sampling procedures. Nevertheless, the field of Monte Carlo appears to have originated almost independently of the statisticians. A. W. Marshall in the introduction to the proceedings of a Monte Carlo symposium held at the University of Florida in 1954 (5) says,

> "The statisticians had . . . been using model sampling methods to investigate some of their problems . . . since the early 1900's. Their use of sampling reached a peak in the period 1925-1935 and

> then died off. However, their work was concerned with probabilistic problems so that they were not interested in the sort of thing which might lead to the original von Neumann-Ulam idea . . . . In any case the statisticians did not have the analogue idea and this is what got Monte Carlo in its current form started."

The field was dominated by the original analogue idea until about 1950. Since that time, there has been a relative decline in interest in the analogue solution of deterministic problems and an increase in the interest of the statisticians in the field of Monte Carlo. The field has been dominated in recent years by practical applications to problems with a probabilistic basis, typical of which are the particle diffusion problems. The usual procedure in these problems is to translate the functional equations describing the diffusion process back to a probabilistic basis as found in nature and then to simulate the diffusion process directly by stochastic methods. In the reference cited earlier (5), Marshall points out,

> "The most important practical applications thus far have had a probabilistic basis; the influence of the original Monte Carlo idea has been to suggest treating them directly as probabilistic problems rather than attempting a difficult, if not impossible, analytical solution. The translation and later retranslation of problems from probabilistic terms to non-probabilistic mathematical problems and back again has been by-passed."

Many references exist that describe both theoretical and applied work that has been done in the field of Monte Carlo (3), (4), (5), (6), (7), and no additional background will be

given here. Suffice it to say that the variety of problems that have been attacked with Monte Carlo and the ingenuity that has been displayed are impressive.

The present application of the Monte Carlo method is a direct stochastic simulation of a particle diffusion process, that of the diffusion and capture of neutrons in an assembly of alternating iron and water regions. The remainder of this paper will elaborate upon the details of the methods used, but a brief description of the basic approach is in order here.

A neutron is considered to be incident upon an array of iron and water slabs. A "history" or trajectory for this neutron through the assembly is calculated by specifying, via stochastic methods, the interactions of the neutron with the media and the changes in the state variables of the neutron at each such event. These specifications are made by random selection from the probability distributions describing each quantity. By generating many of these histories, usually with the aid of a high speed computer, one can simulate a low intensity experiment.

The potential advantages of such a simulation are obvious. Experiments that are too difficult or too expensive to perform in the laboratory may be readily amenable to study by simulation with the computer. Of equal importance is the ease with which parameters such as geometry and neutron energy may be changed in the computer program. This contrasts markedly with

the usual difficulty with which such changes are made in the laboratory.

Clearly, two things are essential for the success of the simulation. First, the number of histories must be large enough to be statistically meaningful and, secondly, the basic microscopic probability laws describing the processes involved must be known. It should be noted, however, that given these probability laws, there are no approximations in the calculations. Indeed, the method is inherently realistic, the only intrinsic limitation being the necessity of obtaining statistical significance in a reasonable amount of calculating time.

The machine employed in the present study was a basic IBM-650 digital computer with alpha device. This machine has a 2000 word memory of the magnetic drum type. Each word is of fixed length and contains ten digits plus a sign.

The array examined was that of Figure 1. The layers are semi-infinite, the only significant dimension being measured along the normal to the assembly. Thicknesses studied were in the range ½ to 3 inches.

The geometry of Figure 1 was chosen primarily as a concession to the limited capacity and speed of the computer that was used. The limitation of slab geometry is not considered to be serious. The results should have application to a variety of geometries that only approximate that of Figure 1 in an area of dimensions comparable to the neutron mean free path.

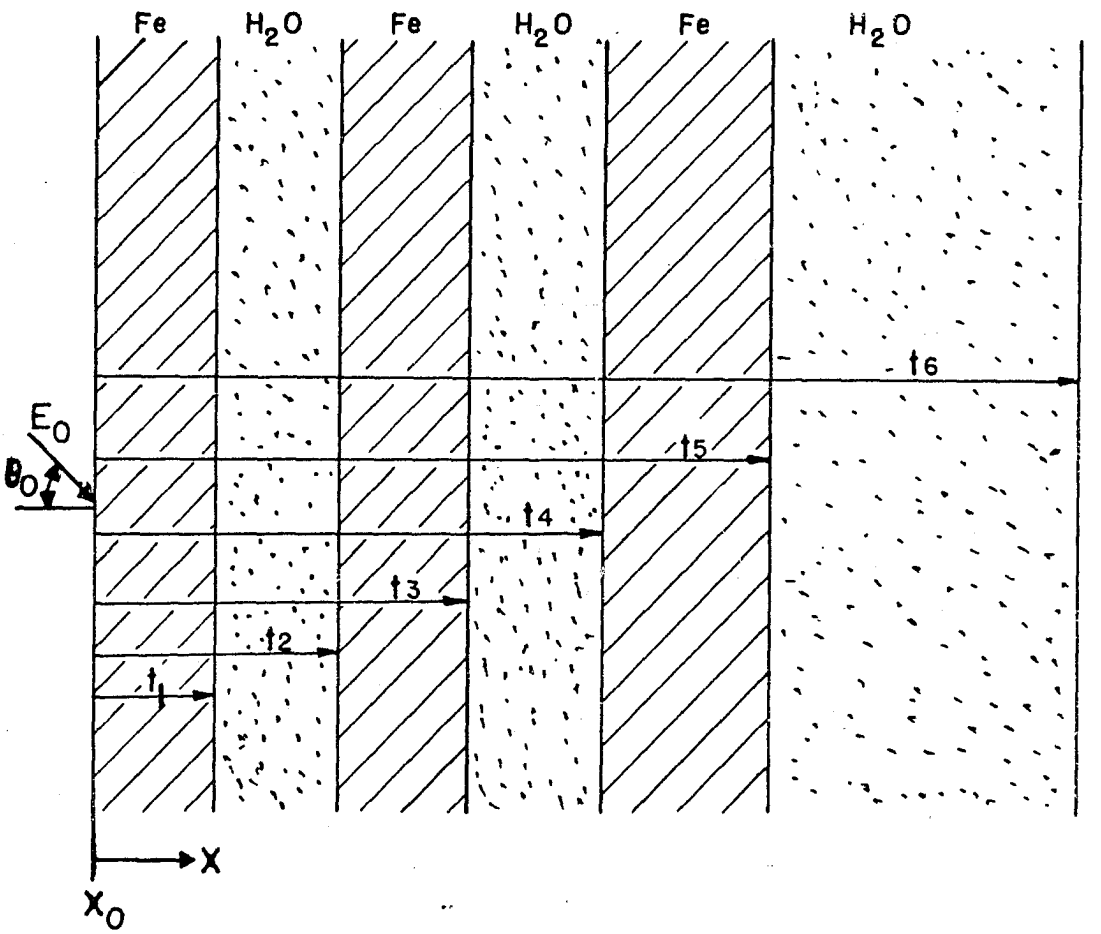

Figure 1. The basic configuration

SOLUTION OF NEUTRON TRANSPORT PROBLEMS

The usual mathematical methods of solving neutron transport problems are based upon the Boltzmann transport equation (8). The steady state form of this equation is:[1]

$$-\vec{\Omega}\cdot \operatorname{grad}_x f(E,\vec{\Omega},\vec{x}) - f(E,\vec{\Omega},\vec{x})\,[\Sigma_s(E,\vec{x}) + \Sigma_a(E,\vec{x})] + S(E,\vec{\Omega},\vec{x}) + \int dE'\,d\vec{\Omega}'\, f(E',\vec{\Omega}',\vec{x})\,\Sigma_s(E'\to E,\vec{\Omega}'\to\vec{\Omega},\vec{x}) = 0$$

where,

$f(E,\vec{\Omega},\vec{x})$ = the angular flux = number of neutrons in $d\vec{x}$ about $\vec{x}$, with energy in dE about E, and with velocity in the solid angle $d\vec{\Omega}$ about $\vec{\Omega}$ times the magnitude of the neutron velocity

m = the neutron mass

$\vec{x}$ = the position vector

$\vec{\Omega}$ = a unit vector in the direction of the neutron velocity

E = the neutron kinetic energy

Σ_s = the scattering cross section of the medium

Σ_a = the absorption cross section of the medium

$\Sigma_s(E'\to E,\vec{\Omega}'\to\vec{\Omega},\vec{x})$ = the cross section at $\vec{x}$ for scattering from E' to E and $\vec{\Omega}'$ to $\vec{\Omega}$

[1] It is assumed that the material is isotropic, i.e., that the cross sections do not depend upon the direction of the incident neutron.

$S(E, \vec{\Omega}, \vec{x})$ = the neutron source

A considerable simplification in this equation results if the neutrons are monoenergetic. The resulting monoenergetic steady state equation is

$$-\vec{\Omega} \cdot \text{grad}_x f(\vec{\Omega}, \vec{x}) - [\Sigma_s(\vec{x}) + \Sigma_a(\vec{x})] f(\vec{\Omega}, \vec{x}) + \int d\vec{\Omega}' f(\vec{\Omega}', \vec{x}) \Sigma_s(\vec{\Omega}' \rightarrow \vec{\Omega}, \vec{x}) + S(\vec{\Omega}, \vec{x}) = 0$$

Normally, one is concerned with a spectrum of neutron energies. The usual procedure is to divide the spectrum into a number of "groups' such that an effective energy and an effective set of the pertinent physical constants may be defined for each group as if there was no energy variation within the group. The monoenergetic transport equations for these groups are coupled in that neutrons leaving one group form part of the source for other groups. The resulting problem is that of solving this system of coupled equations.

The Boltzmann equation cannot, in general, be solved rigorously. A large variety of methods exists for obtaining approximate solutions to this equation for special cases. A few of these are described below.

Diffusion Theory

If the neutron angular flux is isotropic (which will be true only if the spatial variation of the flux is small; i.e., if there are no sources or boundaries within several mean free paths of the point in question and if the absorption cross sections are small), a scalar flux, ϕ, may be defined

for which Fick's law applies.

$$\vec{J} = -D \text{ grad } \phi$$

where $\vec{J}$ is the neutron current or the net rate of flow of neutrons in the direction of $\vec{J}$, and D is the neutron diffusion coefficient at $\vec{x}$.

Fick's law leads to the following relatively simple steady state diffusion equation (9):

$$\text{div } [D \text{ grad } \phi (\vec{x})] - \Sigma_a(\vec{x}) \phi (\vec{x}) + S(\vec{x}) = 0$$

or

$$D \phi(\vec{x}) - \Sigma_a(\vec{x}) \phi(\vec{x}) + S(\vec{x}) = 0$$

for a homogeneous medium.

Examples of assumptions that are often made (singly or in combination) in special cases to enable specific problems to be solved with diffusion theory are:

1) All scattering events are isotropic in the center-of-mass coordinate system.
2) The absorption cross sections are small.
3) The energy of a neutron is unchanged by scattering events.
4) No inelastic scattering is present.
5) Experimentally determined constants are used in the equations to obtain solutions to problems that are similar to the experimental problem.

These methods and approximations are used with varying degrees of success depending upon the particular application

and how closely the actual problem resembles the assumed problem.

A more rigorous form of the Boltzmann equation than is afforded by diffusion theory is necessary if the flux has a pronounced angular dependence. Again, assumptions such as are listed above lead to simplifications in specific cases and enable adequate solutions to be obtained in certain of these special problems.

A wide variety of numerical techniques has been devised for obtaining solutions to the Boltzmann equation. These methods are usually limited by convergence difficulties, i.e., by the computing time that is required. Two typical methods of this type are described below.

Spherical Harmonics Method (Higher Order Diffusion Theory)

The angular flux is expanded in a series of Legendre polynomials that terminates after n terms (P_n approximation). The resulting system of equations is usually solved by numerical methods to obtain the coefficients such that the expansion approximates the solution to the Boltzmann equation. The larger the number of terms in the expansion, the more accurate will be the resulting solution. Convergence is rather slow, and the computational work required increases rapidly as the number of terms in the expansion is increased. The method becomes unwieldy for difficult problems.

Carlson's S_n Method

In this method, the angular flux distribution is assumed to be a linear function of the cosine of the angle over each of n subintervals into which the cosine axis is divided. This makes it possible to integrate the Boltzmann equation, again with numerical methods, in a variety of problems. The computations again become prohibitively laborious for difficult problems.

All of the methods outlined above are unsatisfactory for the solution of the problem described earlier in this paper (thin iron and water layers). In this problem, the dimensions of the slabs are of the same order of magnitude as the mean free path of neutrons in the assembly, and the absorption cross section of iron is large. Hence, there will be a large spatial variation in the neutron flux and the flux will be markedly anisotropic. Furthermore, over much of the range of energies of concern, significant inelastic scattering occurs in iron, and elastic scattering in both iron and oxygen is highly anisotropic. In short, none of the commonly made assumptions in neutron transport theory are valid, and the solution of the problem with the usual mathematical methods is very difficult if not impossible. Solution of such problems is especially tedious with a machine such as the IBM-650.

The Monte Carlo method, while too laborious for use in solving problems in which the simpler approximate methods are

adequate, may be used to solve difficult problems with comparatively little more computing labor than for the simpler problems.

Thus, for the solution of relatively simple neutron transport problems, or in problems in which only very approximate answers are required, various of the approximate analytical methods are certainly superior to Monte Carlo. On the other hand, for complex neutron transport problems, the Monte Carlo method may offer a much more tractable or, indeed, the only available method for obtaining adequate answers.

DEFINITIONS OF PROBABILITY DENSITY FUNCTIONS - TRANSFORMATION OF RANDOM VARIABLES

Definitions

Random Variable - A random variable is a quantity that is associated with the outcome of a game of chance, or with an event of a specific class in such a manner that the random variable takes on a definite characteristic value for each possible outcome or event in the class.

For example, a random variable Z might be associated with the outcome of a toss of a die, where Z = the value of the up-turned face of the die. As another example, the value of a point selected at random from the interval (0, 1) of the real line could constitute a random variable.

Probability Density Function (Probability Distribution Function) - Associated with a random variable will be a probability density function giving the complete set of probabilities, P(A), for all of the possible values, A, that the random variable may assume.[1]

For the game of tossing a die, the probability density function is discrete, i.e., the possible outcomes are finite in number. In this instance (for a true die),

$$P(1) = P(2) = P(3) = P(4) = P(5) = P(6) = 1/6$$

In contrast, the number of points that may be selected at

[1]The definitions and equations presented in this section may be extended in a straightforward manner to multivariate distributions.

random from the interval (0, 1) is infinite. The corresponding density function is, therefore, continuous. The probability density function, p(x), for a continuously distributed random variable (or "variate"), X, is defined by

$p(x)dx$ = the probability that the random variable will take on a value lying in dx about x

where dx is a small increment of x.

The probability density function for a number selected at random from the interval (0, 1) is

$$p(x) = 1$$

(It should be noted that the integral of a probability density function over its range of definition, i.e., over all possible values of the random variable, must be equal to 1 since the probability of any outcome is 1.)

Cumulative Density Function - The cumulative density function is the integral (or the sum if the distribution is discrete) of the density function from the lower bound of definition to a specified value x. It gives, therefore, the probability that the random variable will take on a value that is less than or equal to x.

If $p(x) = 1$, $0 \leq x \leq 1$, the cumulative density function will be,

$F(x) = \int_0^x p(x')dx' = P(X \leq x) = x$ = the probability that a selected value, X, of the random variable will be less than or equal to x.

Transformation of Random Variables (10)

Consider a random variable, X, with probability density function $f(x)$, $a \leq x \leq b$. Assume that a second variate, Y, is defined by $Y = h(X)$, where h is a single-valued function of X such that a unique inverse $X = h^{-1}(Y)$ exists.

The probability density function, $g(y)$, for Y is given by,

$$g(y) = f\,[h^{-1}(y)]\,\frac{dh^{-1}(y)}{dy}$$

Now, since h gives a one-to-one correspondence between X and Y, it is clear that $P(X \leq x)$ is equal to $P(Y \leq y)$, where X is a specific sample from the population $f(x)$ and $y = h(x)$, $Y = h(X)$. Thus,

$$F(x) = \int_a^x f(x')dx' = \int_{h(a)}^y g(y')dy' = G(y)$$

If $g(y)$ is the uniform distribution,

$$g(y) = 1 \text{ for } 0 \leq y \leq 1$$

$$= 0 \text{ elsewhere}$$

we have

$$F(x) = \int_a^x f(x')dx' = \int_o^y dy' = y \qquad (1)$$

Equation 1 has been called the "Golden Rule" of Monte Carlo (2). Its utility lies in the fact that it may be used to select random samples from the distribution $f(x)$, provided that equation 1 can be solved for x.

Independent random samples are obtained easily from the uniform distribution, $g(y)$, by selecting random numbers from

the interval (0, 1) as mentioned earlier. Furthermore, for a given sample Y, G(Y) is just equal to Y and, by equation 1, Y is also equal to F(X) where $X = h^{-1}(Y)$. Thus, the solution of equation 1 for X supplies a random sample from a distribution with cumulative density function F(x), i.e., from the distribution with density function f(x).

This method does not necessarily constitute the most efficient means of selecting random samples from f(x), even if equation 1 can be solved for x. However, the "Golden Rule" contained in equation 1 has been used extensively in the Monte Carlo field, and its generality makes it a very useful tool.

The following example should serve to illustrate the method more clearly.

Consider the problem of selecting a random sample, X, from the exponential distribution,

$$f(x) = Ke^{-Kx} \quad 0 \leq x < \infty$$

We select a number, R, at random from the interval (0, 1) and substitute into equation 1 to get

$$\int_0^X Ke^{-Kx}dx = 1 - e^{-KX} = R$$

or

$$X = -\frac{\ln (1-R)}{K}$$

Note that (1 - R) is random on (0, 1) so that we could use equally well,

$$X = -\frac{\ln R}{K}$$

NOMENCLATURE

The symbols used in this paper are defined, for the most part, in the text and a given symbol may be used for several different quantities. Certain symbols are used rather consistently throughout the text, however. The following list of definitions for such symbols is included to avoid the necessity of redefining these symbols in detail at each appearance. In a few instances in the following list, a given symbol will have two definitions. The particular meaning to be attached will be clear from the text.

The cgs (centimeter-gram-second) system of units was used except where indicated otherwise. In general, the system of units being employed is not important in the derivations and in the discussions, and no units have been included in this list of definitions. (It is essential, of course, that a consistent set of units be used).

The following definitions will apply:

E_i = the kinetic energy of a neutron after the ith collision in a history

E_o = the neutron energy at the beginning of a history

k_B = the Boltzmann constant

M = the mass of a nucleus involved in a collision

m = the mass of the neutron

$p(x)$ = the probability density function for a continuously distributed random variable X; the capture

probability at the position x per unit distance per incident neutron

$P(A)$ = the probability that the event A will occur; the probability that the discretely distributed random variable being considered will take on the value A

T = absolute temperature

V = velocity

W_i = the neutron "weight" after the ith collision in a history

W_o = the neutron "weight" at the beginning of a history

x_i = the position, as measured along the normal to the slab array, of the ith collision in a history

x_o = the neutron position, as measured along the normal to the slab array, at the beginning of a history

$\sigma_a(E)$ or σ_a = the microscopic absorption cross section for neutrons of energy E

$\sigma_s(E)$ or σ_s = the microscopic scattering cross section for neutrons of energy E

$\sigma_{in}(E)$ or σ_{in} = the microscopic inelastic scattering cross section for neutrons of energy E

$\sigma_T(E)$ or σ_T = the microscopic total cross section for

neutrons of energy E

$\sigma_o(E)$ or σ_o = the microscopic total cross section of oxygen for neutrons of energy E

$\sigma_H(E)$ or σ_H = the microscopic total cross section of hydrogen for neutrons of energy E

$\sigma_{H_2O}(E)$ or σ_{H_2O} = the microscopic total cross section of a water molecule for neutrons of energy E

$\Sigma_B(E)$ or Σ_B = $n\sigma_B(E)$ or $n\sigma_B$ = the macroscopic cross section corresponding to the microscopic cross section σ_B, where B designates a specific type of cross section and n is the number of nuclei in the material per unit volume

ψ_i = the scattering angle in a neutron-nucleus collision as measured in the laboratory system of coordinates

ψ_i^* = the scattering angle in a neutron-nucleus collision as measured in the center-of-mass system of coordinates

θ_i = the angle between a neutron's velocity and the slab normal after the ith collision

E_{T_A} = the upper limit of the thermal energy range for nuclide A

A STRAIGHTFORWARD MODEL

Before proceeding to a description of the program used in this study, it will be instructive to examine a straightforward Monte Carlo simulation of the problem described in the introduction. The straightforward method, while so inefficient as to be impractical, embodies most of the basic features of the actual simulation that will be described later, and it will serve to introduce most of the relevant equations.

As mentioned earlier, random neutron paths or histories through the assembly being examined are calculated one by one, thereby simulating a low intensity experiment. If the number of such histories is large enough, one obtains statistically meaningful averages for the characteristics or effects that are being sought, e.g., collision densities, spectra, lifetimes, or, as in the present study, eventual fates.

The configuration to be studied is shown in Figure 1. The six slabs, with thicknesses defined by t_1 to t_6, are assumed to be infinite in the y and z directions, and distances along the direction normal to the array are measured by x.

Consider a neutron impinging upon the left face of this assembly and traveling with a velocity $\vec{V}_o$ directed at an angle θ_o to the slab normal and with corresponding energy E_o. The starting point will be given by $x = x_o$. The state of this neutron at any point in its travel through the slab array will be characterized by the three quantities:

x = the position of the neutron along the slab normal

θ = the angle that the neutron's velocity vector makes with the slab normal

E = the (kinetic) energy of the neutron

We wish to generate a random history for this neutron through the array so as to simulate the trajectory of an actual neutron impinging upon a real array and to determine the fate of the neutron and the values assumed by its state variables (position, energy, direction of travel) when the history terminates. To do this, we must specify the types and positions of the interactions that the neutron undergoes with the materials of the slabs and the changes in the state variables at each such collision. Each of these specifications is to be made in a completely random manner, subject only to the appropriate probability law in each instance.

To generate this history we proceed as follows:

1. Source. The neutron source is specified by assigning values to x_o, θ_o, and E_o. For example, assume that the source is isotropic (equal in all directions, i.e., the cosine of the emission angle is uniformly distributed between -1 and 1), monoenergetic, and located at the left face of the assembly of Figure 1. We set x_o = the coordinate of the left face, E_o = the source energy and $\cos \theta_o = R$, where R is a number selected at random on the interval (0, 1) (only neutrons with $\cos \theta_o > 0$ enter the assembly).

2. Distance Between Collisions (Appendix A). The distance, Δx_i, along the direction x to the next collision for a neutron with energy E_{i-1} and located at x_{i-1} is governed by the probability distribution,

$$p(\Delta x_i) = \frac{\Sigma_T(E_{i-1})}{\cos \theta_{i-1}} \; e^{-\Sigma_T(E_{i-1}) \; \Delta x_i / \cos \theta_{i-1}}$$

We select a value of Δx_i at random from this distribution by picking a random sample, Y_i, from an exponentially distributed population (Appendix A) and then calculate Δx_i from,

$$\Delta x_i = \frac{Y_i \cos \theta_{i-1}}{\Sigma_T(E_{i-1})}$$

The position of the next collision (i^{th} collision) is then given by,

$$x_i = x_{i-1} + \Delta x_i$$

We make the provision, however, that x_i must lie in the same slab as x_{i-1}, or in the first slab in the direction of the neutron's travel if x_{i-1} is located at a boundary of a region. If x_i lies past the next boundary, t_j, in the direction of travel, x_{i-1} is set equal to t_j and, the process is repeated using a new Y_i and the total cross section for the new region.

If x_i exceeds t_6 or is smaller than x_o, the neutron is considered to have been transmitted or reflected respectively. This fact is recorded, along with E_{i-1} and cos θ_{i-1}, and a new history is begun.

When an x_i is established that lies in the correct region with respect to x_{i-1} the i^{th} collision is considered to occur

at x_i.

3. Type of Interaction. Having determined the position of the i^{th} collision, the type of interaction at this point must be specified. The probability that an interaction of type A will occur is given by,

$$P(A) = \sigma_A(E_{i-1})/\sigma_T(E_{i-1})$$

where,

$\sigma_T = \sum_{\substack{\text{all} \\ k}} \sigma_k$ = the total microscopic cross section for the material

We must select each type of interaction with the proper probability.

For illustration, assume that the collision occurs in iron. The possible reactions at energies of interest here are radiative capture, inelastic scattering, and elastic scattering, with corresponding probabilities,

$\sigma_S(E_{i-1})/\sigma_T(E_{i-1})$ = probability for elastic scattering

$\sigma_{in}(E_{i-1})/\sigma_T(E_{i-1})$ = probability for inelastic scattering

$\sigma_a(E_{i-1})/\sigma_T(E_{i-1})$ = probability for radiative capture

where,

$$\sigma_T = \sigma_s + \sigma_{in} + \sigma_a$$

To select a type of interaction with the proper probability we select a number R at random on the interval (0, 1) and make the following specification, depending upon the value of R.

If $R < \frac{\sigma_S}{\sigma_T}$ we specify the interaction to be elastic scat-

tering, if $\frac{\sigma_S}{\sigma_T} < R < \frac{\sigma_S + \sigma_{in}}{\sigma_T}$ we specify inelastic scattering, and for $R > \frac{\sigma_S + \sigma_{in}}{\sigma_T}$ we specify radiative capture.

If we recall that, upon selecting a number R at random from (0, 1), the probability of obtaining a number that is less than or equal to some number k is just equal to k, then it is clear that each of the possible interactions is specified with the proper probability.

The interactions of concern in this study are capture, inelastic scatter, and elastic scatter in iron, and, in water, oxygen elastic scatter and hydrogen capture and elastic scatter. Radiative capture in oxygen is negligible.

4. Angle of Scatter. The angle of scatter is defined as the angle between the incoming and the outgoing velocity vectors of a scattered neutron. The probability distribution describing this quantity depends upon the incoming energy of the neutron, the type of scattering event, and the species of nucleus with which the interaction takes place. Those cases of interest here are, at energies above thermal, elastic scattering and inelastic scattering in iron, and elastic scattering in oxygen and hydrogen. At thermal energies only elastic scatter from iron, oxygen and hydrogen is important.

At energies of concern in this study, inelastic scattering in iron is approximately isotropic in the center-of-mass system of coordinates (11), as is elastic scattering in

hydrogen (12). Thus, for these events, we set

$$\cos \psi_i^* = 2R - 1$$

where R is random on (0, 1).

Elastic scatter in iron and oxygen at energies above thermal is not, in general, isotropic. The probability distribution for the cosine of the scattering angle in the center-of-mass system for anisotropic scattering events is given by a polynomial expansion (Appendix F),

$$p(\cos \psi_i^*) = \sum_{n=1}^{L} A_n (E_{i-1}) \cos^n \psi_i^*$$

A random cosine is selected from this distribution by a rejection technique due to von Neumann and outlined in Appendix I. This selection specifies the scattering angle in the center-of-mass system for such interactions.

For elastic scattering angles at thermal energies, see 8.

5. Azimuthal Scattering Angle. The azimuthal scattering angle, ϕ_i, is the angle through which the outgoing neutron's velocity vector is rotated about the incoming velocity vector. This angle is uniformly distributed from 0 to 2π. A table of random samples of cosines from a population of angles random on (0, 2π) has been prepared with a method due to von Neumann and described in Appendix J. A selection from this table specifies the cosine of the azimuthal scattering angle.

6. Angle with the Slab Normal of a Scattered Neutron's

Velocity Vector. The angle that a scattered neutron's direction of travel makes with the slab normal after collision i is given, at energies above thermal, by (Appendix E),

$$\cos \theta_i = \sin \psi_i \sin \theta_{i-1} \cos \phi_i + \cos \psi_i \cos \theta_{i-1}$$

Here, $\sin \theta_{i-1}$ and $\cos \theta_{i-1}$ are obtained from the previous collision, $\cos \phi_i$ is obtained as described in 5, and $\cos \psi_i$ is obtained from (Appendix D),

$$\cos \psi_i = \frac{1 + a \cos \psi_i^*}{\sqrt{1 + a^2 + 2a \cos \psi_i^*}}$$

where,

$$a = M/m = \text{mass of nucleus/neutron mass}$$

For thermal energy collisions, see 8.

7. Energy Change in Scattering Events. The energy change in an inelastic scattering event in iron is selected from a table of emission probabilities for inelastic scattering gamma rays. Seven of these tables have been prepared, depending upon the incident energy of the neutron. These tables were prepared from data compiled by Nuclear Development Corporation (13). The tables are described in detail in Appendix K. Selection of the energy change is made by means of a random number as described in 3.

For elastic scattering above thermal energies the energy change is given by (Appendices B and C),

$$\frac{E_i}{E_{i-1}} = \frac{1 + a^2 + 2a \cos \psi_i^*}{(1 + a)^2}$$

where a = M/m as in 6.

8. Events at Thermal Energies. For neutrons with energies below 1 or 2 electron volts the nucleus can no longer be considered to be at rest as at high energies (Appendix B). In addition, chemical binding effects become important, i.e., the nucleus is no longer effectively unbound. The determination of the scattering angles and energy changes in scattering events at thermal energies is consequently not a straightforward matter as at higher energies. Certain approximate methods must be employed.

In the present work, a method described by J. R. Triplett et al. at Hanford was used (14a). The method is described in detail in Appendices G and H. The results obtained by using this method appear to be adequate and are discussed in later sections of this paper.

Having established that a neutron's energy has been reduced to a value in the thermal range by a previous collision and that a scattering event takes place, the outgoing direction and energy are determined by the following equations,

$$E_i = \tfrac{1}{2} m V_e^2$$

$$\cos \Theta_i = \left[\frac{V(\alpha + a\alpha'')}{(1 + a)} + \Delta V \alpha'''\right] \Big/ Ve$$

$$V_e^2 = \frac{V^2 C^2}{(1 + a)^2} + (\Delta V)^2 + \frac{2V\Delta V}{1 + a} U$$

$$U = (\alpha + a\alpha'')\alpha''' + (\beta + a\beta'')\beta''' + (\gamma + a\gamma'')\gamma'''$$

$$C^2 = 1 + a^2 + 2a\mu$$

$$\mu = \cos \psi_i^* = \alpha\alpha'' + \beta\beta'' + \gamma\gamma''$$

$$a = M/m$$

$$\alpha = \cos \theta_{i-1}$$

$$\beta = 0$$

$$\gamma = \sin \theta_{i-1}$$

$$\alpha'' = 2R_1 - 1$$

$$\beta'' = \sqrt{1 - (\alpha'')^2} \sin \phi$$

$$\gamma'' = \sqrt{1 - (\alpha'')^2} \cos \phi$$

$$\alpha''' = 2R_2 - 1$$

$$\beta''' = \sqrt{1 - (\alpha''')^2} \sin \omega$$

$$\gamma''' = \sqrt{1 - (\alpha''')^2} \cos \omega$$

R_1 and R_2 = Random numbers from (0, 1)

ϕ and ω = Random angles from (0, 2π)

$$V^2 = \frac{2E_{i-1}}{m}$$

$$\Delta V = \sqrt{\frac{2k_B T}{M}} X_i$$

X_i = a variable selected from a probability table via the method of 3 (see Appendix G)

These procedures establish new state variables for a neutron having undergone collision number i. The calculations are repeated from collision to collision until the history is terminated by capture of the neutron by the media or by the neutron's having been reflected or transmitted. A tabulation of the number of captures as a function of x establishes a capture distribution in the array from a source of strength

equal to the number of histories calculated.

The angular spectrum, the energy spectrum, and number spectrum of reflected and transmitted neutrons are a by-product obtained from the calculations, provided that these have statistical significance.

THE STATISTICAL ESTIMATION TECHNIQUE

The straightforward method described in the previous section simulates exactly the transport and capture of neutrons through the array of Figure 1. Answers produced by this method will have large variances; i.e., large statistical uncertainty, because only the last collision contributes to the final answer. Many collisions must be calculated for each such contribution. This will be true to an even greater extent for relatively small arrays in which most histories terminate by reflection or by transmission. Thus a very large number of histories will be required to obtain statistically adequate results.

A method originated by von Neumann and his associates at Los Alamos during the 1940's may be used to decrease greatly the variance of the predicted capture rates. This method has been called "Statistical Estimation" (6) because an estimate of the answer is made at each collision.

In this method a weight, W_i, constituting a fourth state variable, is assigned to each neutron. This weight has value W_o at the beginning of a history. No capture events are considered to take place as in the straightforward method. Instead, all collisions are assumed to be scattering events. A neutron thus survives all collisions. It survives a given collision, i, however, with its weight reduced by a fraction equal to the nonsurvival probability at that collision.

$$W_i = W_{i-1}\left[1-\frac{\sigma_a(E_{i-1})}{\sigma_T(E_{i-1})}\right]$$

The x-axis is divided into n equal intervals, Δx_i, i = 1 to n. The weight decrease accompanying a collision in Δx_i is deposited in Δx_i. The total accumulation of such deposits in each Δx_i constitutes an estimate of the number of starting neutrons that can be expected to suffer capture in Δx_i.

By means of this technique, the "capture" of each neutron is distributed over many Δx_i intervals. Every history thereby makes many small contributions to the ultimate capture distribution instead of one large deposit as in the straightforward method. The resulting variances for a given number of histories are much smaller for the small deposits because of their larger number.

If the concept of fractional neutrons is disturbing, one can consider each history in the statistical estimation calculation as representing W_o starting neutrons which follow the same random path through the assembly. At each collision advantage is taken of the fact that the probable fraction of the neutrons entering the collision that will be captured, $p_i = \frac{\sigma_a(E_{i-1})}{\sigma_T(E_{i-1})} W_{i-1}$, is known exactly. One, therefore, knows the probable number of neutrons that will continue to the next collision and the probable number of neutrons that will be captured, i.e., the "weight" that will be deposited by the

collision. The accumulation of the deposited neutrons, or weights, in Δx_i divided by the total number of starting neutrons will be an estimate of the nonsurvival probability per neutron (capture probability) in Δx_i.

RUSSIAN ROULETTE

A neutron history in which statistical estimation is used to score the results, as described in the previous section, is clearly interminable. Some method must be used, therefore, to terminate histories. This must be done in such a way so as to leave the final results relatively unaffected.

One obvious manner in which this may be done is to terminate a history when the weight, W_i, reaches a value so low that any further contribution to the final results by that neutron may be neglected. This method is extremely inefficient, however. The same amount of computing time is required to reduce the weight of a neutron from 0.1 to 0.01 as is required to deposit the first 90% of the weight. Thus, most of the computing time is spent in calculating relatively unimportant low weight collisions.

A much more satisfactory method was originated by Ulam and von Neumann at Los Alamos. They called this technique Russian Roulette for reasons that will become clear shortly.

In the Russian Roulette method of terminating histories, the neutron is allowed to "play" a game of chance at all collisions after its weight is reduced to some pre-assigned value, W_R. The possible outcomes of the game are that the neutron survives with its weight increased or that the neutron "dies" at the point of the collision. The probability of survival and the weight increase for neutrons that survive are

specified so as to produce, on the average, the same total weight of continuing neutrons that would exist if the game was not played.

Two variations of Russian Roulette were used in this study. In the first, the neutron is allowed to continue with probability equal to W_i/W_o. If the neutron survives, its weight is set to W_o. The other variation terminates the history with a constant probability P. A surviving neutron in this instance has weight $W_i/(1-P)$. To select survival or "death" with the proper probability, a random number, R, is selected from the interval (0, 1) and compared with W_i/W_o (or 1-P as the case may be). The neutron survives if $R < W_i/W_o$ (or if $R < 1-P$ in the second variation).

The total weight of neutrons that survive the Russian Roulette game and continue their history is, on the average, unchanged from that in the low weight termination scheme described previously. This may be seen as follows.

Let the probability of termination be P. The probability of survival is 1-P. Now, if N neutrons reach W_R with weights W_i and Russian Roulette is not employed, the total weight of the neutrons that continue their histories is NW_i. All neutrons continue with weight W_i. With Russian Roulette, the average number of neutrons that survive is N(1-P), and these surviving neutrons will have weight $W_i/(1-P)$. The average total weight of surviving neutrons is, therefore, $N(1-P)W_i/$

$(1-P) = NW_i$. In other words, with Russian Roulette we process $N(1-P)$ neutrons with weight $W_i/(1-P)$ instead of N neutrons with weight W_i.

As may be obvious, introduction of Russian Roulette will increase the variance of the results somewhat. This is due to the reduction in the number of events at lower weights. However, the increased number of histories that will be required to produce the same statistical accuracy as with the low weight termination method will be compensated several-fold by the savings in computing time accomplished in avoiding most of the low weight calculations.

RANDOM INPUT DATA

The random input data for these calculations were of three types.

1) Random digits from the RAND table of one million random digits (14b).
2) Random exponential deviates from a table calculated for this project (Appendix A).
3) Cosines of random angles from the interval $(0, 2\pi)$ from a table calculated for this project (Appendix J).

As indicated, all of the random input data were pre-calculated. This information was read into the machine as needed by the program on standard IBM punched cards. This method is considerably faster with the IBM-650 than would be the generation of the random data internally during the course of the calculations.

Fifty thousand random input cards were prepared. Each of these cards contained the following:

Columns 1-30: six random exponential deviates in the form xx.xxx

Columns 31-44: two cosines of random angles in the form .xxxxxxx

Columns 45-75: 31 random digits (20 of which were used in the program).

Columns 76-80: serial number.

Between 15,000 and 30,000 of these cards were required

for each problem that was run. Each time that the supply of 50,000 cards was exhausted, the cards were put in a new random order by sorting on 3 or 4 of the unused random digits in each card and the cards were reused. This procedure was repeated for all of the calculations that were made.

In these calculations, approximately 1 to 1.3 input cards were required per collision, i.e., 0.03 to 0.05 seconds per collision were used for reading cards. This compares with approximately 1.3 to 2.0 seconds per collision required for the calculations. Calculation of the random input data internally would have required an estimated 0.4 to 0.6 additional seconds per collision.

Five random numbers may be required in the calculation of a given collision (these will be discussed later). The twenty random digits that were used from each card were employed as follows in supplying these five numbers.

R_0 = columns 49-54

R_1 = columns 45-54

R_2 = columns 55-64

R_3 = columns 60-64

R_4 = columns 59-64 + columns 51-54

With this assignment of the random digits, multiple use of a random digit in a given collision is kept to a minimum and rarely occurs.

THE PROGRAM

The program that was used in this project was written in fixed point basic machine language and was optimized throughout. The flow sheets describing the program are given in Figures 2 to 7. These will be described in order.

Figure 2 - Initialization.

The parameters that define the specific problem to be run are punched into three cards (identified by a 12 punch in column 3).

Card 1.

Columns 1-10: t_1 = xxx.xxxxxxx cm

Columns 11-20: t_2 = xxx.xxxxxxx cm

Columns 21-30: t_3 = xxx.xxxxxxx cm

Columns 31-40: t_4 = xxx.xxxxxxx cm

Columns 41-50: t_5 = xxx.xxxxxxx cm

Columns 51-60: t_6 = xxx.xxxxxxx cm

Columns 61-70: x_o = xxx.xxxxxxx cm

Columns 71-80: $\cos \theta_o$ = xx.xxxxxxxx

Card 2.

Columns 1-10: $t_2 - t_1$ = xxx.xxxxxxx cm

Columns 11-20: $t_3 - t_2$ = xxx.xxxxxxx cm

Columns 21-30: $t_4 - t_3$ = xxx.xxxxxxx cm

Columns 31-40: $t_5 - t_4$ = xxx.xxxxxxx cm

Columns 41-50: $t_6 - t_5$ = xxx.xxxxxxx cm

Columns 51-60: W_o = xx.xxxxxxxx

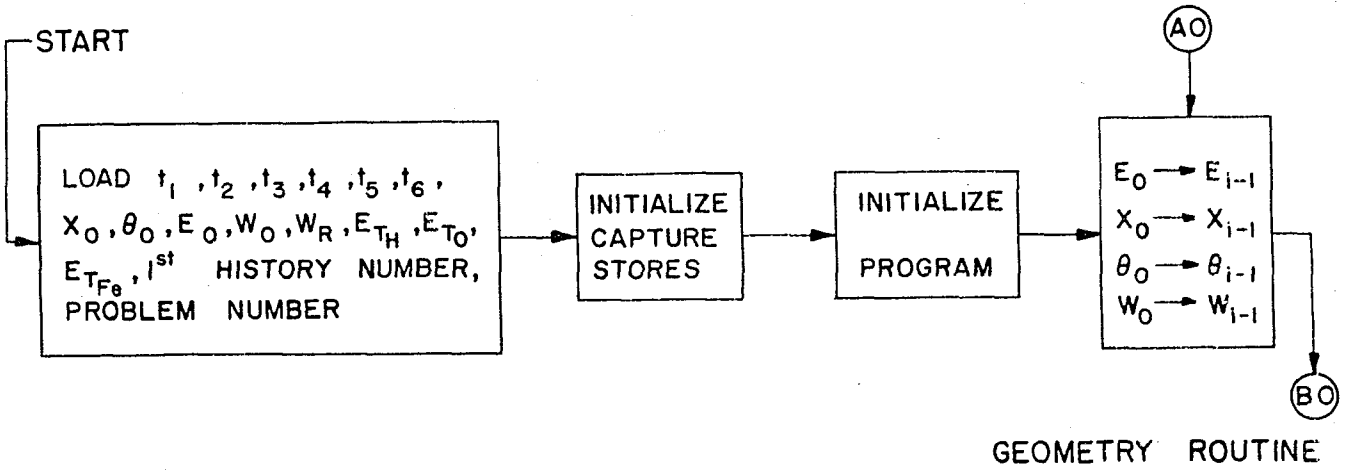

Figure 2. Initialization

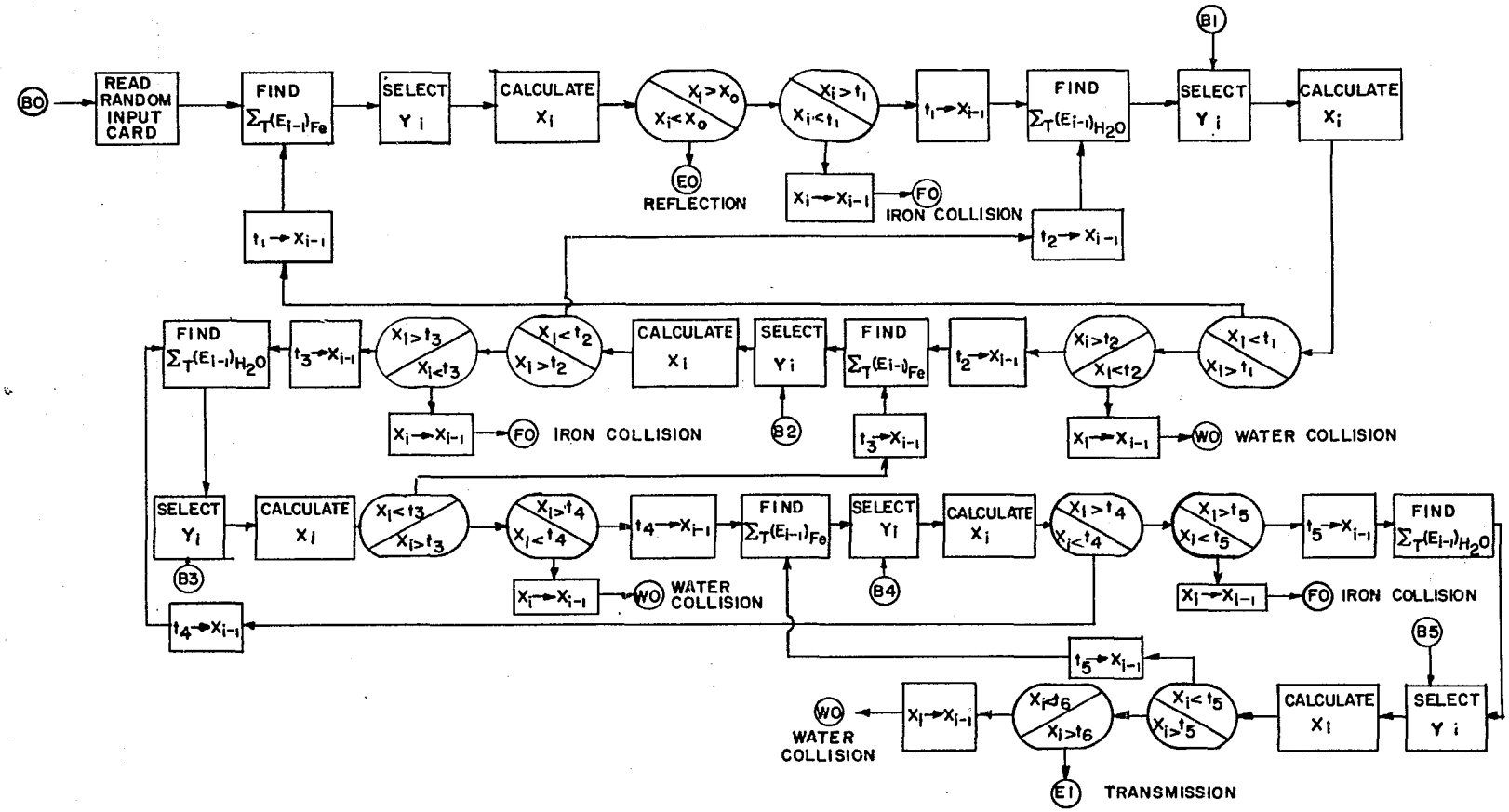

Figure 3. Geometry routine

Figure 4. Iron collision

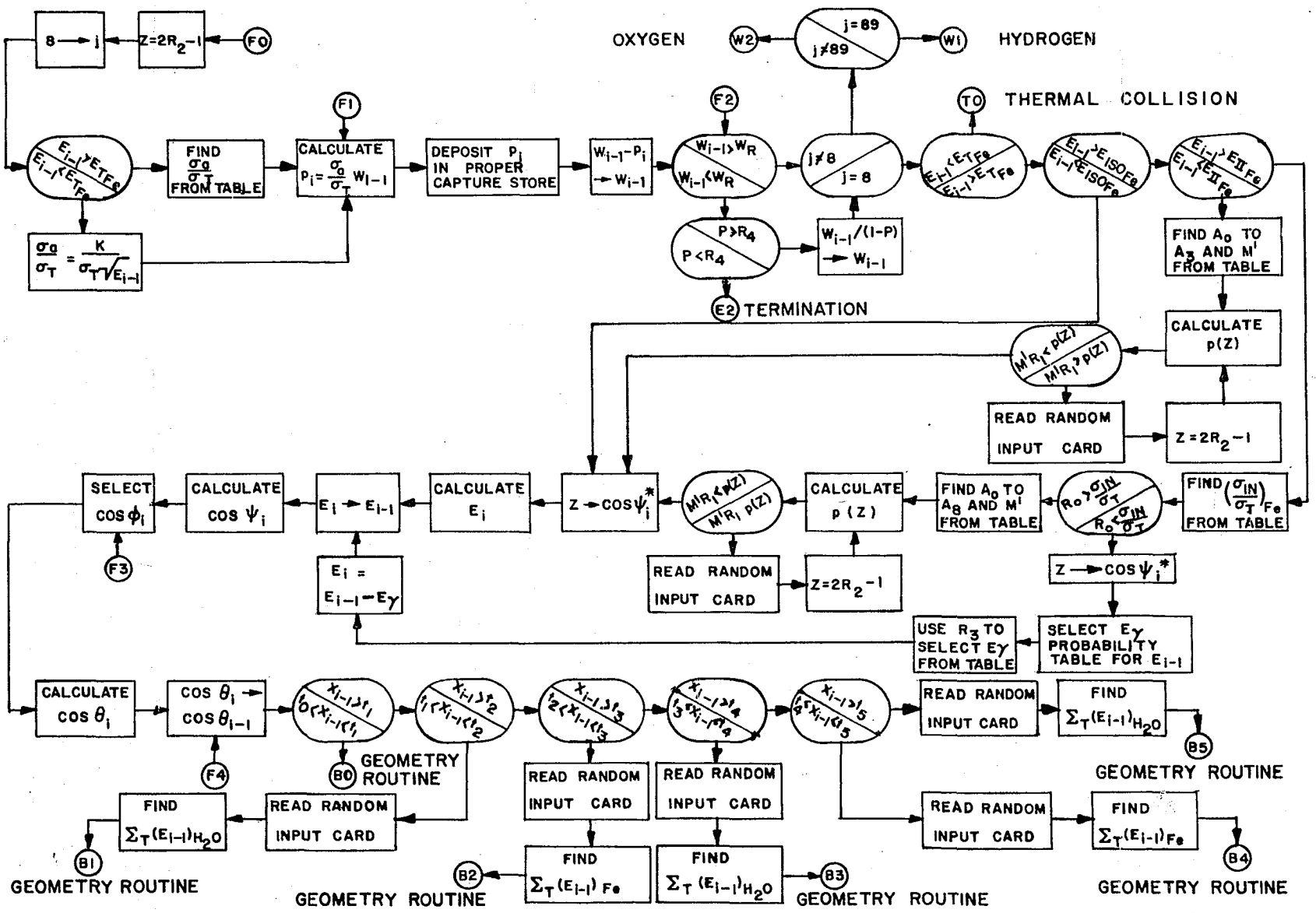
8 → i
Z=2R2-1
F0
OXYGEN
W2
j=89
j≠89
Wi
HYDROGEN
F1
F2
T0
THERMAL COLLISION
FIND σa/σT FROM TABLE
CALCULATE Pi = σa/σT Wi-1
DEPOSIT Pi IN PROPER CAPTURE STORE
Wi-1 - Pi → Wi-1
Wi-1 > WR
Wi-1 < WR
j≠8
j=8
Ei-1 < ET Fe
Ei-1 > ET Fe
Ei-1 > EISOFe
Ei-1 < EISOFe
Ei-1 > EΠFe
Ei-1 < EΠFe
σa/σT = K/(σT √Ei-1)
P > R4
P < R4
Wi-1/(1-P) → Wi-1
E2 TERMINATION
FIND A0 TO A3 AND M' FROM TABLE
CALCULATE p(Z)
M'R1 < p(Z)
M'R1 > p(Z)
READ RANDOM INPUT CARD
Z = 2R2 - 1
SELECT cos φi
CALCULATE cos ψi
Ei → Ei-1
CALCULATE Ei
Z → cos ψi*
M'R1 ≤ p(Z)
M'R1 > p(Z)
CALCULATE p(Z)
FIND A0 TO A8 AND M' FROM TABLE
R0 > σIN/σT
R0 < σIN/σT
FIND (σIN/σT)Fe FROM TABLE
F3
Ei = Ei-1 - Eγ
READ RANDOM INPUT CARD
Z=2R2-1
Z → cos ψi*
USE R3 TO SELECT Eγ FROM TABLE
SELECT Eγ PROBABILITY TABLE FOR Ei-1
CALCULATE cos θi
cos θi → cos θi-1
b0 < Xi-1 < t1
t1 < Xi-1 > t2
t2 < Xi-1 < t3
t3 < Xi-1 < t4
t4 < Xi-1 < t5
Xi-1 > t5
READ RANDOM INPUT CARD
FIND Σ T (Ei-1) H2O
B5
GEOMETRY ROUTINE
F4
B0
GEOMETRY ROUTINE
FIND Σ T (Ei-1) H2O
READ RANDOM INPUT CARD
B1
GEOMETRY ROUTINE
READ RANDOM INPUT CARD
READ RANDOM INPUT CARD
FIND Σ T (Ei-1) Fe
FIND Σ T (Ei-1) H2O
B2
GEOMETRY ROUTINE
B3
GEOMETRY ROUTINE
READ RANDOM INPUT CARD
FIND Σ T (Ei-1) Fe
B4
GEOMETRY ROUTINE

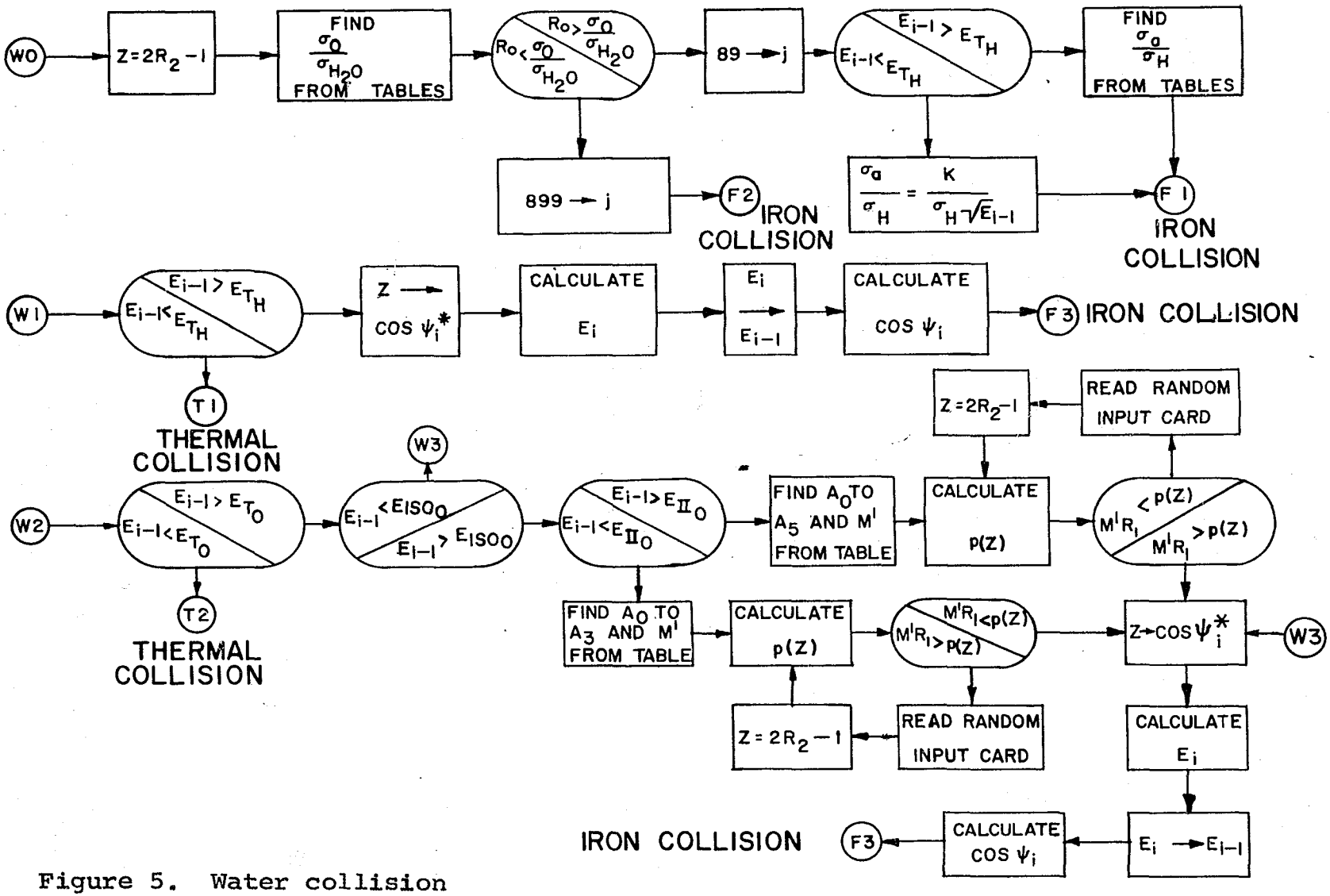

Figure 5. Water collision

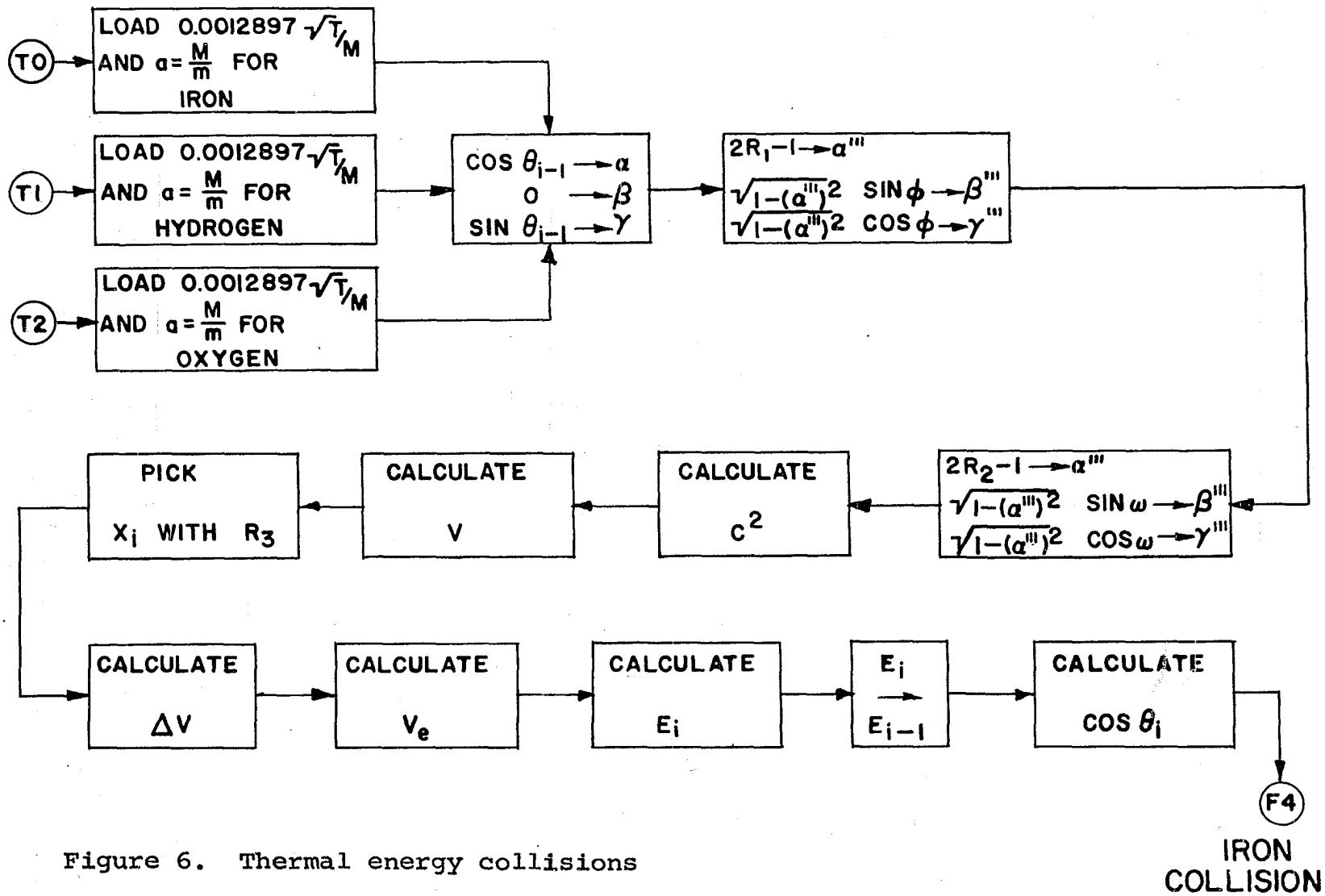

Figure 6. Thermal energy collisions

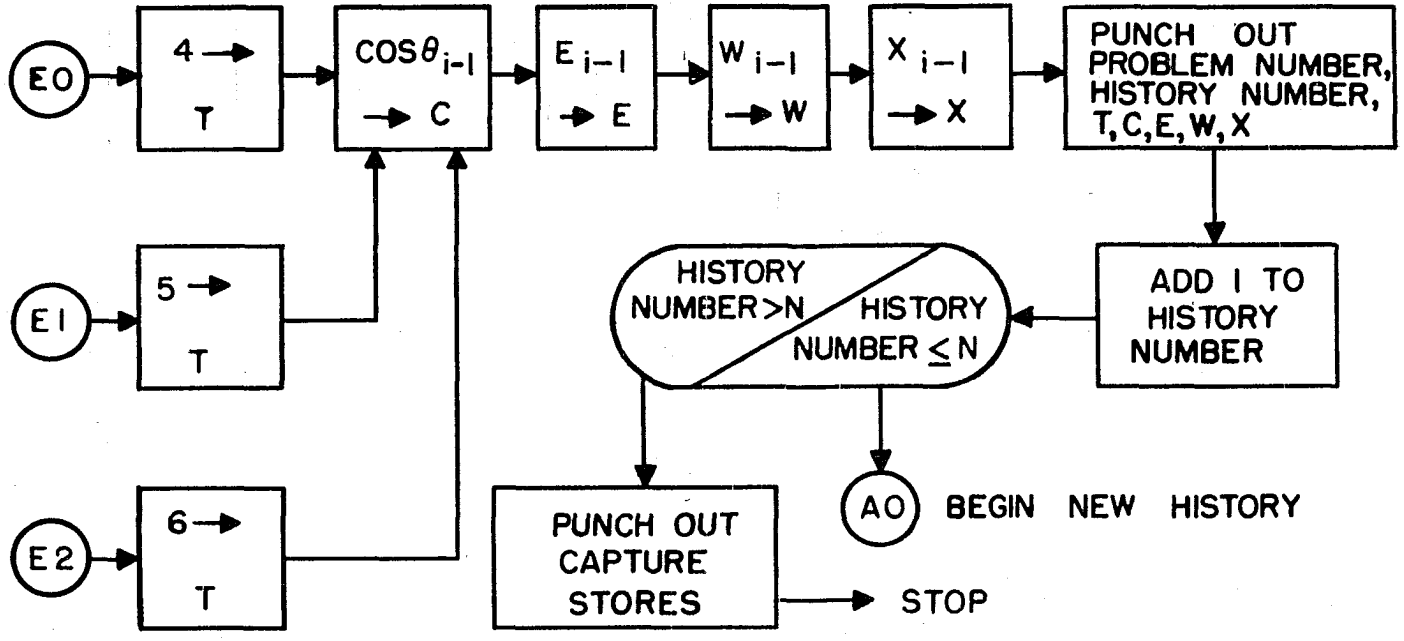

Figure 7. Termination routine

Columns 61-70: W_R = xx.xxxxxxxx

Columns 71-80: sin Θ_o = .xxxxxxxxxx

Card 3.

Columns 1-10: E_o = x.xxxxxxxxx Mev

Columns 11-20: $E_{T_{Fe}}$ = x.xxxxxxxxx Mev

Columns 21-30: E_{T_H} = x.xxxxxxxxx Mev

Columns 31-40: E_{T_O} = x.xxxxxxxxx Mev

Columns 41-45: Problem number

Columns 46-50: Number of the first history (e.g. 00001)

Columns 51-60: $\sqrt{E_o}$ = x.xxxxxxxxx $Mev^{\frac{1}{2}}$

Columns 61-80: Anything (not blank)

The program reads these cards into the machine and stores each parameter into the appropriate locations for use by subsequent parts of the program. Following the entry of the problem parameters, the Δx_i stores in which the capture deposits will be accumulated are cleared to zero and then, the main program is initialized.

(AO) This is the beginning of a new history. The starting parameters, E_o, Θ_o, W_o, and x_o are inserted respectively for E_{i-1}, Θ_{i-1}, W_{i-1}, and x_{i-1}, and the program goes to the geometry routine at (BO).

The description of the remainder of the program, with the exception of the routines for punching out history terminations and the final answers, refers to a general collision, i,

at any stage in the generation of a neutron history.

Figure 3 - Geometry Routine.

(BO) A random input card is read and using the first exponential deviate, Y_i, from this card a random distance, x_i, along the slab normal is calculated from

$$x_i = x_{i-1} + \frac{Y_i \cos \Theta_{i-1}}{2\Sigma_T(E_{i-1})}$$

The correct $\Sigma_T(E_{i-1})$ for the material being traversed is obtained from stored tables.

If $x_i < x_o$, the reflection routine is entered at (EO).

If $x_o < x_i < t_1$, x_{i-1} is replaced by x_i, and the iron collision routine is entered at (FO).

If $x_i > t_i$, the neutron enters the first water layer and x_{i-1} is replaced by t_1. A new x_i is now calculated using the second exponential deviate from the random input card. This x_i is then compared with t_1 and t_2 to determine whether the neutron suffers a collision with water ($t_1 < x_i < t_2$), enters the first iron layer ($x_i < t_1$), or enters the second iron layer ($x_i > t_2$). The history is continued by means of the appropriate routine, depending upon which of these conditions holds, with x_{i-1} replaced by x_i, t_1, or t_2 respectively in the three instances.

This process is continued as described earlier and as shown in Figure 3 until a collision, a reflection, or a transmission takes place. The third random exponential deviate on

each card is used to calculate distances in the second iron layer, the fourth exponential deviate is used for the second water layer, and so on for the six slabs.

Figure 4 - Iron Collision Routine.

(FO) A number Z that is random on (-1, 1) is calculated using R_2, and the nuclear species register is set to 8 designating iron.

If E_{i-1} is larger than the upper energy limit, $E_{T_{Fe}}$, (normally taken as 1 ev) of the thermal energy region for iron, the nonsurvival or capture probability, $\frac{\sigma_a(E_{i-1})}{\sigma_T(E_{i-1})}$, is obtained from stored tables. In the thermal region, $\sigma_a(E_{i-1})$ is assumed to vary as $1/\sqrt{E_{i-1}}$ from a value of 2.5 barns at 0.025 ev (2200 m/sec) (15). The capture probability in this instance is calculated from

$$\frac{\sigma_a(E_{i-1})}{\sigma_T(E_{i-1})} = \frac{K}{\sigma_T(E_{i-1})\sqrt{E_{i-1}}}$$

where K is a constant determined by the 2200 m/sec absorption cross section, and $\sigma_T(E_{i-1})$ is taken from the stored tables.

The capture weight, p_i, to be deposited is calculated and added to the correct Δx_i store as specified by x_{i-1}. W_{i-1} is then replaced by $W_{i-1}-p_i$.

If the new W_{i-1} is larger than W_R the history is continued; otherwise, Russian Roulette is played using R_4. The constant probability Russian Roulette technique shown in Figure 4 is the variation that was used most frequently in the

calculations. Histories that are terminated by the Russian Roulette routine enter the termination routine at (E2).

If Russian Roulette is not played or if the neutron survives the play, the cosine of the scattering angle in the center-of-mass system of coordinates is determined by a routine that depends upon the incident energy of the neutron.

If E_{i-1} is in the thermal energy region for iron, the thermal collision routine is entered at (TO) .

For $E_{T_{Fe}} < E_{i-1} < E_{iso_{Fe}}$, (Appendix L) the scattering will be isotropic in the center-of-mass system and cos ψ_i^* is set equal to Z directly. For $E_{i-1} > E_{iso_{Fe}}$, cos ψ_i^* must be picked from the proper probability distribution (Appendix F).

The number of terms in the differential elastic scattering cross section expansion will vary, depending upon the value of E_{i-1} (Appendix L). For $E_{i-1} < E_{II_{Fe}}$, $p(Z) = \sum_{n=0}^{3} A_n x^n$, while for $E_{i-1} > E_{II_{Fe}}$, $p(Z) = \sum_{n=0}^{8} A_n x^n$.

If $E_{i-1} > E_{II_{Fe}}$, inelastic scattering is possible. The probability of iron inelastic scatter, $\frac{\sigma_{in}(E_{i-1})}{\sigma_T(E_{i-1})}$, is obtained from the stored tables and compared with R_o. If $R_o > \frac{\sigma_{in}}{\sigma_T}$, elastic scatter is specified. If $R_o < \frac{\sigma_{in}}{\sigma_T}$ an inelastic scattering collision is specified. Inelastic scattering is assumed to be isotropic in the center-of-mass system (11) so that cos ψ_i^* is set equal to Z directly for inelastic scat-

tering events.

If anisotropic elastic scattering occurs ($E_{iso_{Fe}} < E_{i-1} < E_{II_{Fe}}$ or $R_o > \frac{\sigma_{in}}{\sigma_T}$), the cosine of the scattering angle is picked from the appropriate distribution, p(Z), by a rejection technique as described in Appendix J and as shown in Figure 4.

After cos ψ_i^* has been selected, the outgoing energy of an elastically scattered neutron is calculated from (Appendix C),

$$E_i = E_{i-1}(0.98241923 + 0.017738077 \cos \psi_i^* + 0.000160135 \cos^2\psi_i^*)^2$$

For an inelastically scattered neutron, the energy change is determined by

$$E_i = E_{i-1} - E_\gamma$$

where E_γ is picked from one of six probability tables as outlined in an earlier section (straightforward model). R_3 is used to pick a value of E_γ from the proper table. The table to be used is determined by E_{i-1} (Appendix K).

The new energy, E_i, then replaces E_{i-1}, after which the angle between the new velocity of the neutron and the slab normal is calculated from (Appendix E),

$$\cos \theta_i = \sin \psi_i \sin \theta_{i-1} \cos \phi_i + \cos \psi_i \cos \theta_{i-1}$$

where cos ϕ_i is a cosine of a random angle, taken from the random input data, and (Appendix D),

$$\cos \psi_i = \frac{1 + a \cos \psi_i^*}{\sqrt{1 + a^2 + 2a \cos \psi_i^*}}$$

$$a = \frac{M}{m} = \text{nuclear mass/neutron mass}$$

Cos θ_{i-1} is then replaced by cos θ_i, a new random data card is read, and the geometry routine is entered again to continue the history. The geometry routine is re-entered at (B0), (B1), (B2), (B3), (B4), or (B5), depending upon x_{i-1}, as shown in Figure 4.

Figure 5 - Water Collision.

(W0) A number, Z, is picked at random from the interval (-1, 1) using R_2, as for an iron collision.

The probability, $\frac{\sigma_O}{\sigma_{H_2O}}$, that the collision is with an oxygen nucleus is found from the stored tables and compared with R_O in order to establish the nuclear species involved in the water collision. If $R_O < \frac{\sigma_O}{\sigma_{H_2O}}$, the collision is considered to be with oxygen; otherwise, the collision is assumed to be with a proton. The nuclear species register is set to 89 for a hydrogen collision and to 899 for an oxygen collision.

For oxygen collisions, only elastic scattering is possible at energies used in this study. Consequently, the iron collision routine is entered immediately at (F2).

When the nucleus involved in the event is a proton, the capture probability is found from stored tables if the incident energy is above the hydrogen thermal region, or, is calculated from $\frac{\sigma_a}{\sigma_H} = \frac{K}{\sigma_H \sqrt{E_{i-1}}}$ if E_{i-1} is less than E_{T_H} (normally

taken as 2 ev). The constant, K, is determined by the 2200 m/sec absorption cross section as described earlier and σ_H is obtained from stored tables. The capture cross section for hydrogen was taken to be 0.33 barns at 2200 m/sec (15). After the capture probability has been determined, the iron collision routine is entered at (F1).

The capture deposit, if one is to be made, is made via the iron collision routine, and on the basis of the contents of the nuclear species register, an exit is made to (W1) for hydrogen or to (W2) for oxygen.

(W1) If $E_{i-1} < E_{T_H}$, the thermal collision routine is entered at (T1) to determine the outgoing energy and the angle with the slab normal made by the outgoing neutron's velocity.

If $E_{i-1} > E_{T_H}$, $\cos \psi_i^*$ is set equal to Z (isotropic scattering angle in the center-of-mass system), and the new energy and scattering angle in the laboratory system of coordinates are determined by

$$E_i = E_{i-1} \frac{1 + a^2 + 2a \cos \psi_i^*}{(1 + a)^2} = \tfrac{1}{2}(1+2R_2-1)E_{i-1} = R_2 E_{i-1}$$

$$\cos \psi_i = \frac{1 + a \cos \psi_i^*}{\sqrt{1 + a^2 + 2a \cos \psi_i^*}} = \sqrt{1 + \cos \psi_i^*} = \sqrt{R_2}$$

where

$$a = \frac{M}{m} \cong 1$$

The iron collision routine is then entered at (F3) in order

to calculate cos θ_i and to continue the history.

(W2) For oxygen collisions that occur with E_{i-1} in the oxygen thermal energy region the thermal collision routine is entered at (T2) in order to establish the new energy and direction of travel.

Oxygen collisions in which $E_{i-1} > E_{T_O}$ (normally taken to be 2 ev) are elastic collisions and cos ψ_i^* must be picked from the proper distribution depending upon E_{i-1}, as was the case for iron collisions.

The distribution of the cosine of the center-of-mass scattering angle is given by, $p(Z) = \sum_{n=0}^{3} A_n x^n$ for $E_{iso_0} < E_{i-1} < E_{II_0}$ and by $p(Z) = \sum_{n=0}^{5} A_n x^n$ for $E_{i-1} > E_{II_0}$ (Appendix L). For $E_{i-1} < E_{iso_0}$, the scattering is isotropic in the center-of-mass system and cos ψ_i^* is set equal to Z.

In oxygen scattering events for which $E_{i-1} > E_{iso_0}$, cos ψ_i^* is picked from the proper distribution by a rejection technique as described in Appendix I and as shown in Figure 5.

The new energy and cos ψ_i are calculated from

$$E_i = E_{i-1} \frac{1 + a^2 + 2a \cos \psi_i^*}{(1 + a)^2}$$

$$\cos \psi_i = \frac{1 + a \cos \psi_i^*}{\sqrt{1 + a^2 + 2a \cos \psi_i^*}}$$

$$a = \frac{M}{m} = \text{nuclear mass/neutron mass}$$

The iron collision routine is then entered at (F3) to calculate cos θ_i and to continue the history.

Figure 6 - Thermal Energy Collisions.

When the velocity of a neutron in a history is reduced to a value that is of the same order of magnitude as the thermal velocity of the atoms of the material through which the neutron is passing, complications enter the treatment of a neutron-nucleus collision that are not present at higher neutron energies.

First, the velocity of the bombarded nucleus due to its thermal motion is no longer small compared to the velocity of the incident neutron, i.e., the nucleus can no longer be assumed to be at rest as was done at higher energies (Appendix B).

In addition, the energies of the chemical bonds between the nucleus and its neighbors becomes significant compared to the neutron's energy. The nucleus is no longer effectively unbound as far as the incident neutron is concerned and inelastic reactions between the neutron and these bonds become relatively important (16).

Due to these factors, the methods and equations that were described earlier cannot be used to establish the changes in energy and direction of travel for a neutron suffering a collision at low (or thermal) energies.

In such collisions, a method presented by J. R. Triplett

et al. (14a) was used. The details of this method are presented in Appendices G and H. Let us now refer again to Figure 6.

(T0) The quantities $0.0012897\sqrt{T/M}$ and a = M/m are calculated for iron where T = the temperature of the medium in °K M = the mass of iron in amu and m = the neutron mass in amu.

(T1) The values of $0.0012897\sqrt{T/M}$ and M/m are calculated for hydrogen.

(T2) The values of $0.0012897\sqrt{T/M}$ and M/m are calculated for oxygen.

The magnitude of the scattered neutron's velocity is then calculated as is the angle that this velocity makes with the slab normal. The equations used for these calculations were presented earlier in the section on the straightforward model, and, as mentioned, are described in detail in the Appendices. The steps involved are outlined in Figure 6.

After the new energy and angle with the slab normal have been established, the iron collision routine is entered at (F4) to continue the history.

Figure 7 - Termination Routine.

The termination routine is entered at (E0) where a 4 identifies a reflection, at (E1) where a 5 identifies a transmission, or at (E2) where a 6 is used to identify a Russian Roulette termination.

Following the adjustment of the store identifying the

type of termination, the values of E_{i-1}, W_{i-1}, x_{i-1}, and the contents of the termination identification store are punched out on a standard IBM card. The history termination card contains the following:

Columns 1-5: Problem Number

Columns 6-10: History Number

Columns 11-20: Type of Termination

Columns 21-30: Cos θ_{i-1} = xx.xxxxxxxx

Columns 31-40: E_{i-1} = x.xxxxxxxxx Mev

Columns 41-50: W_{i-1} = xx.xxxxxxxx

Columns 51-60: x_{i-1} = xxx.xxxxxxx cm

Columns 61-80: Meaningless

After this punch-out, the history number is increased by 1 and is compared with N, where N is the total number of histories to be calculated. If the history number is less than or equal to N, a new history is begun at (AC) in Figure 2. If the total number of histories that have been calculated is equal to N, the contents of the capture stores (Δx_i stores) are punched out and the problem stops.

The capture store punch-out is in the following form:

Columns 1-5: Problem Number

Columns 6-10: N + 1

Columns 11-80: 7 ten-digit words in the following form, rrrsssssss, where rrr = serial number of the store (001 to n) and sssssss = the contents of the store in the decimal form xx.xxxxx

OPTIONAL ROUTINES

Isotropic Monoenergetic Source

An isotropic monoenergetic source was supplied by setting $\cos \theta_o = 2R_2 - 1$. The flow sheet for this optional routine is shown in Figure 8.

Monoenergetic Cosine Source

The intensity of the radiation at the surface of a large volume source of nuclear radiation is often approximately proportional to the cosine of the angle at which the radiation emerges from the surface (17). This is rigorously true if the strength of the source is uniform throughout the volume of the source and if the attenuation of the radiation in the material of the source is exponential in character.

Such a cosine surface source was used in most of the calculations for this study.

The probability distribution function of the emergent angle for a cosine source is given by

$$p(\theta)d\Omega = -\frac{1}{\pi}\cos\theta\, d\Omega = -2\sin\theta\cos\theta\, d\theta$$
$$= 2\cos\theta\, d\cos\theta = q(\cos\theta)d\cos\theta$$
$$(0 \leq \cos\theta \leq 1)$$

where $p(\theta)$ is the probability per unit solid angle of emission at an angle θ, $d\Omega$ is an increment of solid angle, and $q(\cos\theta)$ is the corresponding probability distribution for the cosine of the emergent angle.

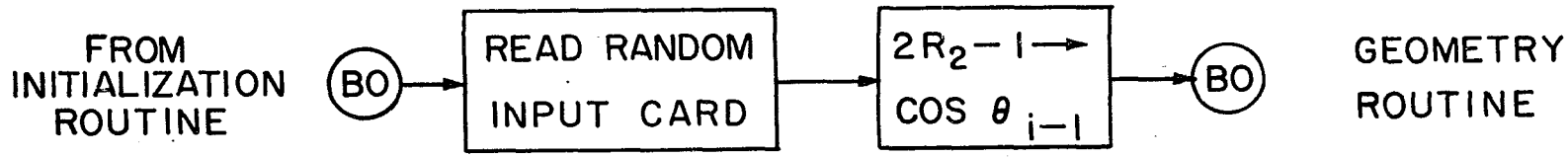

Figure 8. Isotropic monoenergetic source

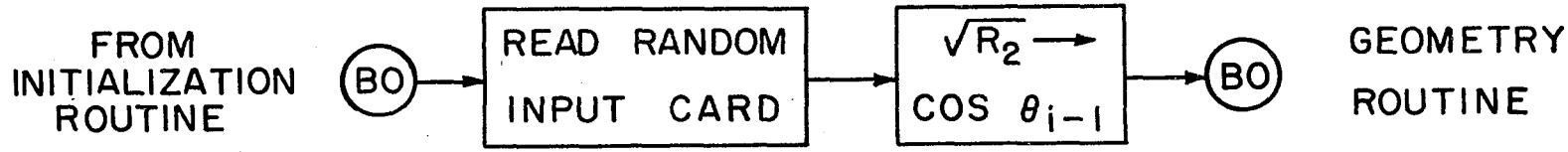

Figure 9. Monoenergetic cosine source

To pick a random sample from this distribution, we transform to the uniform distribution, g(y), as described earlier.

$$g(y) = 1 \text{ for } 0 \leq y \leq 1$$
$$= 0 \text{ elsewhere}$$

Application of the "Golden Rule" gives

$$Q(\cos\theta) = P(\cos\theta' \leq \cos\theta) = \int_0^{\cos\theta} q(\cos\theta')\,d\cos\theta' =$$

$$\cos^2\theta = P(y' \leq Y) = \int_0^Y g(y')\,dy' = \int_0^Y dy' = y =$$

$$G(y) = R$$

where R is a number selected at random from the interval (0, 1). R constitutes a random sample from G(y) and from Q(cos θ). Thus, we set

$$\cos^2\theta = R$$

or

$$\cos\theta = \sqrt{R}$$

The routine in Figure 9 was used to generate a monoenergetic cosine source.

Isotropic Thermal Source

An isotropic thermal neutron source was generated by selecting E_o from the Maxwell-Boltzmann distribution of neutron energies (18) and by setting $\cos\theta_o$ equal to $2R_2 - 1$.

The Maxwell-Boltzmann energy distribution is given by

$$n(E)\,dE = \frac{2\pi n}{(\pi k_B T)^{3/2}}\, e^{-E/k_B T} E^{\frac{1}{2}}\, dE$$

where n = total number of neutrons/cm^3 and n(E)dE = neutrons/cm^3 with energy in dE at E.

The energy range from 0 to 10 electron volts was divided into 48 intervals as shown in Table 1 and the cumulative Maxwell-Boltzmann distribution, C_i, was calculated for each energy at 298°K.

$$C_i = \int_0^{E_i} n(E)\,dE$$

(Note that $P(E_{i-1}) \leq E \leq E_i) = C_i - C_{i-1} = \int_0^{E_i} n(E)\,dE - \int_0^{E_{i-1}} n(E)\,dE$).

These cumulative probabilities are also given in Table 1.

To specify E_o, a random number, R_1, from a random input card was compared with the cumulative distributions given in Table 1. The energy corresponding to the first C_i larger than or equal to R_1 was taken to be E_o. (This is the same method used to select interaction types as described in the section on the straightforward model.)

The flow sheet for the isotropic thermal neutron source routine is shown in Figure 10.

Uniform First Collision Weighting

The number of neutrons that penetrate to a given distance, x, into the array of Figure 1 from the source, becomes small as x becomes large. The number of capture deposits at such distances is therefore small and the variance, or statistical uncertainty, of the results is large. There is, therefore, a

Table 1. Cumulative Maxwell-Boltzmann energy distribution

E_i(ev)	C_i	E_i(ev)	C_i
0.001	0.00500	0.105	0.95527
0.002	0.01496	0.110	0.96212
0.003	0.02746	0.115	0.96832
0.004	0.04159	0.120	0.97320
0.005	0.05707	0.125	0.9725
0.010	0.14505	0.130	0.98055
0.015	0.23886	0.135	0.98530
0.020	0.33029	0.140	0.98567
0.025	0.41573	0.145	0.98766
0.030	0.49353	0.150	0.98942
0.035	0.56315	0.155	0.99080
0.040	0.62497	0.160	0.99202
0.045	0.67911	0.165	0.99294
0.050	0.72609	0.170	0.99377
0.055	0.76669	0.175	0.99444
0.060	0.80165	0.180	0.99502
0.065	0.83177	0.185	0.99562
0.070	0.85755	0.190	0.99563
0.075	0.87937	0.200	0.99565
0.080	0.89787	0.250	0.99575
0.085	0.91358	0.350	0.99725
0.090	0.92689	0.500	0.99875
0.095	0.93807	1.000	0.99900
0.100	0.94722	10.000	0.99999

limit to the thicknesses that may be examined meaningfully.

One means of extending this limit is to take advantage of the fact that the distribution of first collisions is known exactly. This makes it possible to devote a larger fraction of the computing time to deeply penetrating histories and to correct the final answers accordingly. This is done at the

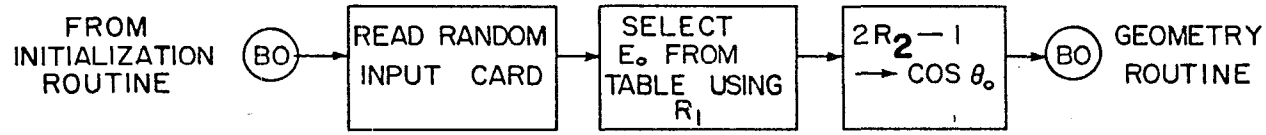

Figure 10. Isotropic thermal source

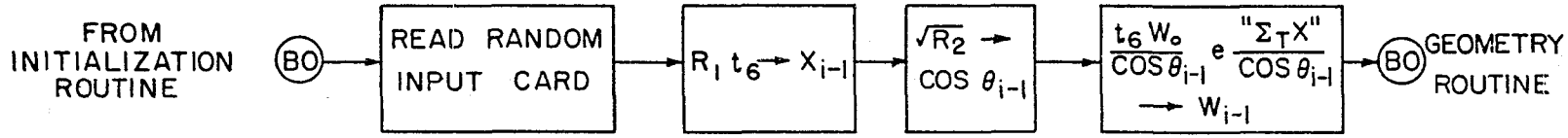

Figure 11. Uniform first collision weighting

expense of increasing the variance of the shallow penetration results, but the net effect is a significant increase in the limit of dimensions that may be studied.

The method proceeds as follows. Instead of allowing the first collisions to be picked according to the exponential attenuation law (Appendix A), the first collisions are picked uniformly throughout the array. The weight of each neutron is then adjusted so that the average weight of neutrons having first collisions at any distance into the assembly is unchanged. In other words, instead of following $Ne^{-"\Sigma_T x"}\,dx$ neutrons of weight W_o that suffer first collisions in dx at x (total weight of $W_o Ne^{-"\Sigma_T x"}\,dx$), we follow Ndx/t_6 neutrons with first collisions in dx at x and let each of these have starting weight $W_o e^{-"\Sigma_T x"} t_6$. Here, "$\Sigma_T x$" is the number of relaxation lengths from the starting point to x. With this method, the number of events is approximately constant throughout the array, but the weight of the capture deposits is adjusted so that the net results are, on the average, unchanged.

The flow sheet for this routine is shown in Figure 11 for a cosine source.

TEST RUNS

If we ignore errors in the basic cross section data, the only approximations in the equations and techniques presented in the previous sections occur in the low energy or "thermal" treatment as described in Appendices G and H.

As pointed out in Appendix H, the most important low energy events are neutron-proton collisions. The relatively low frequency of thermal neutron-oxygen collisions and the usually small energy changes accompanying thermal neutron-iron collisions cause the approximations made in the treatment of these events to be of relatively minor importance. Energy changes accompanying neutron-proton collisions are, on the other hand, quite important. Since the capture cross sections are inversely proportional to the square root of the neutron energy, the capture distributions are sensitive to the thermal neutron energy spectrum and, hence, to approximations made in the treatment of thermal neutron-proton collisions.

For this reason it was considered essential, before proceeding to the main calculations, to make a check of the thermal neutron energy spectrum and capture distribution produced by the program for water.

In an early version of the final program a cut-off weight, W_c, was used to terminate neutron histories. This version of the program also punched out the values of the state variables (E_{i-1}, x_{i-1}, $\cos \theta_{i-1}$, W_{i-1}) for each collision. This program

made it possible to generate by fixing W_c at zero, an interminable neutron history, with the state variables for each collision being punched out on cards.

Such a history in water (with the thicknesses of the iron slabs set to zero) reaches thermal equilibrium after 10 to 40 collisions. By counting the number of collisions (after equilibrium is reached) that occur in each of several specified energy intervals, an energy spectrum for the collisions can be obtained. This energy distribution for thermal neutron collisions constitutes a sample of the equilibrium thermal neutron energy spectrum produced by the program for water. If the number of events is large, the sample should give a good measure of this spectrum.

It should be noted that all of the collisions in the above frequency count are given equal weight. This is tantamount to assuming that the capture cross section of water is zero, since there is no weight reduction from collision to collision; i.e., there is no capture. The thermal neutron capture cross section of water is small however, and the energy spectrum in actual water does not differ greatly from the Maxwellian spectrum that would exist in water with zero capture cross section (19), (20). The Maxwellian energy distribution is given by

$$n(E)\,dE = \frac{2\pi n}{(\pi k_B T)^{3/2}}\, e^{-E/k_B T}\, E^{1/2} dE$$

This distribution was described earlier in the section on optional routines.

A series of spectrum runs, as just described, was calculated using different schemes of effective proton mass vs neutron energy in each run. These runs consisted of 3000 to 5000 collisions each. Comparison of the resulting spectra with the Maxwellian distribution was used as a basis for choosing the effective proton mass scheme to be used in the program. The mass schemes tested are given in Table 2. These

Table 2. Effective proton masses (in amu) vs incident neutron energy

E(ev)	I Reference (20)	II Empirical scheme	III Triplett et al. (22)	IV (Described in text)
10.0	1.9	1.0	1.0	1.0
1.0	"	1.9	1.0	1.4
0.1	"	1.9	1.25	2.0
0.074	"	1.9	1.55	2.8
0.049	"	5.0	1.98	3.6
0.035	"	5.0	2.40	4.6
0.028	"	5.0	2.65	5.0
0.025	"	5.0	2.90	5.6
0.021	"	10.0	3.10	6.0
0.019	"	10.0	3.40	6.6
0.017	"	10.0	3.54	7.6
0.014	"	10.0	3.92	9.0
0.012	"	18.0	4.42	10.0
0.009	"	18.0	5.0	13.0
0.007	"	18.0	6.3	17.0
0.005	"	18.0	7.7	23.0
0.003	"	18.0	10.0	32.9
0.001	"	18.0	15.05	65.0

masses were obtained from the following sources:

I. Brown, H. Dean. Neutron energy spectra in water (20).

II. An empirical scheme of masses devised to increase with decreasing neutron energy from 1.9 amu at 1 ev (20) to 18 amu at 0.001 ev (21).

III. Triplett, J. R., et al. (22). These masses were based upon reference (23). A graph of these effective proton masses vs neutron energy is given in Appendix H.

IV. These empirical masses are roughly 2A - 1, where the A are the effective masses from reference (23), modified somewhat at lower neutron energies.

The spectra from these runs are compared with the Maxwellian spectrum in Figures 12 and 13. In Figures 12 to 14 p(E) is the probability per unit energy that a neutron will have energy in dE at E, i.e., $p(E) = n(E)/n$. As can be seen from the figures, only the empirical proton masses of scheme number IV lead to a Maxwellian neutron spectrum for water.

In order to check the masses of IV at temperatures other than 298°K, a spectrum run was made with the masses of IV and a temperature of 375.5°K. The thermal neutron spectrum from this run is compared with the Maxwellian spectrum in Figure 14. The agreement with the Maxwellian curve in Figure 14 is

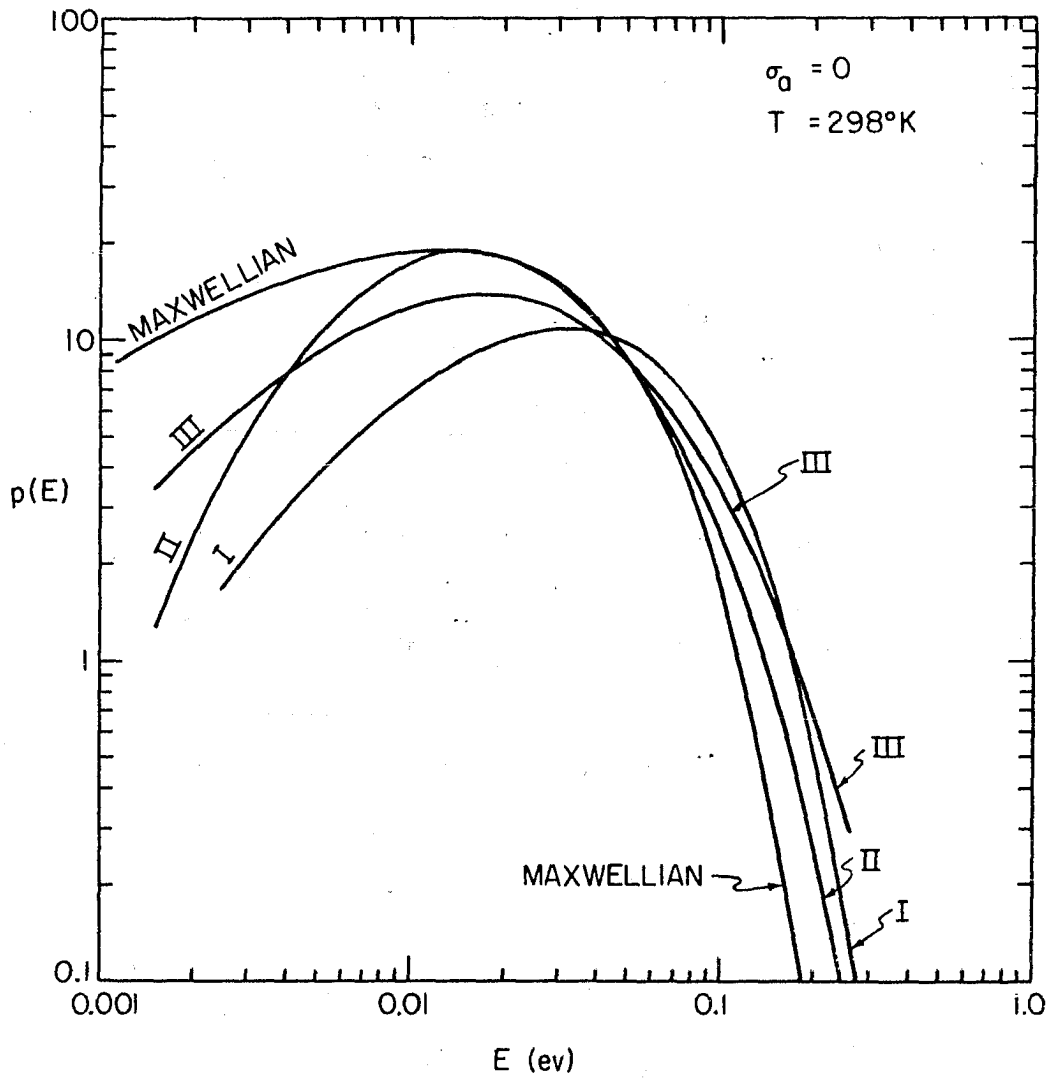

Figure 12. Monte Carlo produced thermal neutron spectra in water for various effective proton mass schemes

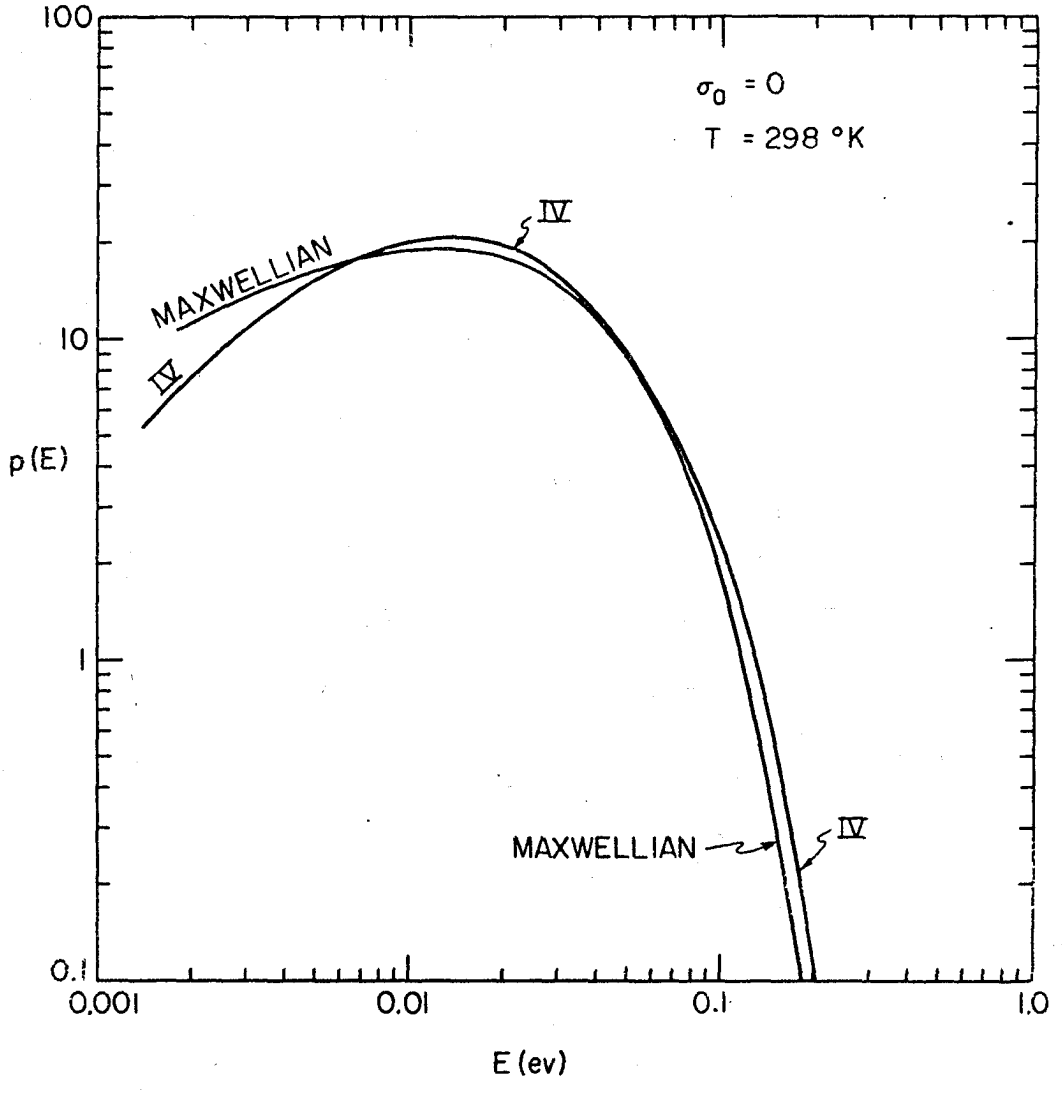

Figure 13. Monte Carlo produced thermal neutron spectrum in water for effective proton mass scheme #IV at 298°K

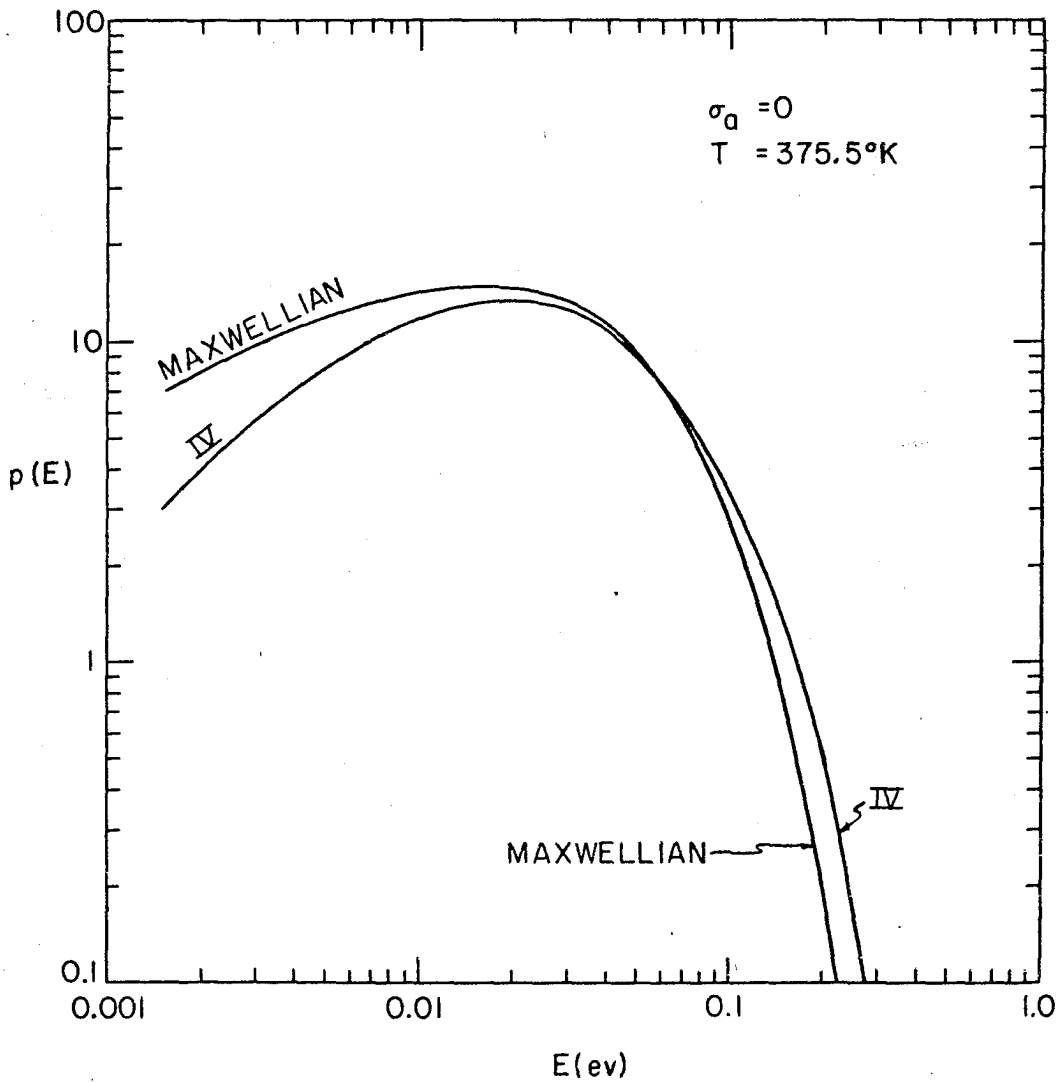

Figure 14. Monte Carlo produced thermal neutron spectrum in water for effective proton mass scheme #IV at 375.5°K

poorer than that in Figure 13. However, the two curves in Figure 14 have the same shape, and the slight shift of the Monte Carlo curve could be corrected by a few relatively small empirical changes in the effective mass scheme.

Since temperature effects were not included in this study, it was decided to use effective mass scheme number IV and to make the remainder of the calculations at a temperature of 298°K.

A final test of the low energy routine and of the effective proton mass scheme IV was made by generating an isotropic thermal neutron source, as described earlier, at one surface of a large water layer (iron thicknesses set to zero). A total of 200 histories was generated in about 10 hours. Points on the capture distribution curve were then calculated from

$\bar{p}(x)$ = the probability of capture per unit distance per incident neutron = $P(x)/\Delta x N$

where

$P(x)$ = the weight deposited in Δx at x by the calculation

x = the mid-point of Δx

N = the total number of histories in the calculation

The capture distribution for this problem should be given adequately by simple diffusion theory (9) (see the earlier section on neutron transport). Diffusion theory gives

$$p(x) = \Sigma_a \phi(x) = \Sigma_a \frac{e^{-Kx}}{2KD} = 0.1969\ e^{-0.3937\ x}$$

where

$\phi(x)$ = the thermal neutron scalar flux per unit source

Σ_a = the macroscopic cross section for capture of thermal neutrons in water = 0.02201 cm^{-1} (8)

D = the thermal neutron diffusion coefficient for water = 0.142 cm (8)

$K^2 = \Sigma_a D$

The Monte Carlo data points were fitted by the function $p(x) = A\ e^{B\ x}$, as described in Appendix N, with the following result,

$$p(x) = 0.1762\ e^{-0.3920\ x}$$

This curve and the Monte Carlo data are compared with the diffusion theory capture distribution in Figure 15. The Monte Carlo curve agrees with the theoretical curve even more closely than might be expected from the small number of histories that was generated.

An albedo, or fraction of incident neutrons that were reflected, was calculated from the Monte Carlo results. The Monte Carlo albedo was 0.823, compared with the experimental thermal neutron albedo for water (9) of 0.821.

An attempt was made to find some theoretical or experimental results that might be used to check the high energy portion of the Monte Carlo program. This search was not

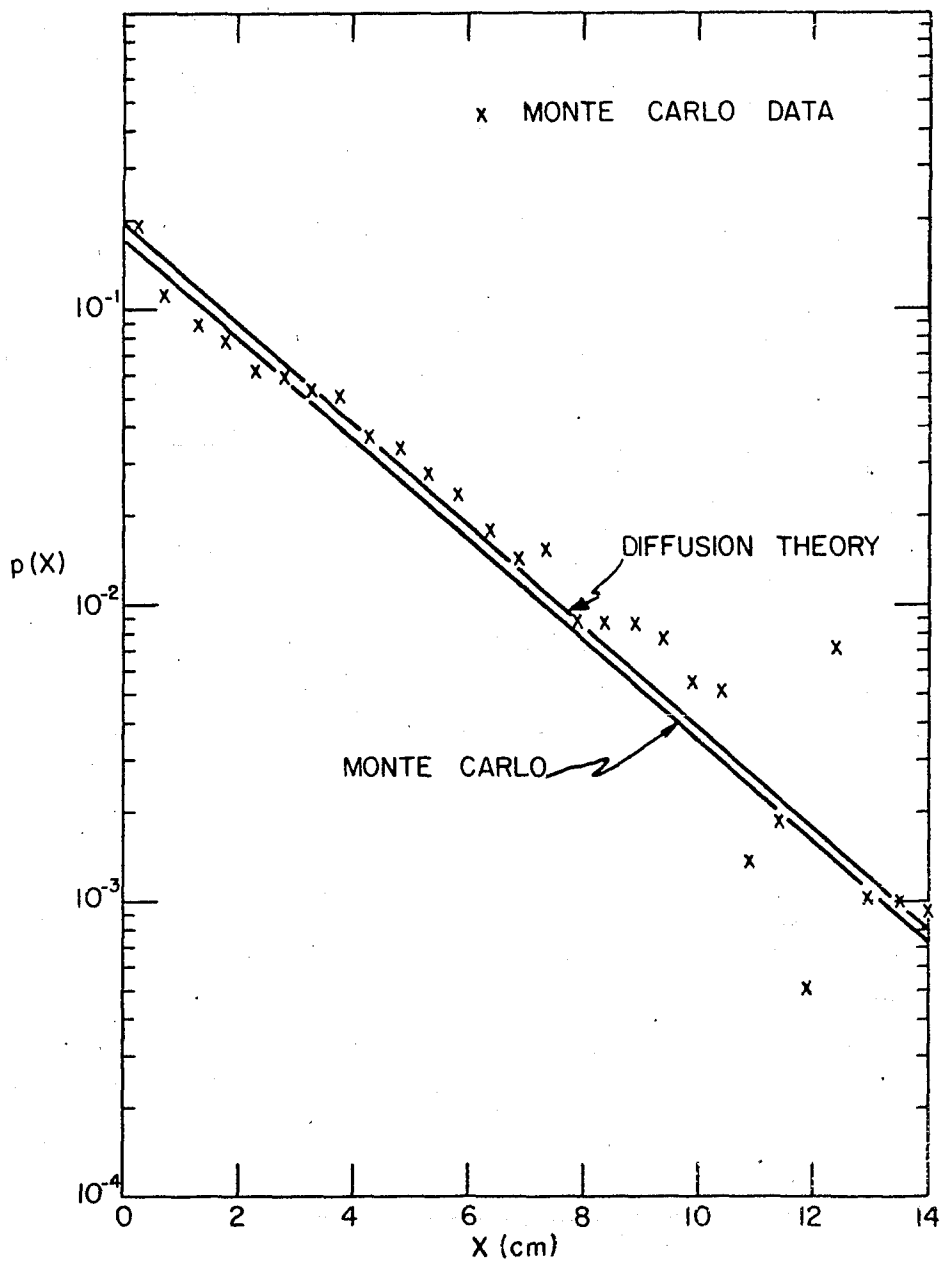

Figure 15. Capture distribution from a plane isotropic thermal neutron source at one surface of a large water slab (x = distance from the plane source)

successful. As pointed out earlier, such a problem is not amenable to solution with the usual mathematical methods. It appears also that no directly comparable experimental results are available. Therefore, the high energy portion of the program was not checked with a test problem. It would be expected, however, that results produced by this portion of the program would be as reliable as the cross section data that were used in the program.

PRELIMINARY RUNS

Several preliminary problems were run in order to establish the problem parameters (slab geometry, angle of incidence, incident energy) that were most important. These runs also served to define the ranges of problem parameters that were practical for study with the program.

The principle limitations of the program were in the slab thicknesses and the source energies that could be used. The upper limit for the source energy was 4.65 Mev. This limit was imposed by the lack of storage space for the cross section data necessary for additional energy groups (Appendix L). Because of the relatively short mean free path of thermal neutrons in water and the low neutron capture cross section in water, the running time per problem was very sensitive to the thicknesses of the water layers. One attempt was made to run a problem in which the water layers were two inches thick. This problem was abandoned after 2.5 hours with only 60 histories completed. All subsequent problems used water thicknesses of one inch or less. This (1") appeared to be an approximate upper limit for the thickness of water that could be studied. Some typical running times will be given later and it will be seen that the dimensions of the iron layers are much less important in determining the computing time required for a given problem.

The Monte Carlo capture curves that will be presented in

the remainder of this paper were obtained from the following curve fits (Appendix N):

Water layers: $p(x) = A + Bx + Cx^2$

First iron layer: $p(x) = \alpha e^{\beta x}$

Other iron layers: $p(x) = \alpha \cosh \beta(x-x_o)$

In fitting all of the curves, the origin of the x axis was taken as the left face of the particular slab being considered. This was done for convenience in both the curve fitting calculations and in the subsequent presentation of the correlations for the curve parameters. Transformation to another coordinate system, $[p(x'), x']$, is accomplished easily by substituting $x = x' - x_d$ into the original equation, where x_d is the displacement of the left face of the slab in the new coordinate system.

As pointed out earlier, $p(x)$ is the probability of capture per unit distance per incident neutron, and the data points for the curve fits were obtained from

$$\bar{p}(x) = P(x)/\Delta x N$$

where $\bar{p}(x)$ are the "observed" points to be fitted, $P(x)$ is the weight deposited in Δx at x by the calculations, x is the midpoint of Δx and N is the total number of histories in the run.

The first problem that was calculated was:

$t_1 = 1"$	$t_2 = 2"$	$t_3 = 3"$
$t_4 = 4"$	$t_5 = 7"$	$t_6 = 10"$
$E_o = 1$ Mev	$\theta_o = 0°$	$x_o = 0$

$\Delta x = 0.1"$ $T = 298°K$

The resulting fitted capture curves are presented in Figure 16. This problem consisted of 400 histories and required 11 hours of computing time.

An attempt was made to estimate the variance of the curves in Figure 16 by dividing the data into four groups of 100 histories each and fitting curves to each of these groups of histories. The resulting four curves in each layer constituted four independent estimates of the final curve so that a variance for each curve could be calculated in the usual manner,

$$s^2(x) = \sum_{i=1}^{4} [p_i(x) - p(x)]^2/3 = \text{the variance of the curve at x}$$

The $p_i(x)$ are the four independent estimates of the capture probability at x, and p(x) is obtained from the fitted 400-history curve. The resulting coefficients of variation, where the coefficient of variation is defined as the standard deviation at x divided by p(x), were between 10% and 35%.

This method of estimating the statistical uncertainty of the results was not satisfactory. The small number of degrees of freedom, i.e., the small number of independent estimates of each curve meant that the variance estimates were inaccurate. In addition the curve fitting was very time-consuming. The computing time required with this procedure is not justified

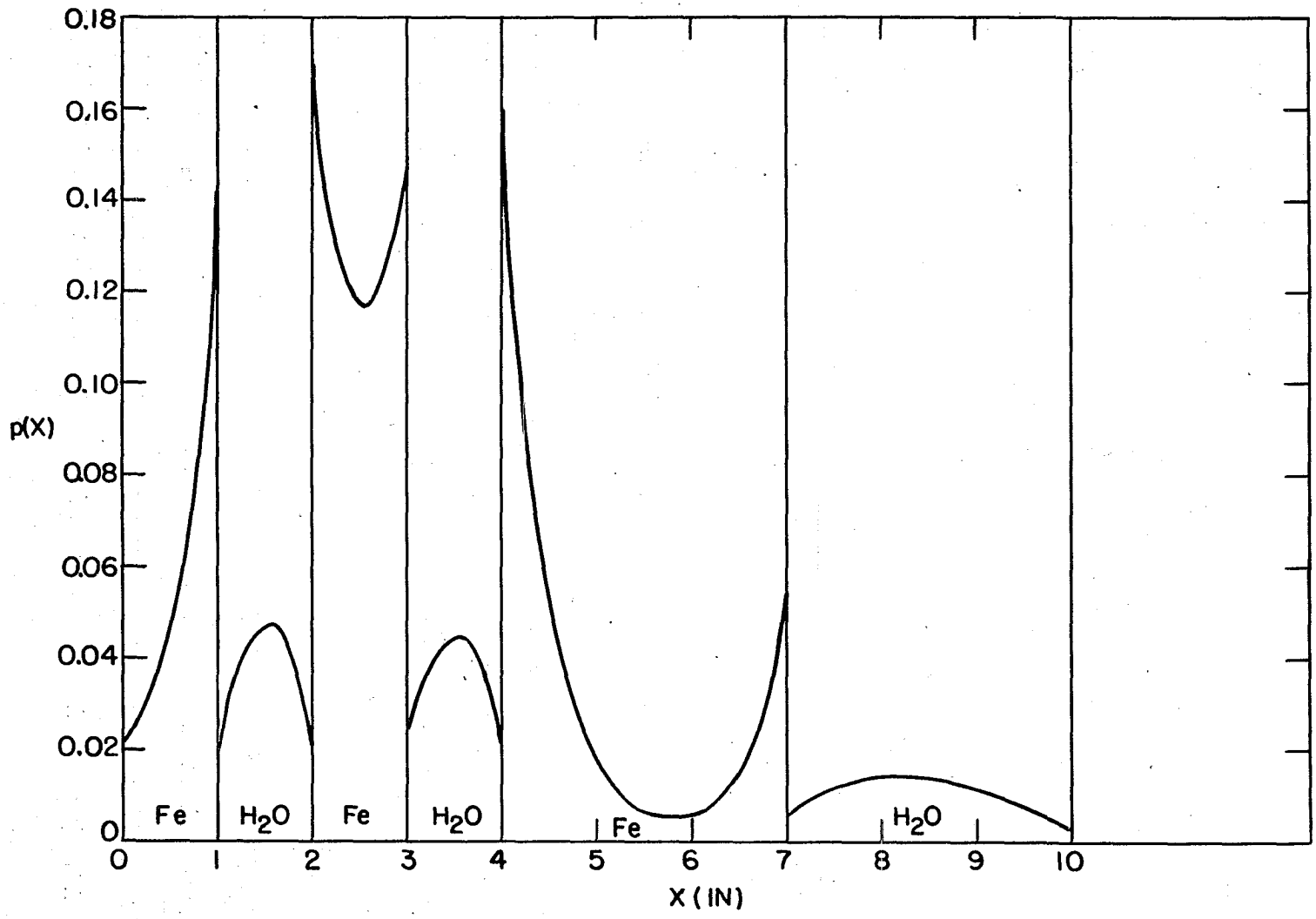

Figure 16. Capture distribution from a 1 Mev normally incident source at x = 0

by the quality of the results. It was decided to calculate the statistical uncertainties only for the data points, $\bar{p}(x)$, in subsequent runs. The variances of the fitted curves are smaller than the variances of the $\bar{p}(x)$, but the magnitude of this improvement is very difficult to determine. This point will be discussed further in a later section.

The most uncertain points in the curves of Figure 16 are the surface points in the second iron layer. This also appeared to be characteristic of subsequent runs. The values of surface points in thin iron slabs in the interior of such an array are very sensitive to statistical fluctuations in the number of thermal neutrons diffusing into the iron from the adjacent water layers. Some improvement in the determination of these points can be accomplished through the use of the statistically more accurate water capture data at the slab boundaries, as will be pointed out later. However, at present suffice it to say that the estimated capture rates at the interior iron surfaces in Figures 16 to 21 may be in error by 20 to 40%. Comparisons at these points of the results of other runs with the results in Figure 16 should be made with this fact in mind.

The data in the interior of a thicker iron slab such as the third iron layer in Figure 16 influence the end points of the capture curve to a greater extent than do the data in the interior of thinner layers. Thus, the end points of the curve

in the third iron layer in Figure 16 are more accurately defined than those for the curve in the second iron layer.

The second problem that was run was identical to the problem just described with the exception that the water was poisoned with 2.0 w/o boric acid. Running time for 400 histories in this problem was 7 hours. The resulting capture distributions are compared with the results of the unpoisoned run in Figure 17. Capture rates were reduced in the iron layers and increased in the water layers as expected. The usefulness of data on poisoned water systems did not appear to be such that further poisoned water runs were merited in this study; therefore, this was the only such problem that was run. The primary reason for including a description of this run is to point out the reduced running time required for poisoned problems. The water thickness limitation is relaxed somewhat for such problems.

Neutron scattering in the laboratory system of coordinates is anisotropic for iron and oxygen at higher energies and for hydrogen at all energies. It would be expected, therefore, that the capture distribution through an array of iron and water slabs from neutrons impinging upon one surface of the array would be dependent upon the angle of incidence of the source neutrons, i.e., upon the angular spectrum of the source.

A series of runs was calculated with which to examine

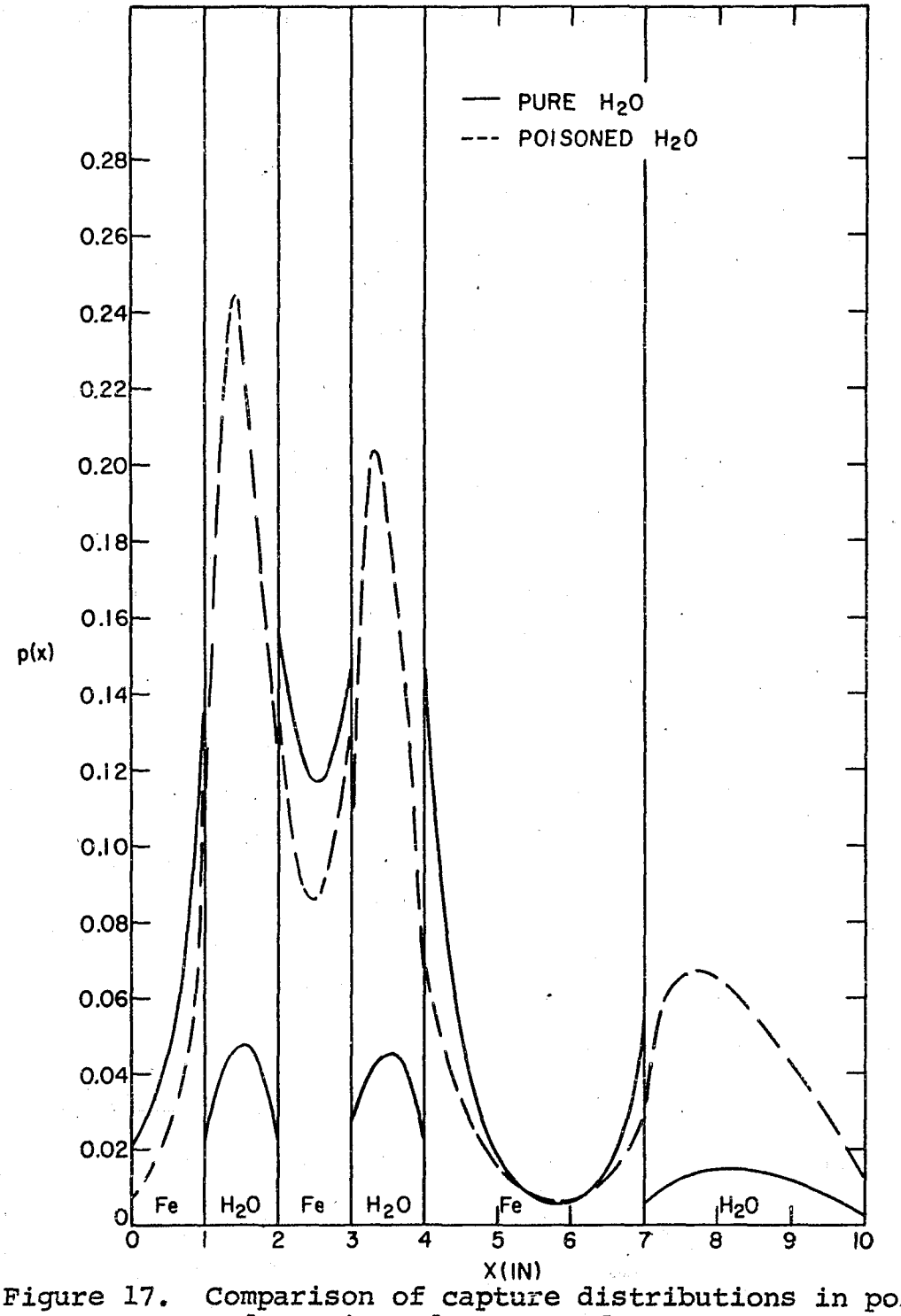

Figure 17. Comparison of capture distributions in poisoned and unpoisoned systems from a 1 Mev normally incident source at x = 0

this dependence. The following basic problem was run with three different source angular spectra.

$t_1 = \frac{1}{2}$" $t_2 = 1$" $t_3 = 1\frac{1}{2}$"

$t_4 = t_5 = t_6 = 2$" $E_o = 1$ Mev $x_o = 0$

$\Delta x = 0.1$" $T = 298°K$

The three source angular spectra were: a normally incident source ($\theta_o = 0$), an isotropic source, and a cosine source. Running times for these problems were 6 to 9 hours for 2000 to 3000 histories. The resulting capture curves are compared in Figure 18. A small decrease is evident in the distribution resulting from the normally incident source as compared with the distributions from the other two sources. The curves are the same for the isotropic and the cosine sources within statistical uncertainties. Coefficients of variation of the data points in these runs are given in Table 3.

A final run in this series was made using the parameters of the first problem that was described in this section (Figure 16) and a cosine source. This calculation also employed the uniform first-weighting technique described in the section on optional routines. Running time in this problem was 12.7 hours for 400 histories. The resulting capture curves are compared with the results for the normally incident source (Figure 16) in Figure 19. The cosine source resulted in larger capture rates in the first three layers than the normally incident source. This increase, although larger than

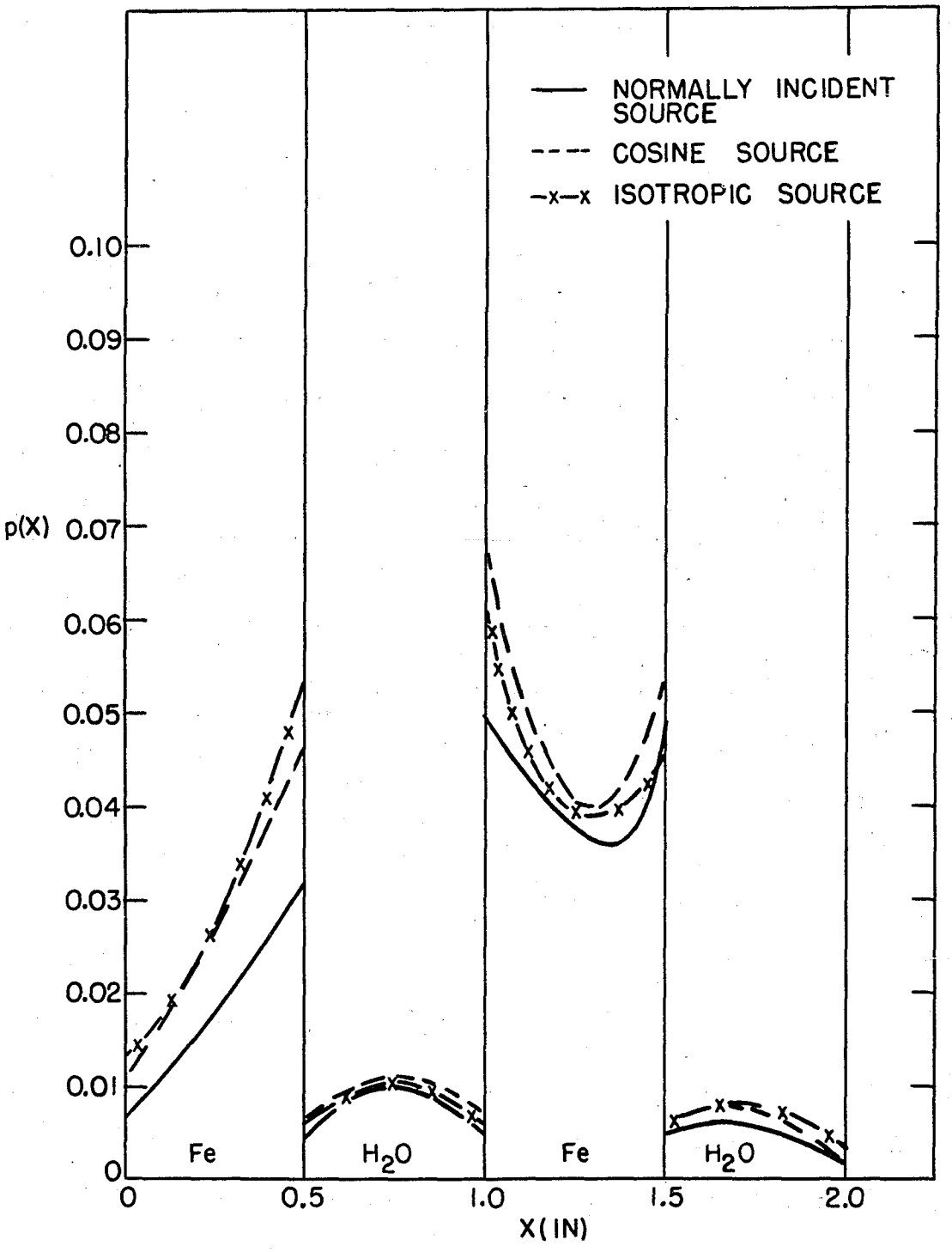

Figure 18. Effect of source angular spectrum upon the capture distribution--1 Mev source at x = 0

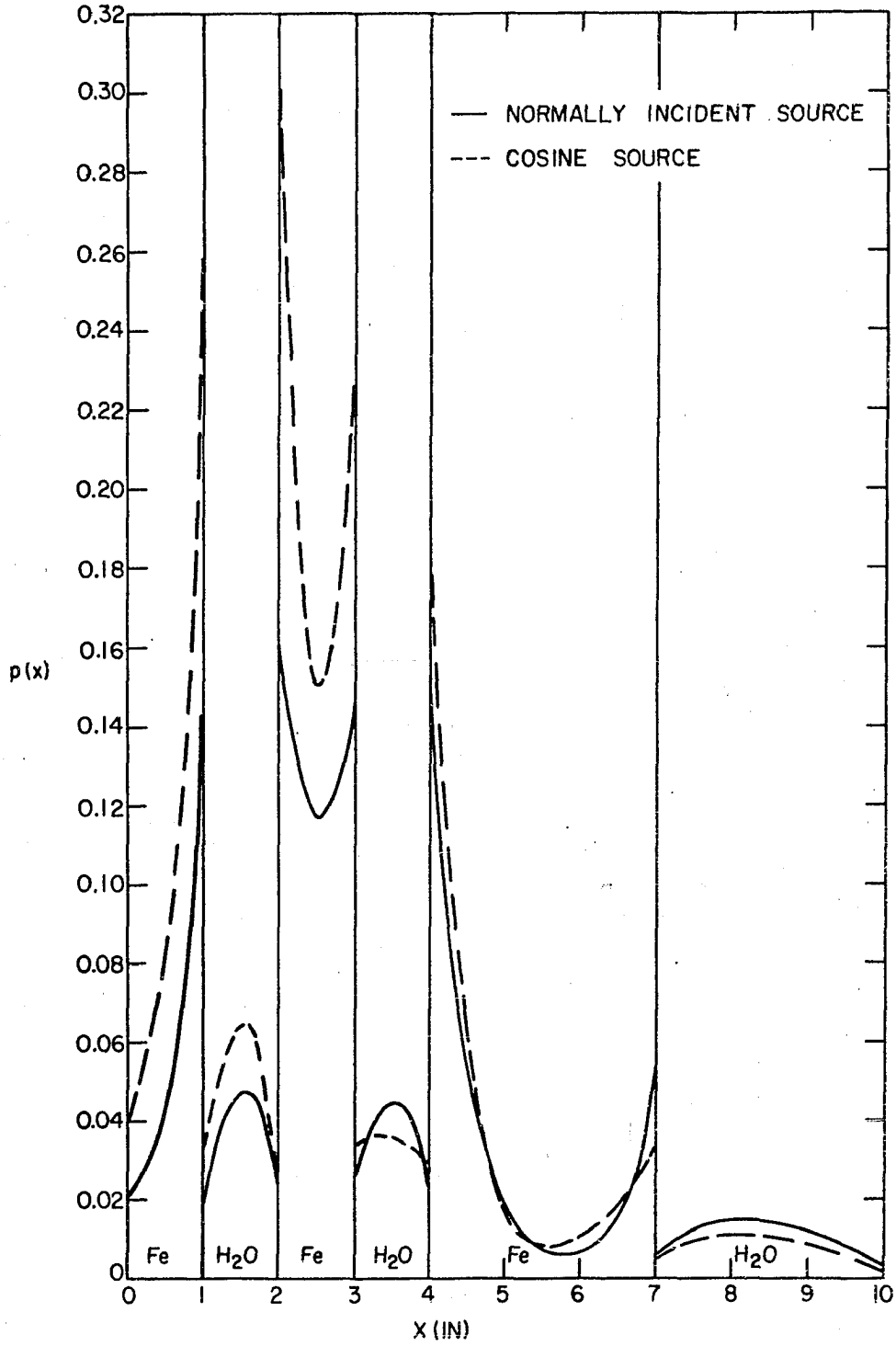

Figure 19. Effect of source angular spectrum upon the capture distribution, 1 Mev source at x = 0

Table 3. Coefficients of variation of data points from the source angular spectrum runs in the ½" geometry x = 0 at the left face of the array

	x(in.)	normally incident source	cosine source	isotropic source
	0.05	0.243	0.120	0.251
	0.15	0.252	0.228	0.151
Fe	0.25	0.227	0.180	0.182
	0.35	0.222	0.184	0.145
	0.45	0.216	0.228	0.120
	0.55	0.181	0.118	0.102
	0.65	0.185	0.099	0.072
H_2O	0.75	0.179	0.083	0.102
	0.85	0.177	0.116	0.105
	0.95	0.164	0.071	0.092
	1.05	0.172	0.051	0.109
	1.15	0.168	0.182	0.121
Fe	1.25	0.192	0.066	0.141
	1.35	0.153	0.136	0.126
	1.45	0.187	0.128	0.266
	1.55	0.195	0.141	0.119
	1.65	0.178	0.177	0.086
H_2O	1.75		0.259	0.123
	1.85		0.319	0.141
	1.95		0.304	0.128

the increase in the smaller geometry, was considerably smaller than the changes in the capture rates that resulted from changing the geometry. This latter effect can be seen by comparing Figures 18 and 19.

It should be pointed out that the fractions of neutrons that are reflected and transmitted are more sensitive to changes in the source angular spectrum than are the capture distributions. The normally incident, cosine, and isotropic

sources in the problems of Figure 18 resulted in reflection fractions of 0.209, 0.353, and 0.442 respectively, while the transmission fractions for these three problems were 0.743, 0.602, and 0.514 respectively.

Most sources encountered in actual reactor applications will approximate cosine or isotropic sources much more closely than normally incident sources. Therefore, on the basis of the results just described, it was decided to use cosine sources in the remainder of the calculations. The results should apply quite well to problems with isotropic sources and reasonably well to thin slabs with normally incident sources.

The final series of preliminary runs was designed to examine the effect of reducing the number of layers in the array. A repeat of the first problem (Figure 16) was run in which the thicknesses of the third water layer and the third iron layer were set to zero. The capture distributions in the remaining layers are compared in Figure 20 with the results in the corresponding layers for the first problem. Figure 21 shows a similar comparison between the results from a 1 Mev cosine source using six ½" layers and results from the same problem with the thicknesses of the last iron and the last water layers set to zero (this latter problem is the same problem for which results were presented in Figure 18).

The small effect upon the capture rates of removing the last two layers of the larger geometry as contrasted with the

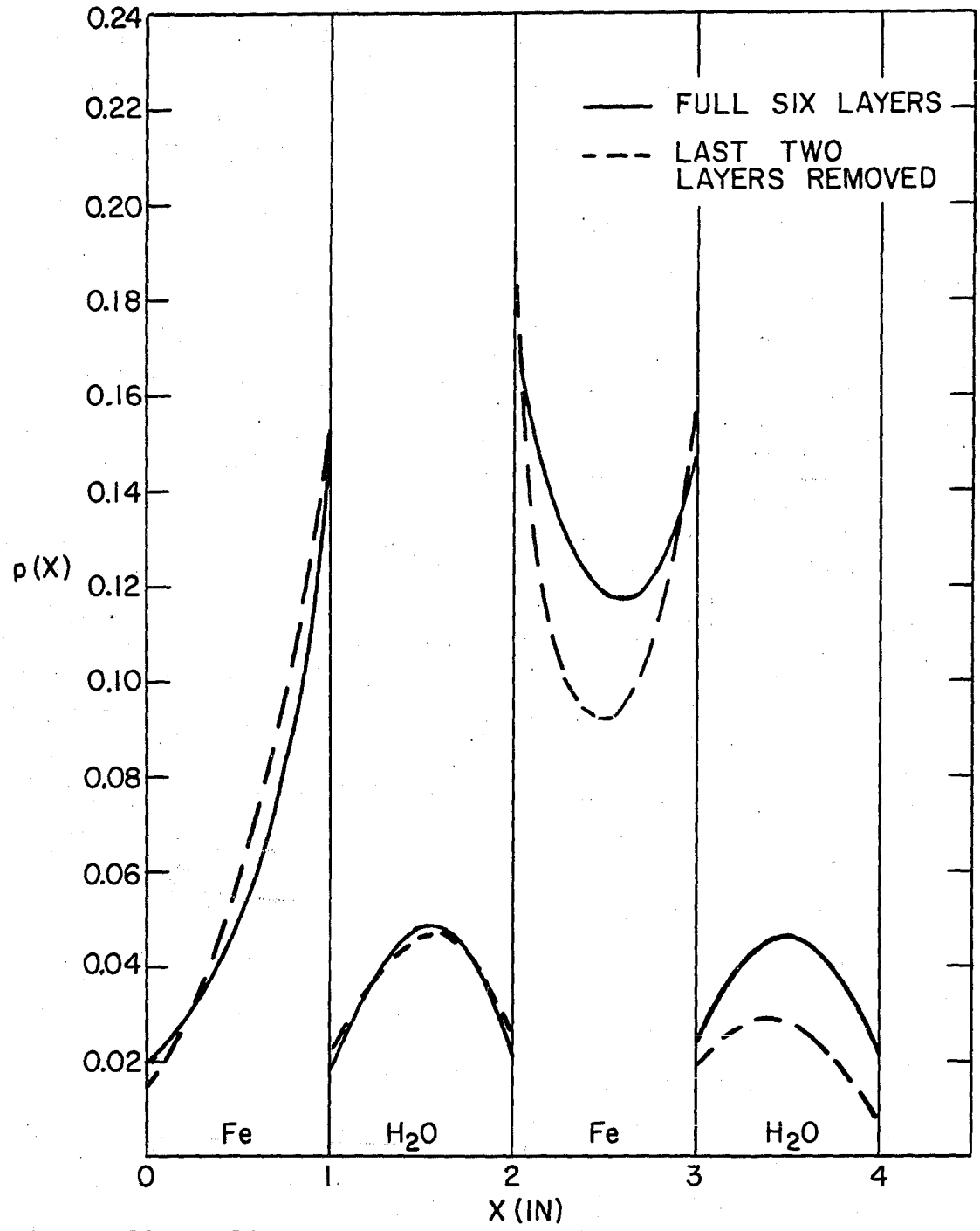

Figure 20. Effect upon the capture distribution of removing the third iron and third water layers--1 Mev normally incident source at x = 0

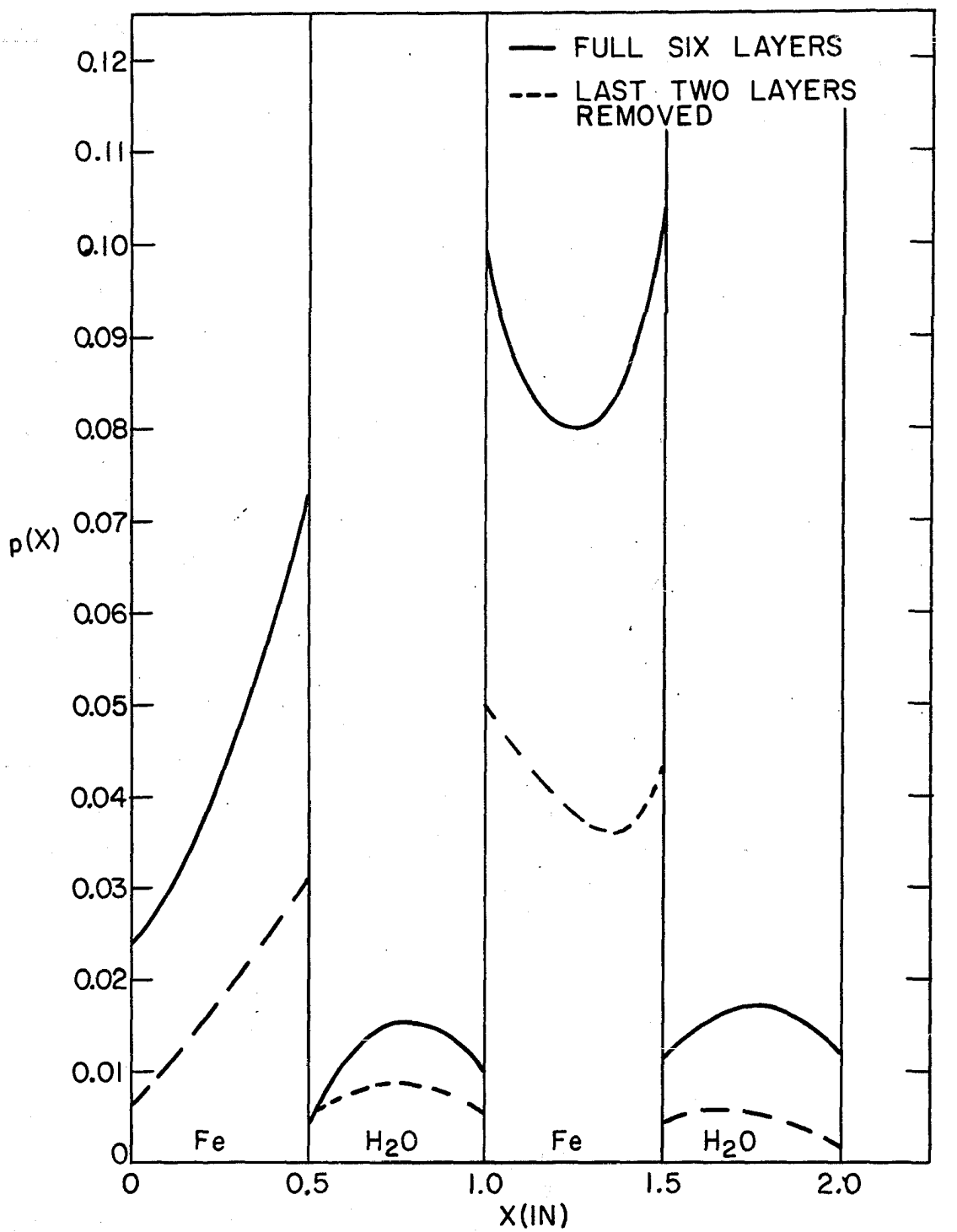

Figure 21. Effect upon the capture distribution of removing the third iron and third water layers--1 Mev cosine source at x = 0

large effect of removing the last two layers of the ½" geometry can be explained as follows: In the first instance, the last two layers are separated from the first four layers by a layer of water that is large (1") compared with the thermal neutron mean free path (0.1" to 0.2"). Thus, interaction between the last two layers and the first three layers is relatively small for this geometry. On the other hand, interaction in the smaller geometry between the last two layers and the first three layers through the intermediate ½" water layer is significant. Thus, when the last two layers are removed from the smaller array, many of the neutrons that otherwise would diffuse back to the first three layers from the last two layers are lost by transmission. Reduced capture rates in the first three layers result.

The results of these preliminary runs were used as a guide in outlining the principle problems that were run. Because of the large variation with energy of the neutron mean free path in the materials, it was recognized from the inception of this project that the capture distributions would be sensitive to changes in the energy of the source neutrons. In addition, the geometry, i.e., the number and sizes of the layers, also was expected to be important in determining the capture rates throughout the array. This last point was substantiated in the preliminary runs. Finally, the source angular spectrum would be expected to affect the capture

distributions. The preliminary runs indicated that this latter factor is considerably less significant than the first two (source energy and geometry).

On the basis of these considerations it was decided to concentrate in the remainder of this study upon the effect of the source energy. The geometry effect does not lend itself as readily to examination as does the effect of varying the source energy. This is particularly true in view of the limitations of the IBM-650 and of the program that was used in this work. Since the scope of this project did not admit the comprehensive examination of both source energy effects and geometry effects, a compromise was made in favor of the energy effects by examining in some detail the effect of source energy upon the capture distributions for two different geometries. The results of these calculations are presented in the following sections.

PRINCIPLE RUNS

In the principle calculations made in this study, the dependence of the capture distribution upon source energy was examined. Monoenergetic cosine sources of varying energies were used with two different geometries. These geometries were: I. six ½ inch layers, and II. six 1 inch layers. The temperature in all of these runs was 298°K, and the Δx spacing was 0.1". Source energies were 4.5, 1.0, 0.1, 0.04, 0.02, and 0.01 Mev for geometry I, and 4.5, 1.0, 0.1, 0.04, 0.025, and 0.01 Mev for geometry II. Running times were between 9 hours for 1400 histories using a 4.5 Mev source and geometry I, and 12 hours for 400 histories using a 0.025 Mev source and geometry II. Longer running times were required for larger water thicknesses and lower source energies.

Coefficients of variation were calculated for the data points by dividing the total number of histories into 16 to 32 groups and using these 16 (to 32) independent estimates of each data point to calculate the variances. Each problem was run by calculating n groups of N histories each, n = 16 to 32, where n times N is the total number of histories calculated for the problem. The n groups of output were then sorted into m groups of cards (n cards per group) with each group containing the same Δx's. The number m is equal to the total number of cards required to punch out the contents of the Δx stores at a rate of seven Δx's per card. These sorted cards were

used as input to an analysis of variance program obtained from the Iowa State University Statistical Laboratory. The output of this program gave the variance of the capture rate, $\bar{p}(x)$, in each Δx. Tables 4 and 5 show the resulting coefficients of variation for the data points. These data points were used in fitting the first set of capture curves that will be discussed in the following paragraphs.

After the program output cards had been used to calculate the point variances, the total capture weight, $P(x)$, deposited in each Δx interval was determined by summing the n contributions to each interval. This was done with an IBM-402 tabulating machine.

The capture probability points, $\bar{p}(x)$, were calculated from

$$\bar{p}(x) = P(x)/\Delta x\ N_T$$

where N_T is the total number of histories in the problem. Capture probability curves using the functions presented earlier, were then fitted to the $\bar{p}(x)$.

It should be pointed out that all of the data points in a given layer are used to fit the capture curve at a given x; therefore, the effective number of events used to establish a curve at a given x is larger than the number of events used to establish a single $\bar{p}(x)$. This reduces the variances of the curves as compared to the variances of the data points. The amount of this reduction is very difficult to determine, however, and consultation with members of the ISU Statistical

Table 4. Coefficients of variation for data points, $\bar{p}(x)$, in geometry I

		E(mev)					
	x(in)	4.5	1.0	0.1	0.04	0.02	0.01
	0.05	0.3845	0.2006	0.2390	0.2232		0.2242
	0.15	0.2402	0.1794	0.1499	0.2037	not	0.2012
Fe	0.25	0.3000	0.2748	0.1683	0.1667		0.1759
	0.35	0.3683	0.2092	0.1653	0.1422	calculated	0.1844
	0.45	0.2588	0.2197	0.1366	0.1716		0.1755
	0.55	0.1977	0.1929	0.1098	0.1274		0.1332
	0.65	0.1918	0.1291	0.1258	0.1165		0.1072
H_2O	0.75	0.2010	0.1447	0.0904	0.1076		0.1080
	0.85	0.1842	0.1140	0.1112	0.1315		0.1100
	0.95	0.1304	0.1383	0.1202	0.1190		0.1113
	1.05	0.1599	0.1562	0.1086	0.1062		0.1258
	1.15	0.1522	0.1530	0.1035	0.1421		0.1402
Fe	1.25	0.1298	0.1776	0.1079	0.1847		0.1105
	1.35	0.1546	0.1658	0.1285	0.1168		0.1074
	1.45	0.1622	0.1719	0.1307	0.1251		0.1224
	1.55	0.1433	0.1578	0.0894	0.0994		0.1156
	1.65	0.1446	0.1948	0.1052	0.1179		0.1312
H_2O	1.75	0.1914	0.1376	0.1318	0.0923		0.1161
	1.85	0.1445	0.1490	0.1201	0.0912		0.1234
	1.95	0.1512	0.1770	0.1063	0.1207		0.1181
	2.05	0.1795	0.1933	0.1610	0.1589		0.1582
	2.15	0.1754	0.1353	0.1288	0.1277		0.1675
Fe	2.25	0.1680	0.1535	0.1535	0.1593		0.1805
	2.35	0.1525	0.1280	0.1555	0.1573		0.1980
	2.45	0.1755	0.1648	0.1691	0.1919		0.1828

Table 4. (Continued)

	x(in)	E(mev) 4.5	1.0	0.1	0.04	0.02	0.01
H_2O	2.55	0.1720	0.1664	0.1472	0.1791		0.1787
	2.65	0.1947	0.1625	0.1412	0.1710		0.1729
	2.75	0.2014	0.1692	0.1453	0.1726		0.2437
	2.85	0.1989	0.1878	0.1421	0.2192		0.2778
	2.95	0.1980	0.2604	0.1611	0.2408		0.2631

Table 5. Coefficients of variation for data points, $\bar{p}(x)$, in geometry II

	E(mev) x(in)	4.5	1.0	0.1	0.04	0.025	0.01
	0.05	0.3565	0.8143	0.2177	0.2337	not	0.3286
	0.15	0.2905	0.3273	0.1928	0.2433		0.1439
	0.25	0.3628	0.2670	0.2503	0.2089	calculated	0.1829
	0.35	0.3250	0.1547	0.2187	0.1556		0.1751
	0.45	0.1681	0.3005	0.1675	0.1835		0.1880
Fe	0.55	0.2778	0.1719	0.2325	0.1492		0.1373
	0.65	0.3174	0.1731	0.1759	0.1288		0.1385
	0.75	0.2723	0.1590	0.1773	0.1210		0.1257
	0.85	0.3087	0.2123	0.1875	0.1215		0.1570
	0.95	0.2173	0.1425	0.1584	0.1629		0.1550
	1.05	0.1829	0.1662	0.1468	0.1697		0.1058
	1.15	0.1991	0.1462	0.1325	0.1421		0.1048
	1.25	0.1794	0.0835	0.1214	0.1261		0.1149
	1.35	0.1855	0.2217	0.0857	0.1113		0.1005
	1.45	0.1624	0.1827	0.0846	0.1410		0.1145
H_2O	1.55	0.2313	0.1456	0.1281	0.0918		0.1305
	1.65	0.1935	0.1112	0.1172	0.0871		0.1287
	1.75	0.1714	0.1444	0.1119	0.0958		0.0936
	1.85	0.1700	0.1514	0.1128	0.0980		0.1219
	1.95	0.1501	0.1383	0.1197	0.1009		0.1055
	2.05	0.1543	0.1730	0.1212	0.1065		0.1096
	2.15	0.2336	0.1964	0.1418	0.1325		0.1436
	2.25	0.1487	0.1575	0.1544	0.1296		0.1279
	2.35	0.1695	0.2574	0.1335	0.1266		0.1433
Fe	2.45	0.1608	0.3302	0.2273	0.1144		0.1846
	2.55	0.1453	0.1314	0.1542	0.1317		0.1794
	2.65	0.2093	0.1435	0.1234	0.1430		0.1307
	2.75	0.1409	0.1438	0.1411	0.1509		0.1452

Table 5. (Continued)

	E(mev) x(in)	4.5	1.0	0.1	0.04	0.025	0.01
Fe	2.85	0.1325	0.1235	0.1792	0.1580		0.1384
	2.95	0.2013	0.1794	0.1535	0.1543		0.1888
	3.05	0.1527	0.2174	0.1622	0.1437		0.1280
	3.15	0.1677	0.2705	0.1825	0.1727		0.1750
	3.25	0.1689	0.1452	0.1969	0.1572		0.1698
	3.35	0.2247	0.1856	0.1596	0.1890		0.1863
H_2O	3.45	0.1602	0.1626	0.1952	0.1783		0.1328
	3.55	0.1645	0.1742	0.1778	0.1684		0.1787
	3.65	0.1745	0.1941	0.1756	0.1909		0.2252
	3.75	0.2069	0.1721	0.2315	0.1668		0.1955
	3.85	0.2276	0.1064	0.2060	0.1743		0.2305
	3.95	0.1858	0.1497	0.2169	0.1627		0.2607
	4.05	0.2037	0.1515	0.2986	0.2442		0.2446
	4.15	0.1877	0.2012	0.2711	0.1892		0.3504
	4.25	0.2324	0.1701	0.2855	0.2530		0.2563
	4.35	0.1397	0.2009	0.2745	0.2983		0.2648
	4.45	0.1332	0.1320	0.2743	0.2651		0.4077
Fe	4.55	0.1836	0.2290	0.2304	0.2864		0.3116
	4.65	0.1761	0.1659	0.2870	0.2707		0.4134
	4.75	0.1495	0.0967	0.2433	0.2842		0.4249
	4.85	0.1473	0.2643	0.3059	0.2361		0.3243
	4.95	0.2165	0.1442	0.3016	0.3642		0.3180
	5.05	0.1977	0.2094	0.3252	0.4194		0.3642
H_2O	5.15	0.2051	0.1692	0.3910	0.5829		0.3843
	5.25	0.2119	0.2446	0.5111	0.3591		0.3943
	5.35	0.2673	0.2714	0.6875	0.4275		0.4475

Table 5 (Continued)

	E(mev) x(in)	4.5	1.0	0.1	0.04	0.025	0.01
H_2O	5.45	0.3318	0.3465	0.5402	0.4732		0.6374
	5.55	0.2568	0.4419	0.4325	0.4471		0.5736
	5.65	0.3511	0.2983	0.3259	0.6355		0.5201
	5.75	0.2478	0.4604	0.4632	0.7664		0.4511
	5.85	0.2974	0.4552	0.4918	0.4863		0.7086
	5.95	0.2555	0.4670	0.8854	0.4423		0.5393

Laboratory failed to produce a method of doing this with a practical amount of computing time. It can be stated only that the curves and correlations resulting from the data processing described in this section have less statistical uncertainty than the statistical uncertainties, as presented in Tables 4 and 5, of the original data points.

The capture distributions are most conveniently correlated as a function of the logarithm of the source energy. A so-called "lethargy" was used in the remainder of the work, where the lethargy of a neutron is defined by

$$U = \text{lethargy} = \ln (E_o/E)$$

Here, E is the energy of the neutron and E_o is a convenient reference energy. A reference energy of 10 Mev was used in this work to insure that all lethargies would be positive.

Capture probability points from the first curve fits (as a function of distance into each layer) were cross-plotted as a function of source lethargy at constant x. This was done for the mid-point of each Δx interval and for the surface points of each layer. These points were then fitted as a function of source lethargy by means of a fourth degree polynomial

$$p(U) = \sum_{i=0}^{4} A_i U^i$$

where p(U) is the capture probability per unit distance per incident neutron (at a given x) for a source of lethargy U.

The program used for these fits was obtained from the IBM-650 program library. Representative samples of the resulting curves are shown in Figures 22 and 23, along with the points that were used in the fitting calculations. The anomalous scatter in the surface points (x = 0 and 0.5 for geometry I and x = 0 and 1.0 for geometry II) should be noted. These curves will be discussed later. The smoothed lethargy curves were used to obtain new capture probability points as a function of x. (Note that, in Figures 22 and 23, x = 0 at the left face of each layer).

Throughout the calculations the uncertainty of the end points of the capture distribution in a given iron layer was of concern. The shape of the capture distribution curve in an iron layer is sensitive to the values of the end points, and statistical variations in the determination of some of these points had led, in some instances, to results that were not compatible with known qualitative features that should have been evident in the curves. The following considerations were used to improve the estimates of these end points, and, as will be pointed out later, the results, using the "corrected" end points, were qualitatively much superior to the first capture curves.

It became clear early in this work that most of the capture weight in these problems was being deposited by neutrons that had reached thermal equilibrium with the media through

Figure 22. Geometry I--sample plots (and smoothed curves) of p(u) = capture probability per unit distance per incident neutron, for source of lethargy u, (at constant x = position in each layer) vs source lethargy

Top row (left to right): First water layer, second water layer, third water layer

Bottom row (left to right): First iron layer, second iron layer, third iron layer

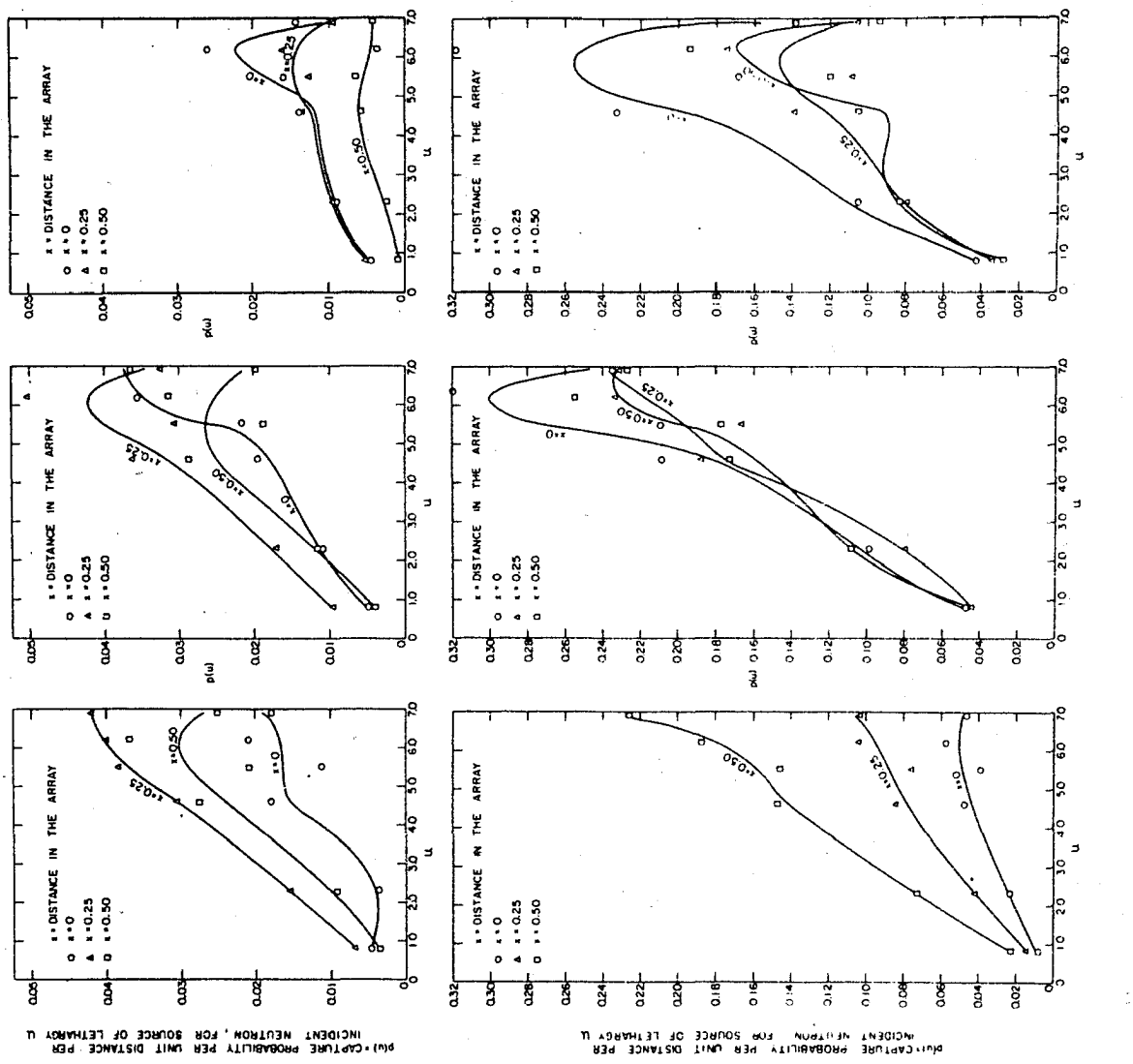
x = DISTANCE IN THE ARRAY
x = 0
x = 0.25
x = 0.50
p(u)
u

Figure 23. Geometry II--Sample plots (and smoothed curves) of $p(u)$ = capture probability per unit distance per incident neutron, for source of lethargy u, (at constant x = position in each layer) vs source lethargy

Top row (left to right): First water layer, second water layer, third water layer

Bottom row (left to right): First iron layer, second iron layer, third iron layer

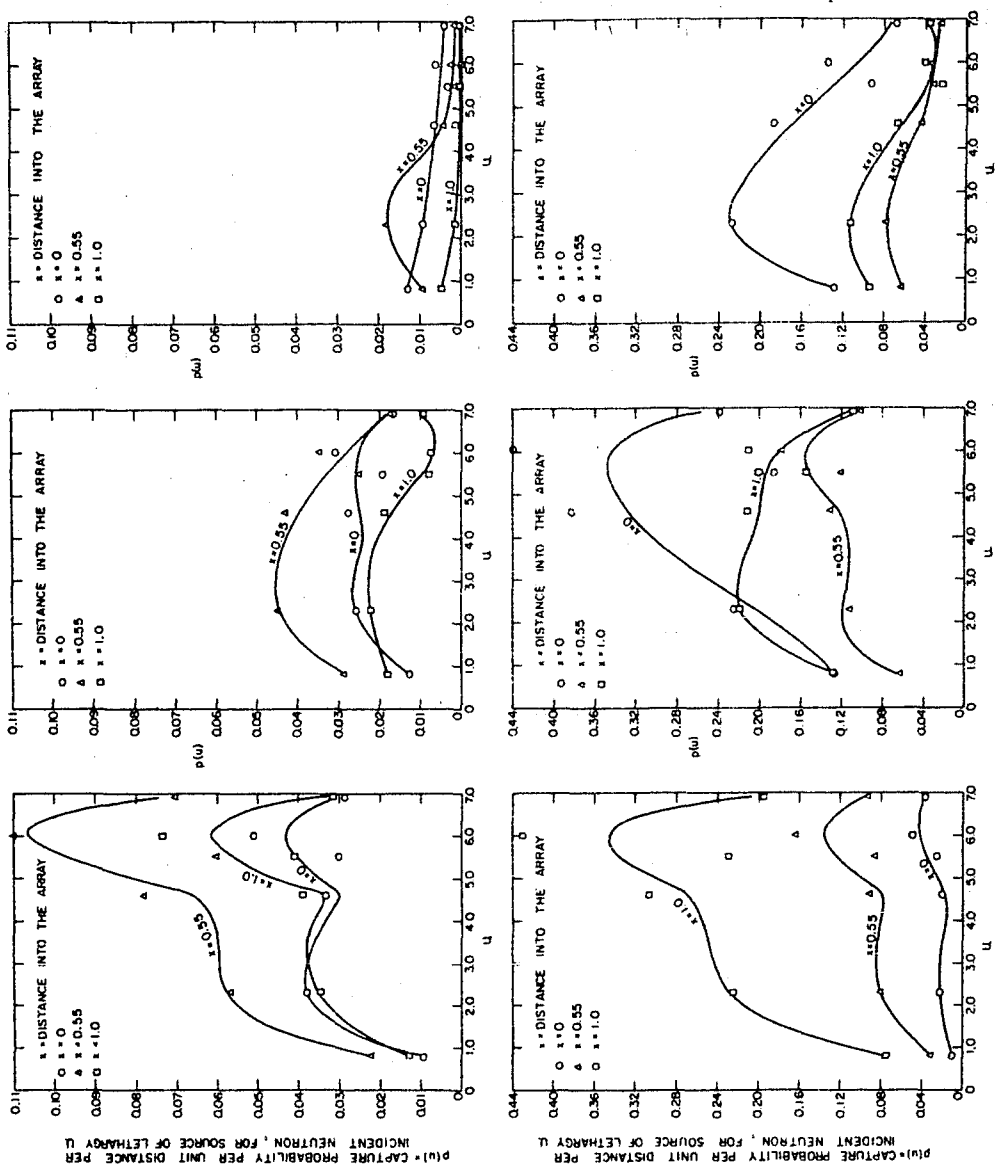
x = DISTANCE INTO THE ARRAY
x = 0
x = 0.55
x = 1.0
p(u) = CAPTURE PROBABILITY PER UNIT DISTANCE PER INCIDENT NEUTRON, FOR SOURCE OF LETHARGY u
u

which they were passing. One might expect that the energy spectrum of these thermalized neutrons at iron-water interfaces in the array would be approximately independent of which interface was being considered. If this constancy holds, an effective capture cross section can be defined such that the capture rate at any interface is given by the product of this cross section and the flux of thermal neutrons at the interface. This effective capture cross section and the ratio of the capture rate in iron to the capture rate in water at an interface will be constant to the extent that the energy spectrum of the neutrons being captured is constant.

If this spectrum is Maxwellian and if the capture cross sections of iron and water vary inversely as the square root of the neutron energy, then the ratio, r, of the iron capture rate to the water capture rate at an interface will be given by (24)

$$r = \phi\ (\Sigma_{a_T})_{Fe} / \phi\ (\Sigma_{a_T})_{H_2O} = \frac{(\Sigma_{a_T})_{Fe}}{(\Sigma_{a_T})_{H_2O}} = 9.74$$

where Σ_{a_T} is the macroscopic thermal neutron capture cross section (15), and ϕ is the thermal neutron flux at the interface.

Tables 6 and 7 show the ratio of iron capture rate to water capture rate at the five iron-water interfaces for geometries I and II. These ratios were calculated from the

Table 6. Ratio of capture rate in iron to capture rate in water at the iron-water interfaces of geometry I

Interface (Figure 1)	E(Mev) 4.5	1.0	0.1	0.04	0.02	0.01
t_1	4.9	19.6	8.3	13.1	9.0	12.6
t_2	12.7	10.6	7.6	10.0	9.3	9.3
t_3	9.7	9.9	8.9	8.2	7.1	6.2
t_4	10.7	9.0	8.1	9.0	10.2	7.0
t_5	5.8	9.0	7.5	7.5	7.4	9.5

Table 7. Ratio of capture rate in iron to capture rate in water at the iron-water interfaces of geometry II

Interface (Figure 1)	E(Mev) 4.5	1.0	0.1	0.04	0.025	0.01
t_1	8.1	5.9	9.2	7.6	8.4	6.8
t_2	10.0	6.5	9.8	4.6	6.4	7.6
t_3	10.2	8.5	7.8	8.4	6.8	6.4
t_4	7.1	10.3	9.9	11.3	17.3	7.0
t_5	7.4	12.5	10.1	7.0	6.5	8.4

original curve fits (as a function of x). A stability in this ratio is evident. Fifty-seven percent of the ratios lie within $\pm$ 20% of 9.74, and an additional 37% of the ratios lie within $\pm$ 40% of 9.74.

It would be expected that the water capture data would have better statistical accuracy than the iron capture data because of the larger number of collisions that occur in water than in iron. This is borne out in Tables 4 and 5. In addition, the spatial variation of the capture curves is much smaller in water layers than in iron layers. Consequently,

the end points of capture curves in water layers are much less sensitive to statistical fluctuations in the data than are the end points of capture curves in iron layers. Thus, the end-points of the capture curves in the water layers are more accurately determined than the end-points of the capture curves in the iron layers.

The considerations of the last few paragraphs were used to "correct" the end points of the iron capture probability curves. The water capture probability points, $\bar{p}(x)$, that were obtained from the data that had been smoothed as a function of source lethargy (Figures 22 and 23) were re-fitted by $p(x) = A + Bx + Cx^2$. The end points from these curves were then assumed to be 1/9.74 times the corresponding iron capture probabilities at the interfaces, i.e., the iron capture probability at each interface was set to 9.74 times the water capture probability at that interface, as obtained from the final water curve fits. Intermediate points in each iron layer were obtained from the lethargy curves (Figures 22 and 23). In general, there was relatively little difference between the corrected iron end-points and the end-points that were obtained from the lethargy curves.

In a few instances (approximately 15% of all iron end-points), the corrected end-points appeared to be somewhat unreasonable in comparison with the other points in the layers. For these cases, the values of the end points were adjusted

rather arbitrarily so as to meet the following requirements (iron layers):

1. The end-points must be reasonable in comparison with other points in the layer.
2. The right end-point should not have a larger value than the left end-point for a given layer (excluding, of course, the first iron layer).
3. The iron capture rate at $x = t_4$ should not be greater than the iron capture rate at $x = t_3$.
4. A minimum should exist in the capture curves in the iron layers.

These qualitative features are discussed in a later section. The adjustments just described resulted in changes of less than 20% for 95% of the anomalous end-points. The maximum adjustment was 50%.

After these end-point adjustments, the capture probability points in the iron layers were re-fitted as a function of x. The resulting capture curve parameters were fitted by a fourth degree polynomial, as a function of source lethargy. The resulting smoothed parameters were used to calculate a final set of capture probability curves as a function of distance into each layer.

Figures 24 to 27 show the capture probability curves for these problems. The circles in these figures are the original data points, $\bar{p}(x)$, the solid curves are the first probability

Figure 24. Geometry I, water layers--Capture probability per unit distance per incident neutron vs x = distance into the layer

Roman numerals (e.g., II-0.04) = layer number (left to right), attached arabic numerals = source energy (Mev)

I = First water layer

II = Second water layer

III = Third water layer

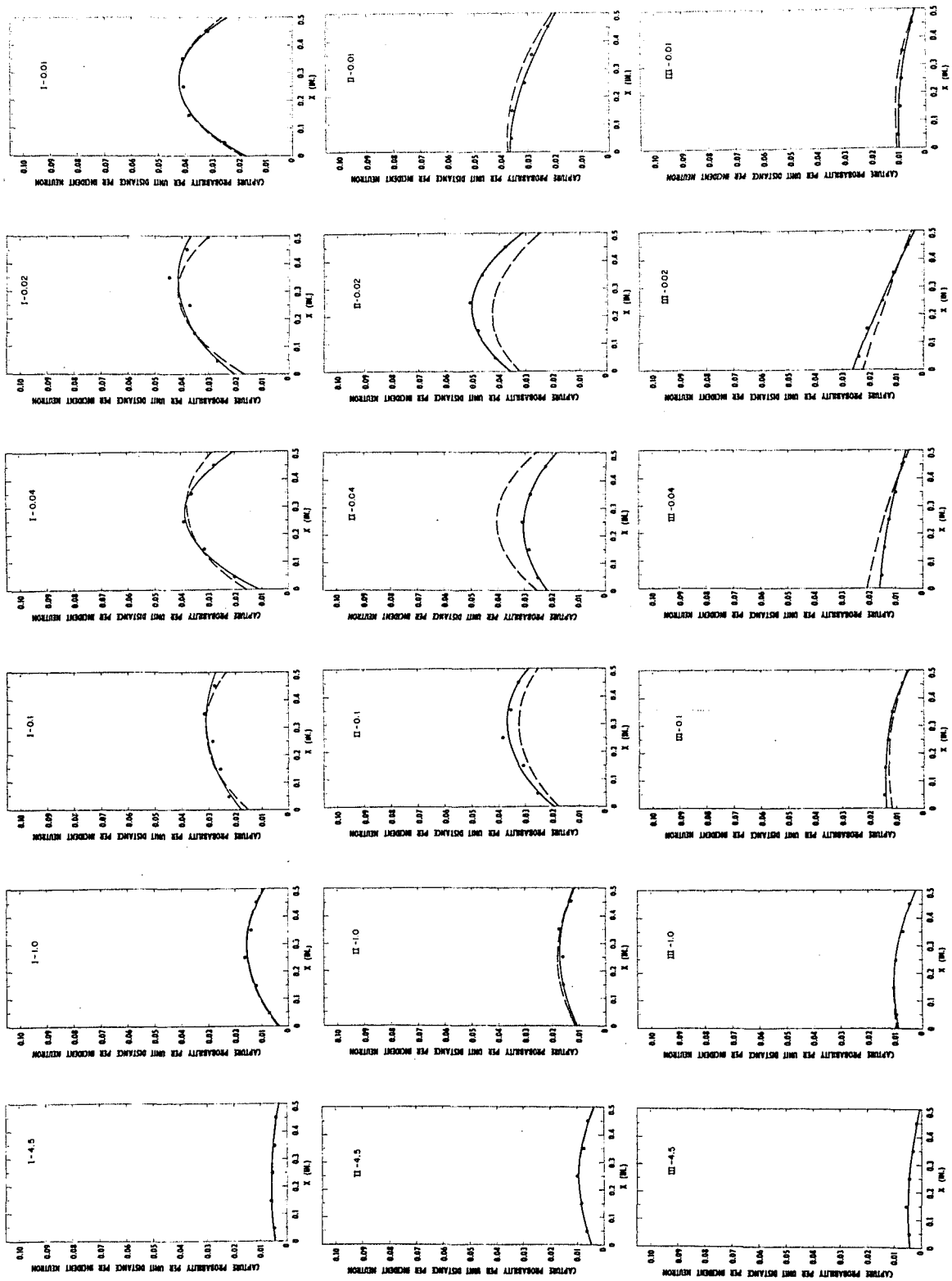
I-0.01
II-0.01
III-0.01
I-0.02
II-0.02
III-002
I-0.04
II-0.04
III-004
I-0.1
II-0.1
III-0.1
I-1.0
II-1.0
III-1.0
I-4.5
II-4.5
III-4.5
X (IN.)
CAPTURE PROBABILITY PER UNIT DISTANCE PER INCIDENT NEUTRON

Figure 25. Geometry I, iron layers--Capture probability per unit distance per incident neutron vs x = distance into the layer

Roman numerals (e.g., II-0.04) = layer number (left to right), attached Arabic numerals = source energy (Mev)

I = First iron layer

II = Second iron layer

III = Third iron layer

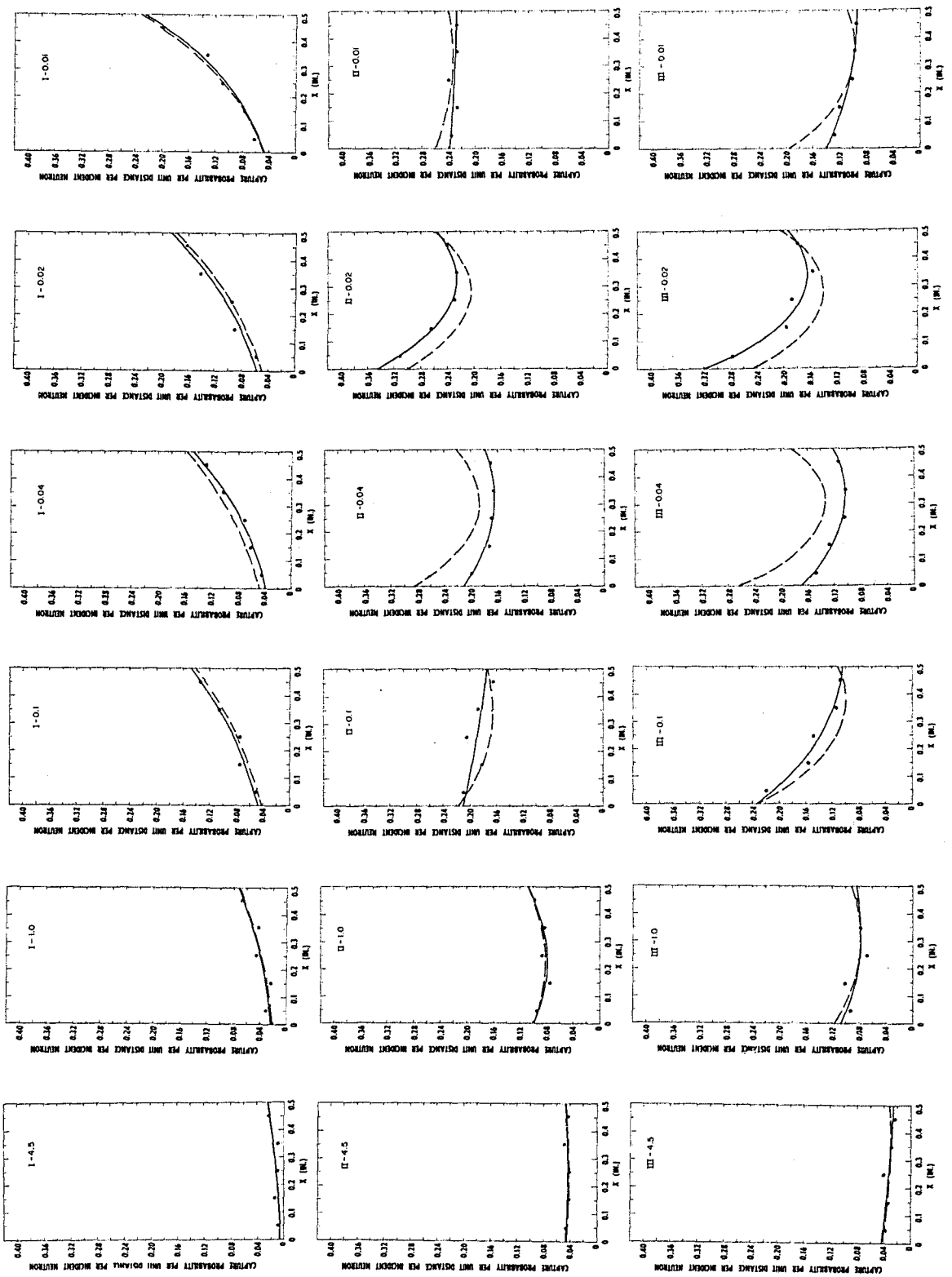
I-0.01
II-0.01
III-0.01
I-0.02
II-0.02
III-0.02
I-0.04
II-0.04
III-0.04
I-0.1
II-0.1
III-0.1
I-1.0
II-1.0
III-1.0
I-4.5
II-4.5
III-4.5
X (IN.)
CAPTURE PROBABILITY PER UNIT DISTANCE PER INCIDENT NEUTRON

Figure 26. Geometry II, water layers--Capture probability per unit distance per incident neutron vs x = distance into the layer

Roman numerals (e.g., II-0.04) = layer number (left to right), attached Arabic numerals = source energy (Mev)

I = First water layer

II = Second water layer

III = Third water layer

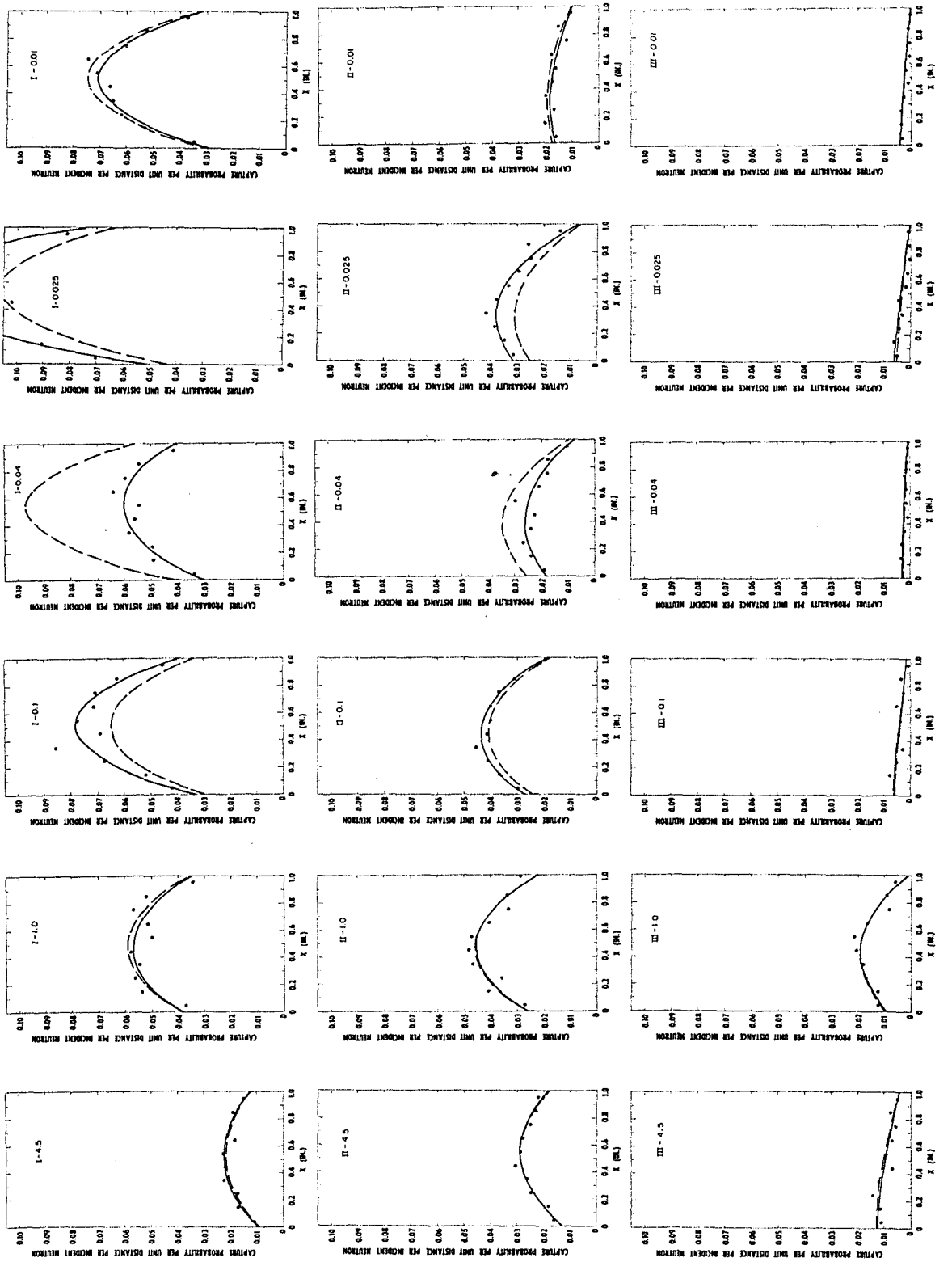
I-0.01
II-0.01
III-0.01
I-0.025
II-0.025
III-0.025
I-0.04
II-0.04
III-0.04
I-0.1
II-0.1
III-0.1
I-1.0
II-1.0
III-1.0
I-4.5
II-4.5
III-4.5
CAPTURE PROBABILITY PER UNIT DISTANCE PER INCIDENT NEUTRON
X (IN.)

Figure 27. Geometry II, iron layers--Capture probability per unit distance per incident neutron vs x = distance into the layer

Roman numerals (e.g., II-0.04) = layer number (left to right), attached Arabic numerals = source energy (Mev)

I = First iron layer

II = Second iron layer

III = Third iron layer

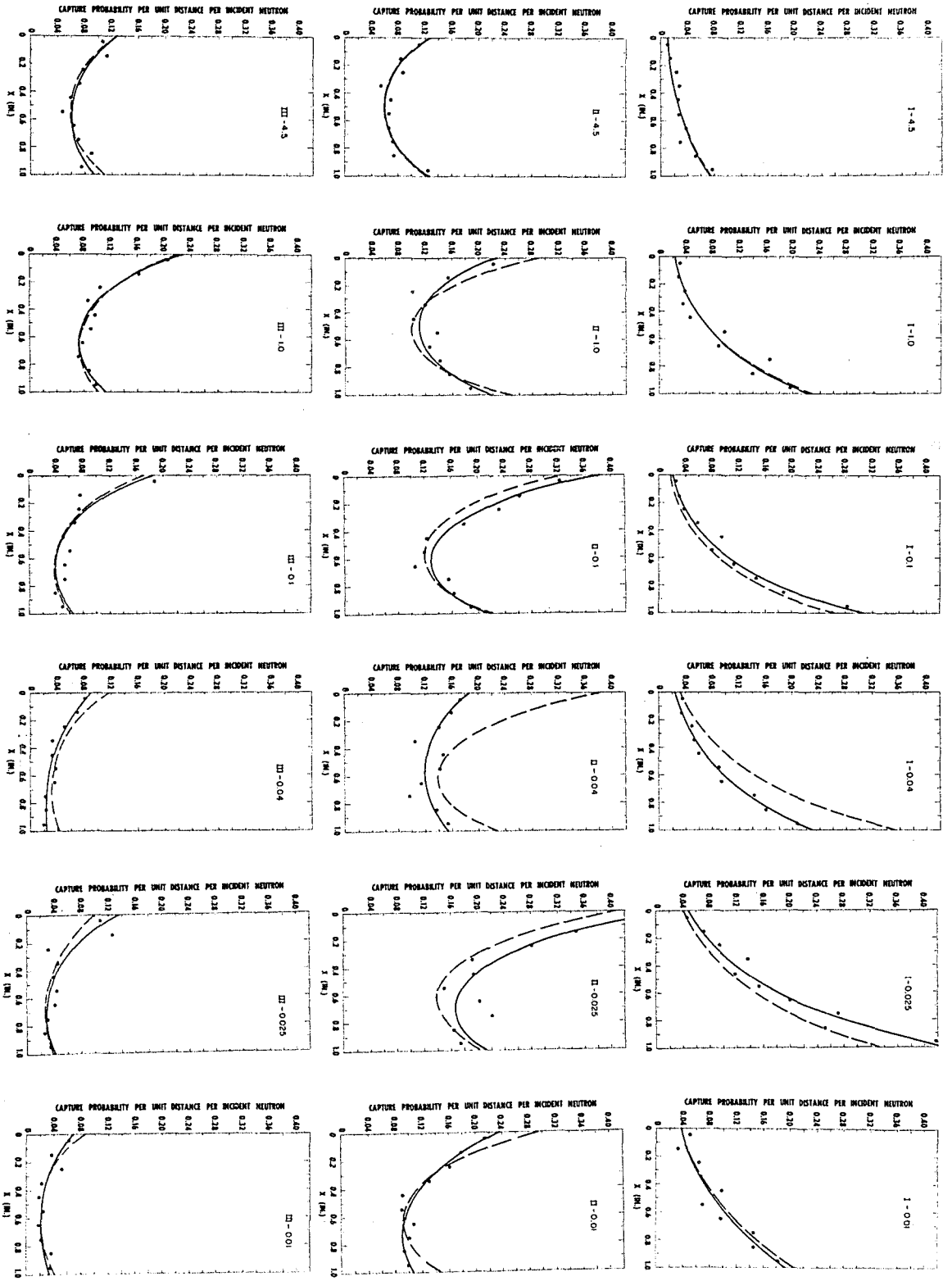
CAPTURE PROBABILITY PER UNIT DISTANCE PER INCIDENT NEUTRON
X (M)
III-4.5
II-4.5
I-4.5
III-1.0
II-1.0
I-1.0
III-0.1
II-0.1
I-0.1
III-0.04
II-0.04
I-0.04
III-0.025
II-0.025
I-0.025
III-0.01
II-0.01
I-0.01

curves fitted to the $\bar{p}(x)$, and the dashed curves are the final curves obtained after the processing described in this section. The dashed curves were obtained from the final parameter correlations as a function of source lethargy. In Figures 24 to 27, the Roman numerals (e.g., II-0.04) indicate the layer number (from left to right), and the Arabic numerals give the source energy in Mev.

Figures 28 to 39 give the final parameter correlations as a function of source lethargy. These figures can be used to find the parameters for the capture probability curves in geometries I and II for any source energy between 0.01 Mev and 4.5 Mev, where the capture probability curves are given by

$$\text{Water layers:} \quad p(x) = A + Bx + Cx^2$$

$$\text{First iron layer:} \quad p(x) = \alpha e^{\beta x}$$

$$\text{Other iron layers:} \quad p(x) = \alpha \cosh \beta(x-x_o)$$

Here x is in inches, x = 0 at the left face of the layer, and p(x) is the capture probability per unit distance per incident neutron.

The equations for the curves in Figures 28 to 39 are as follows:

Geometry I

First water layer

$$A = 0.020148-0.029866U+0.015275U^2-0.0026889U^3+0.00015932U^4$$

$$B = -0.11985+0.24169U-0.10610U^2+0.019502U^3-0.0012072U^4$$

$$C = 0.15250-0.32869U+0.13713U^2-0.024243U^3+0.0014336U^4$$

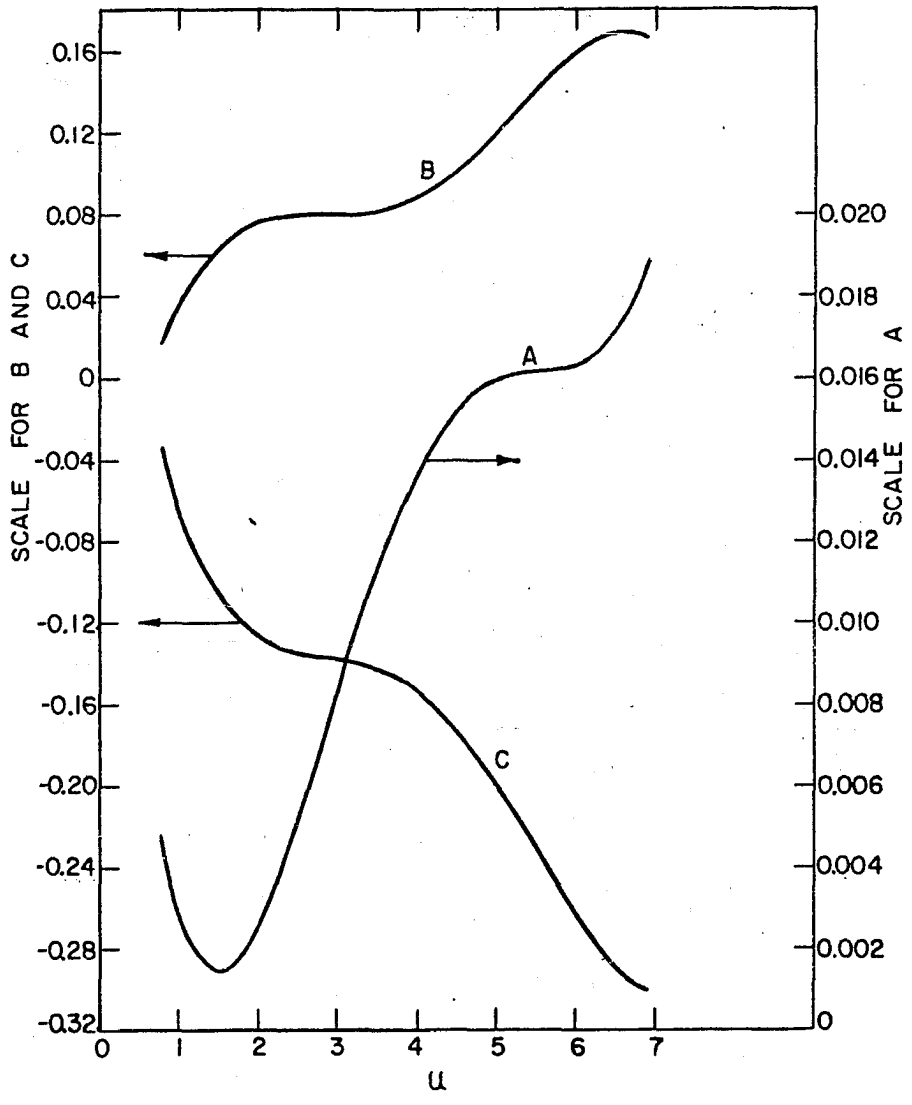

Figure 28. First water layer of geometry I--parameters for p(x) = capture probability per unit distance per incident neutron = $A+Bx+Cx^2$ vs U = source lethargy = $\ln(10/E_o)$, E_o = source energy (Mev), x in inches

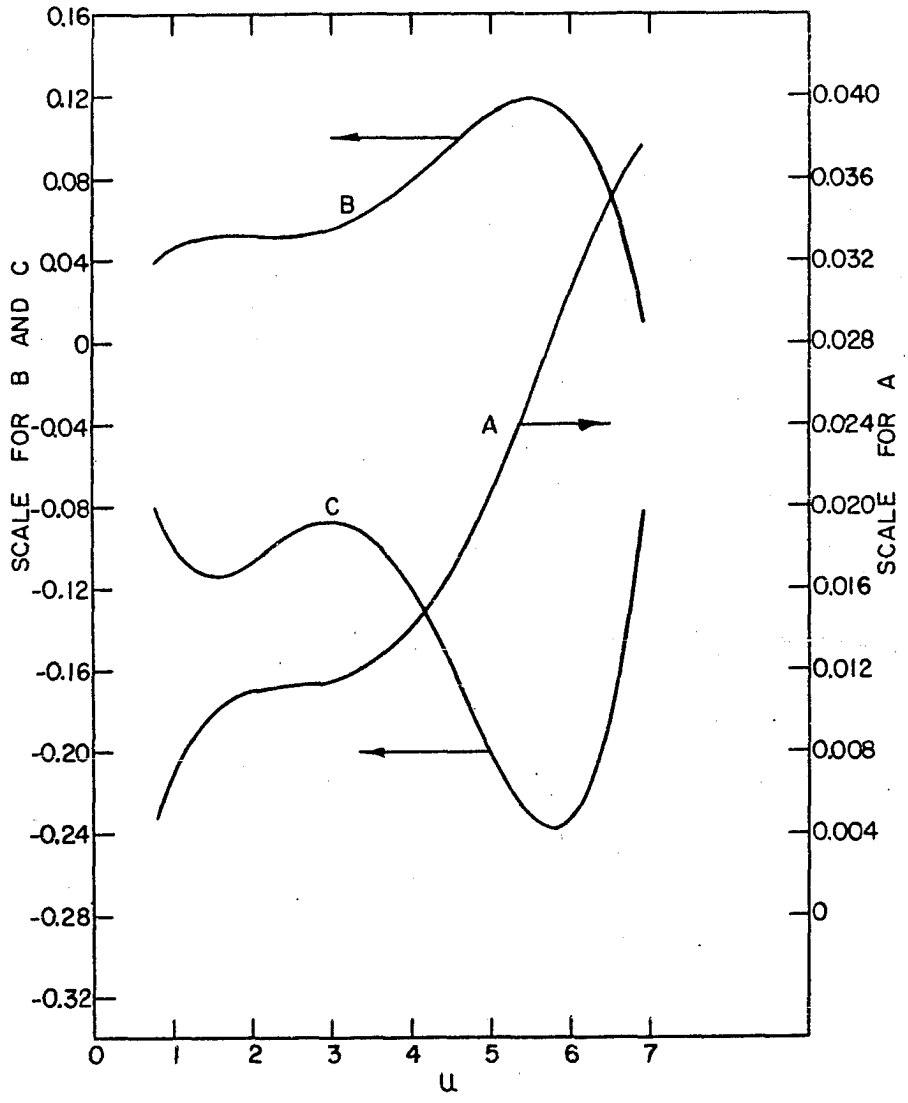

Figure 29. Second water layer of geometry I--parameters for $p(x)$ = capture probability per unit distance per incident neutron = $A+Bx+Cx^2$ vs U = source lethargy = $\ln(10/E_o)$, E_o = source energy (Mev), x in inches

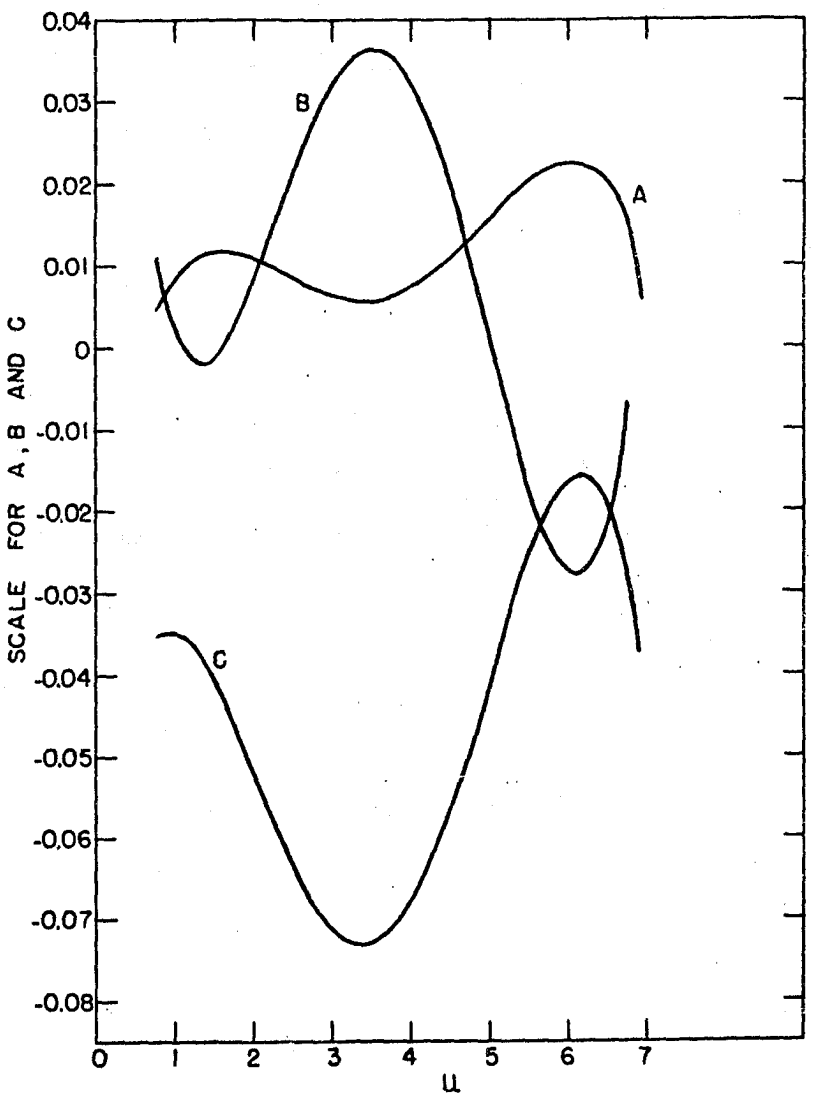

Figure 30. Third water layer of geometry I--parameters for p(x) = capture probability per unit distance per incident neutron = $A+Bx+Cx^2$ vs U = source lethargy = $\ln(10/E_o)$, E_o = source energy (Mev), x in inches

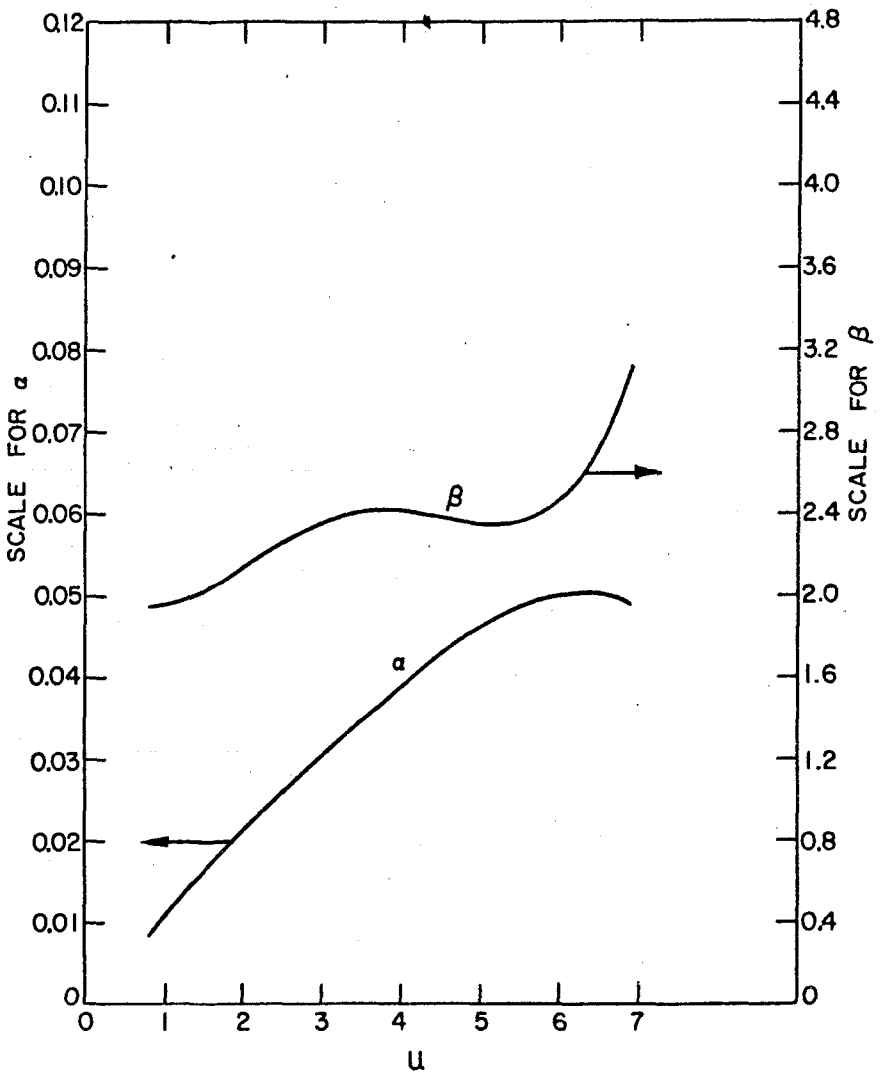

Figure 31. First iron layer of geometry I--parameters for p(x) = capture probability per unit distance per incident neutron = $\alpha e^{\beta x}$ vs U = source lethargy = $\ln(10/E_o)$, E_o = source energy (Mev), x in inches

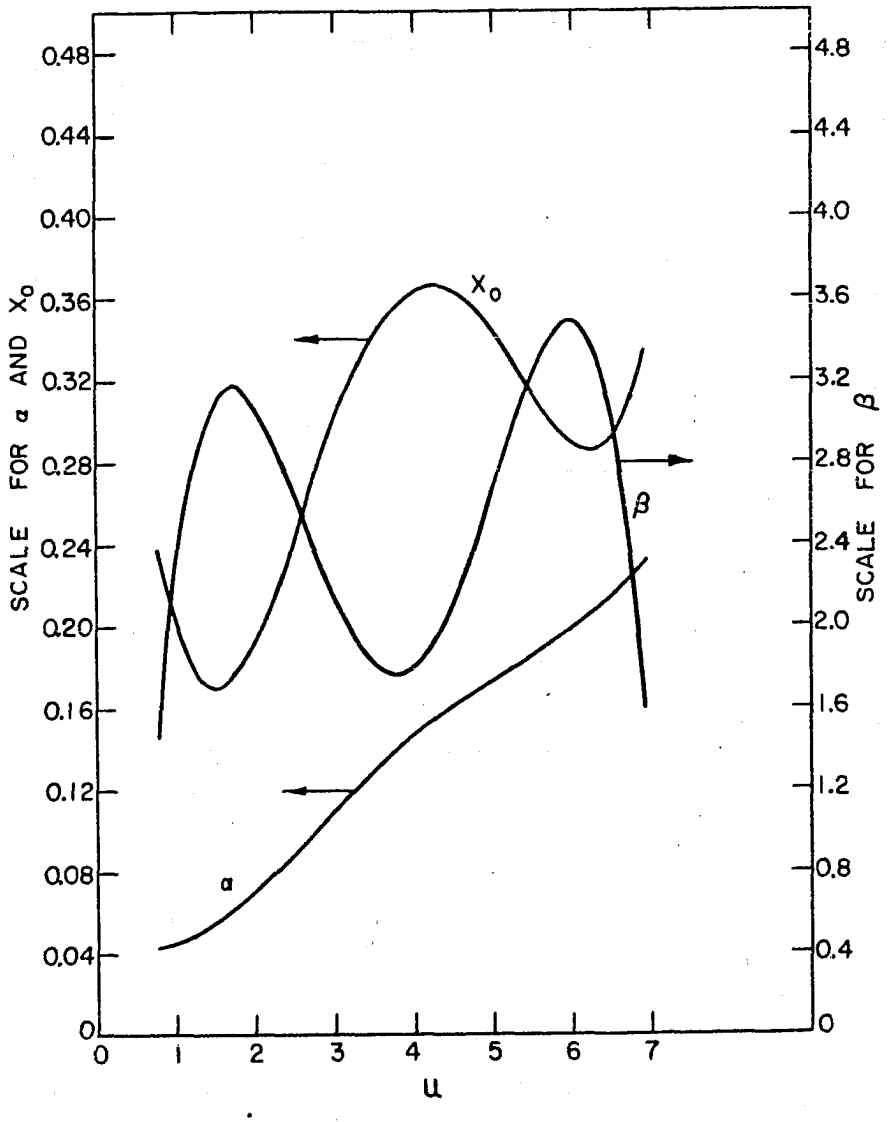

Figure 32. Second iron layer of geometry I--parameters for $p(x)$ = capture probability per unit distance per incident neutron = $\alpha \cosh \beta(x-x_0)$ vs U = source lethargy = $\ln(10/E_0)$, E_0 = source energy (Mev), x in inches

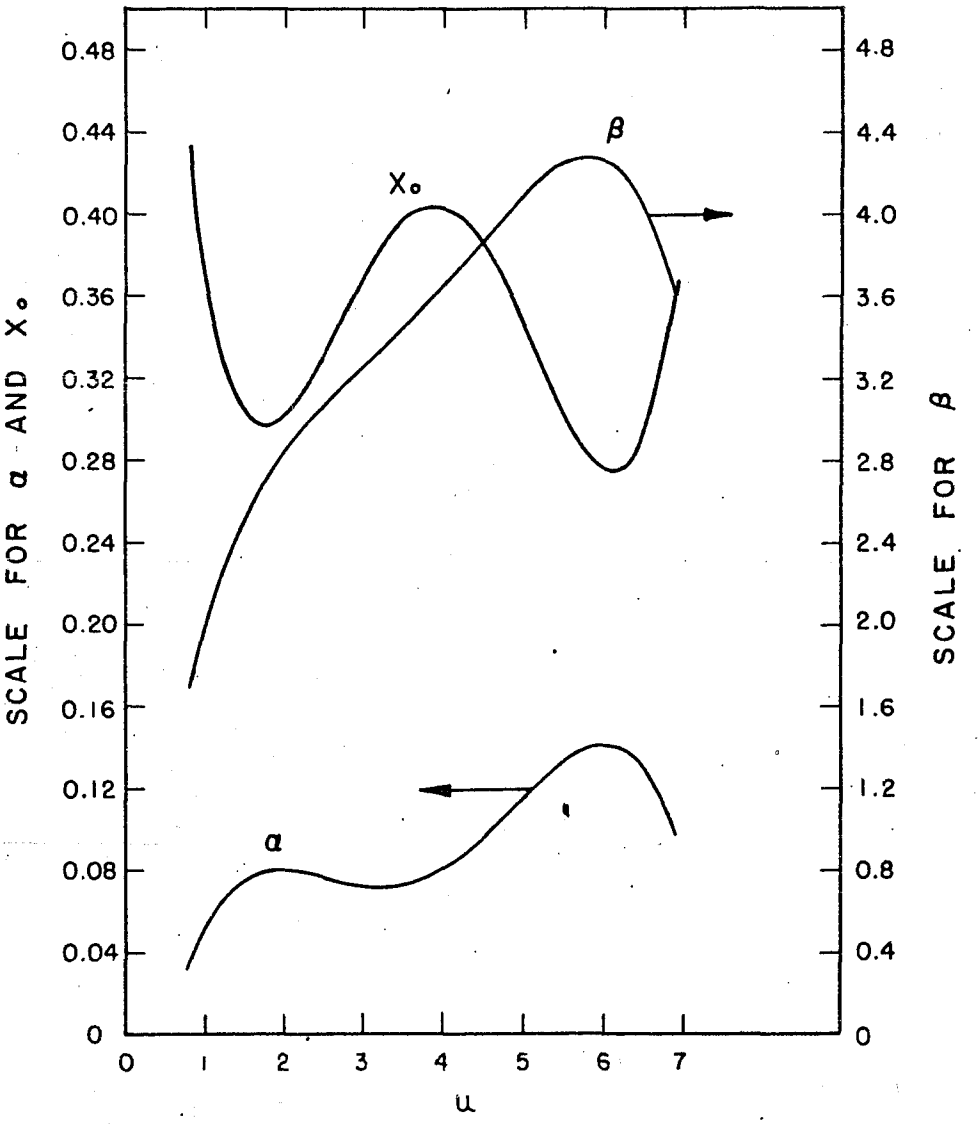

Figure 33. Third iron layer of geometry I--parameters for p(x) = capture probability per unit distance per incident neutron = $\alpha \cosh \beta(x-x_o)$ vs U = source lethargy = $\ln(10/E_o)$, E_o = source energy (Mev), x in inches

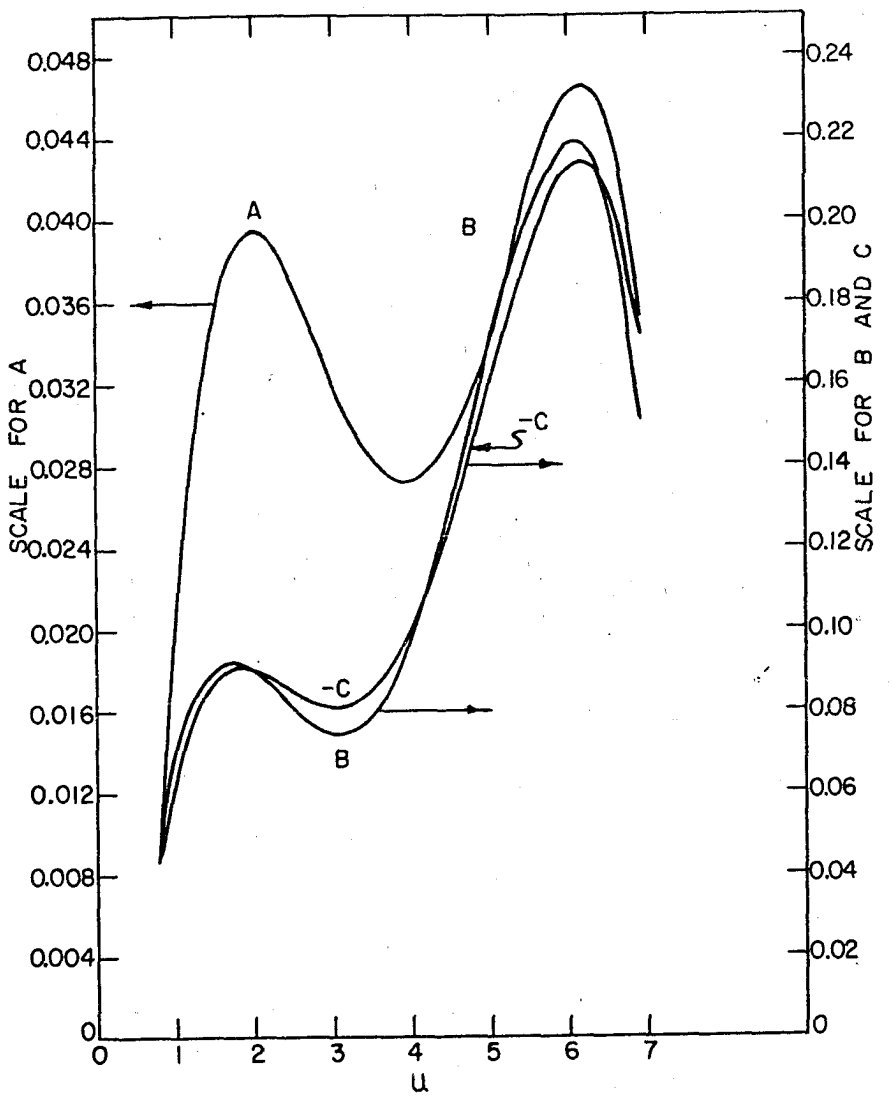

Figure 34. First water layer of geometry II--parameters for p(x) = capture probability per unit distance per incident neutron = $A+Bx+Cx^2$ vs U = source lethargy = $\ln(10/E_o)$, E_o = source energy (Mev), x in inches

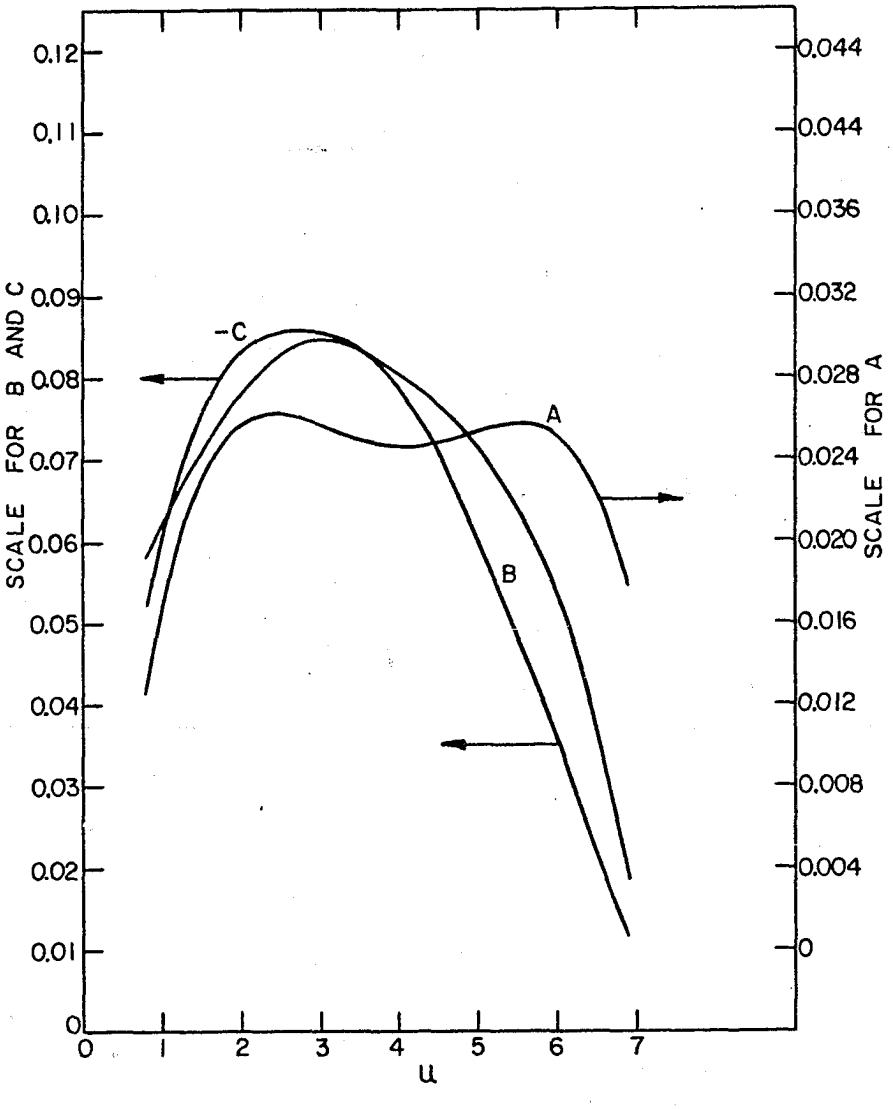

Figure 35. Second water layer of geometry II--parameters for $p(x)$ = capture probability per unit distance per incident neutron = $A+Bx+Cx^2$ vs U = source lethargy = $\ln(10/E_o)$, E_o = source energy (Mev), x in inches

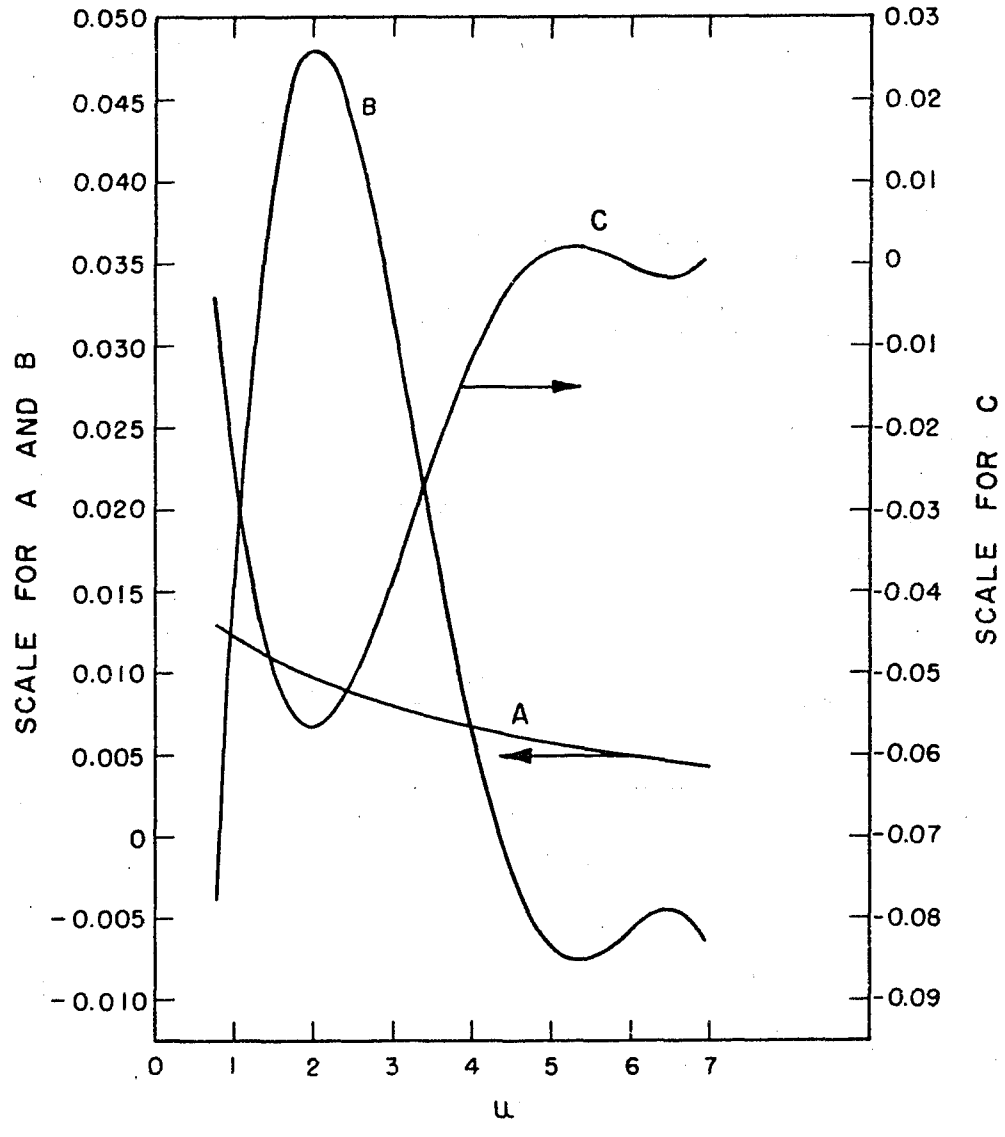

Figure 36. Third water layer of geometry II--parameters for $p(x)$ = capture probability per unit distance per incident neutron = $A+Bx+Cx^2$ vs U = source lethargy = $\ln(10/E_o)$, E_o = source energy (Mev), x in inches

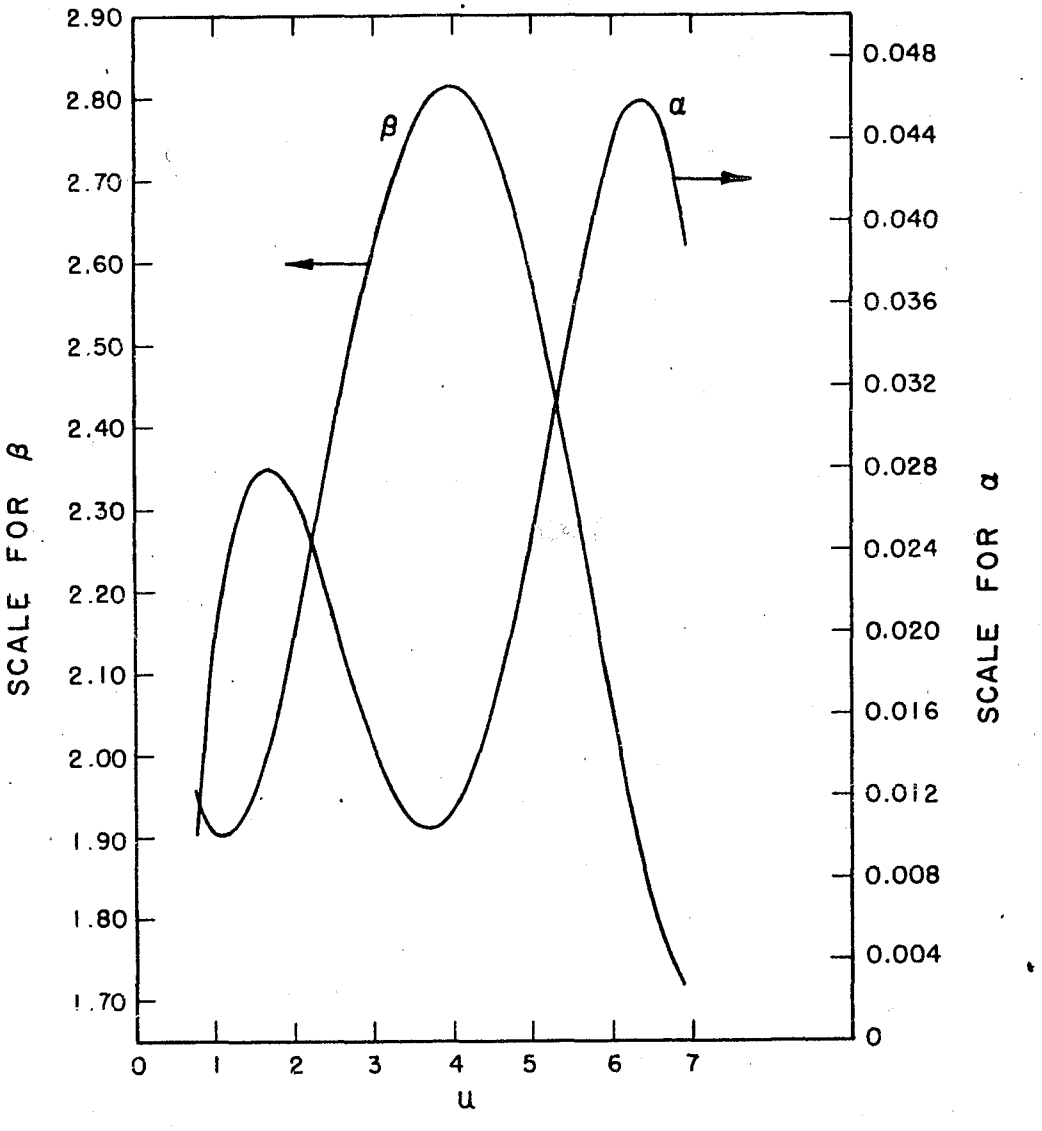

Figure 37. First iron layer of geometry II--parameters for p(x) = capture probability per unit distance per incident neutron = $\alpha e^{\beta x}$ vs U = source lethargy = $\ln(10/E_o)$, E_o = source energy (Mev), x in inches

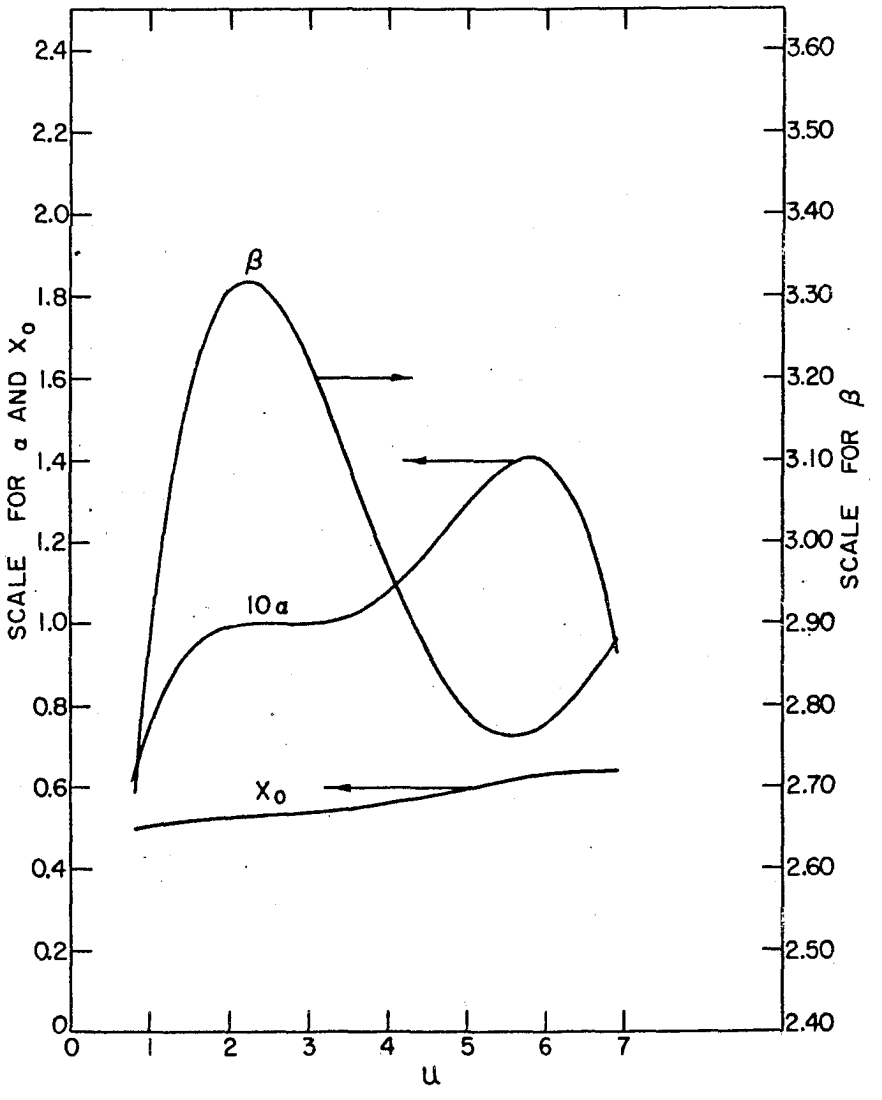

Figure 38. Second iron layer of geometry II--parameters for $p(x)$ = capture probability per unit distance per incident neutron = $\alpha \cosh \beta(x-x_o)$ vs U = source lethargy = $\ln(10/E_o)$, E_o = source energy (Mev), x in inches

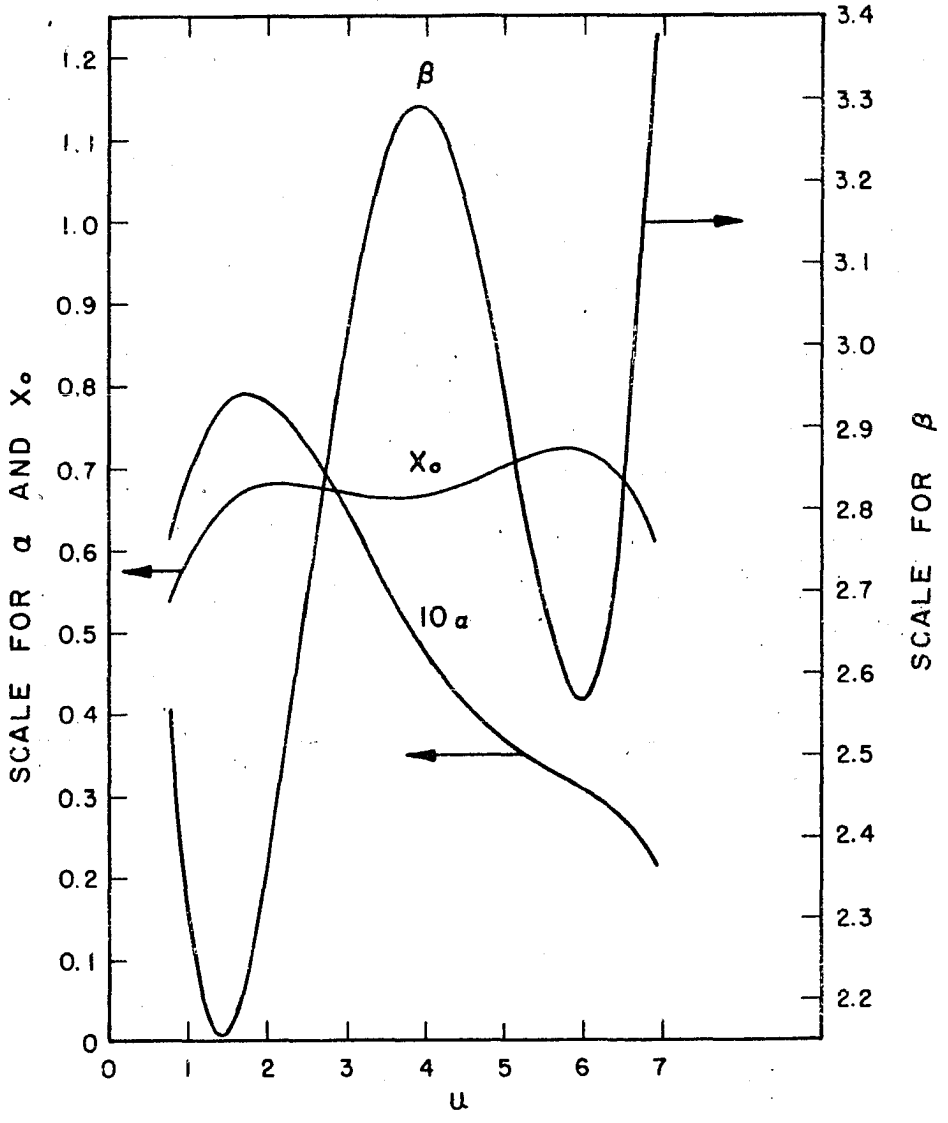

Figure 39. Third iron layer of geometry II--parameters for p(x) = capture probability per unit distance per incident neutron = $\alpha \cosh \beta(x-x_o)$ vs U = source lethargy = $\ln(10/E_o)$, E_o = source energy (Mev), x in inches

Second water layer

$$A = -0.010530+0.028008U-0.012967U^2+0.0024755U^3-0.00015046U^4$$

$$B = -0.022785+0.12646U-0.075225U^2+0.018165U^3-0.0014234U^4$$

$$C = 0.10058-0.37228U+0.21745U^2-0.048703U^3+0.0035433U^4$$

Third water layer

$$A = -0.027629+0.063275U-0.034098U^2+0.0070187U^3-0.00047649U^4$$

$$B = 0.099616-0.18496U+0.10976U^2-0.023316U^3+0.0015946U^4$$

$$C = -0.071129+0.086423U-0.063919U^2+0.014879U^3-0.0010617U^4$$

First iron layer

$$\alpha = -0.0025743+0.015906U-0.0029019U^2+0.00056628U^3-0.000046922U^4$$

$$\beta = 2.2402-0.73110U+0.56472U^2-0.13255U^3+0.0099479U^4$$

Second iron layer

$$\alpha = 0.061470-0.050526U+0.040881U^2-0.0076542U^3+0.00047975U^4$$

$$\beta = -4.7957+11.9908U-6.0812U^2+1.1835U^3-0.077532U^4$$

$$x_o = 0.57717-0.66842U+0.35627U^2-0.067594U^3+0.0042400U^4$$

Third iron layer

$$\alpha = -0.11301+0.27244U-0.13417U^2+0.026715U^3-0.0017897U^4$$

$$\beta = -0.15850+3.1550U-1.2289U^2+0.23327U^3-0.015944U^4$$

$$x_o = 0.89617-0.87482U+0.43124U^2-0.081658U^3+0.0052045U^4$$

Geometry II

First water layer

$$A = -0.073950+0.15298U-0.070769U^2+0.012948U^3-0.00081000U^4$$

$$B = -0.14034+0.36548U-0.19639U^2+0.041289U^3-0.0028313U^4$$

$$C = 0.12391-0.32083U+0.16613U^2-0.034283U^3+0.0023245U^4$$

Second water layer

$$A = -0.015493+0.049535U-0.020809U^2+0.0036375U^3-0.00022621U^4$$

$$B = 0.042467+0.018143U+0.0030349U^2-0.0018953U^3+0.00014207U^4$$

$$C = 0.0023756-0.093051U+0.035072U^2-0.0056974U^3+0.00036269U^4$$

Third water layer

$$A = 0.015227-0.0032838U+0.00030567U^2+0.000000718U^3 -0.000001273U^4$$

$$B = -0.12973+0.22296U-0.093266U^2+0.014693U^3-0.00079435U^4$$

$$C = 0.12694-0.23359U+0.099055U^2-0.015767U^3+0.00086027U^4$$

First iron layer

$$\alpha = -0.057682+0.13126U-0.067311U^2+0.013020U^3-0.00083016U^4$$

$$\beta = 2.7346-1.7004U+1.0808U^2-0.21613U^3+0.013336U^4$$

Second iron layer

$$\alpha = -0.039410+0.18706U-0.089785U^2+0.017982U^3-0.0012311U^4$$

$$\beta = 1.4519+2.1269U-0.80463U^2+0.11361U^3-0.0054095U^4$$

$$x_o = 0.45018+0.086131U-0.038467U^2+0.0080942U^3-0.00054379U^4$$

Third iron layer

$$\alpha = 0.0067343+0.10045U-0.045487U^2+0.0073951U^3-0.00041559U^4$$

$$\beta = 4.8196-4.5840U+2.5730U^2-0.51818U^3+0.034378U^4$$

$$x_o = 0.19273+0.62853U-0.28439U^2+0.052977U^3-0.0034318U^4$$

TRANSMISSION AND REFLECTION DATA

Transmission and reflection data were obtained as a by-product of the principle runs. The paucity of events contributing to many of the transmission and reflection data means that much of this information is of questionable quantitative value. Furthermore, the primary interest in this study was the determination of the capture distributions. Therefore, the transmission and reflection data were not processed extensively. These data are presented in this section along with qualitative comments on certain features and trends that are evident in the data.

Figures 40 and 41 show the variation of the reflection and transmission fractions as a function of source lethargy. The variation of the reflection fraction with source energy is due primarily to variation in the iron total cross section. Reflection increases slowly with energy as the iron cross section increases. The increasing iron cross section leads to an increasing fraction of collisions in the first iron layer and, hence, to increasing reflection. The effect of the large anti-resonance in the iron total cross section at 25 kev (U = 6) is clearly visible in Figure 40. At source energies near 25 kev, the first iron layer is relatively "transparent" to the incident neutrons. For such sources a much larger fraction of the incident neutrons reach the water layers and are thermalized. The probability of being reflected is small

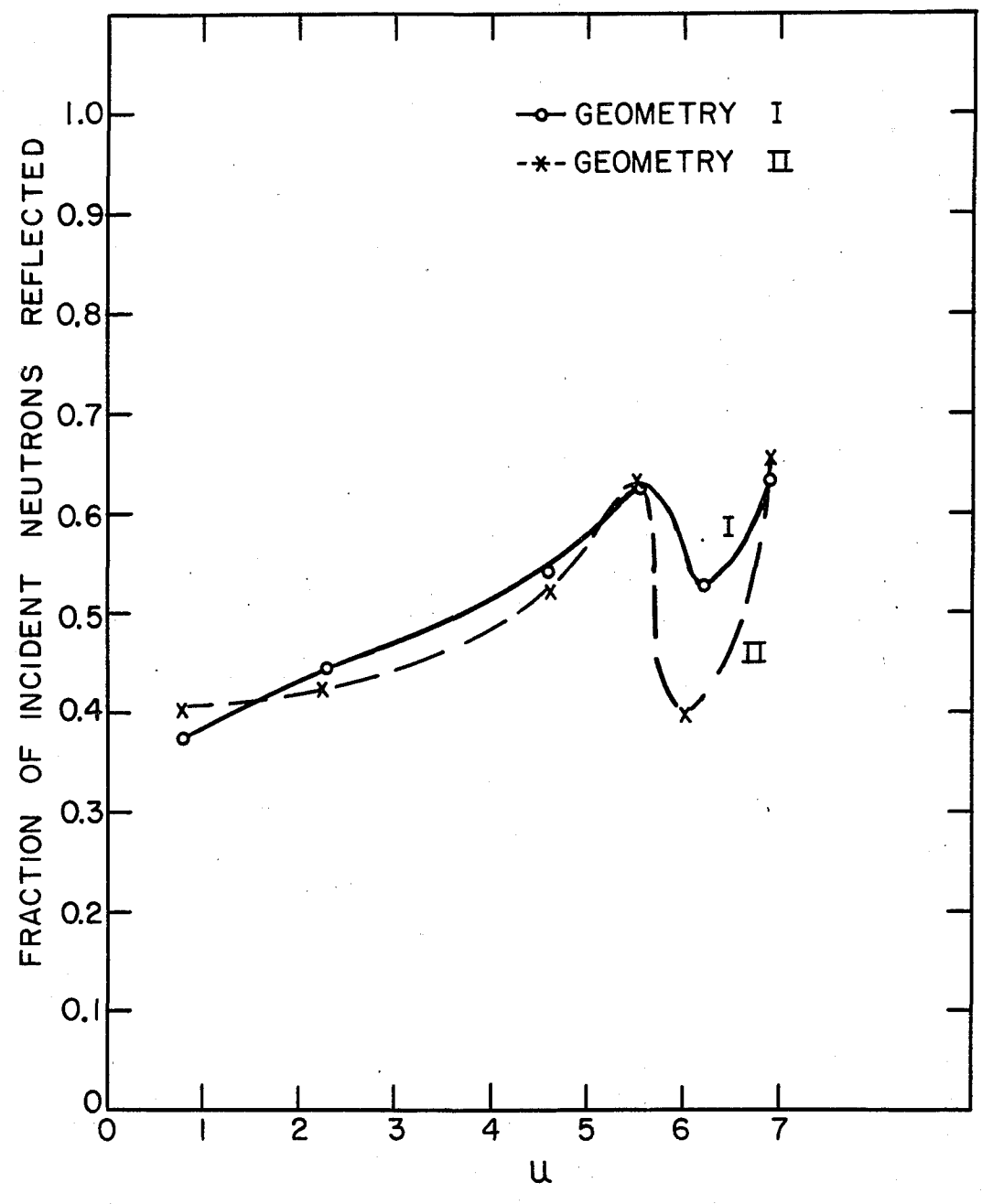

Figure 40. Reflection fractions in the principle runs

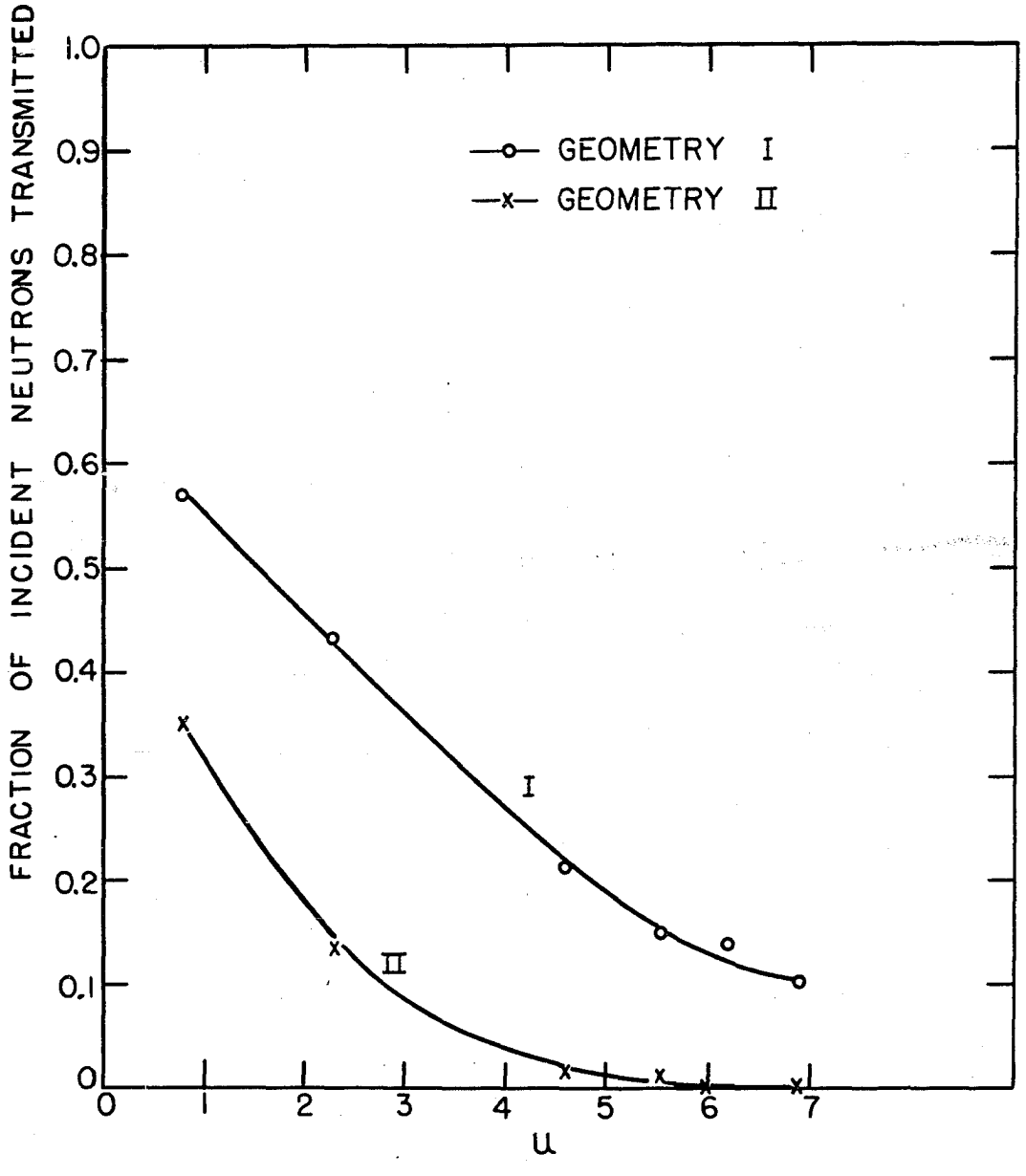

Figure 41. Transmission fractions in the principle runs

for thermal neutrons so that 25 kev sources lead to reduced reflection fractions (and, as discussed in the next section, to increased capture rates). A smaller, opposite effect (increased reflection) is evident at about 0.04 Mev (U = 5.5). This is the result of a positive resonance in the iron total cross section near this energy.

The variation of the transmission fraction in Figure 41 is due to the increasing probability of a neutron's being thermalized in the array as the source energy decreases. The short mean free path of low energy neutrons means that they have much less chance of being transmitted than do higher energy neutrons. The difference between the two curves in Figure 41 is due primarily to the difference in the thicknesses of the water layers in the two geometries.

Tables 8 to 11 give the energy spectra of the transmitted and reflected neutrons. In general, the reflection spectra exhibit a large peak representing the majority of the reflected neutrons at, or just below, the source energy, another much smaller peak at thermal energies, and a small broad minimum between the two peaks. An exception to this occurs for sources of energy near the 25 kev iron anti-resonance. For such sources a large fraction of the reflected neutrons have suffered collisions in the first water layer. The large energy reductions accompanying these water collisions cause the reflected neutron energies to be spread more

Table 8. Energy spectrum of reflected neutrons--geometry I

	Fraction of reflected neutrons in ΔE Source energy E_o(Mev)					
ΔE(Mev)	4.5	1.0	0.1	0.04	0.02	0.01
$0-10^{-6}$	0.029	0.071	0.107	0.087	0.157	0.127
$10^{-6}-10^{-5}$	0.015	0.035	0.060	0.050	0.077	0.052
$10^{-5}-10^{-4}$	0.011	0.054	0.060	0.060	0.103	0.089
$10^{-4}-10^{-3}$	0.020	0.046	0.072	0.101	0.131	0.069
$10^{-3}-10^{-2}$	0.021	0.087	0.100	0.086	0.127	0.664
$10^{-2}-10^{-1}$	0.049	0.134	0.602	0.617	0.406	--
$10^{-1}-1$	0.248	0.573	--	--	--	--
1-10	0.606	--	--	--	--	--

Table 9. Energy spectrum of reflected neutrons--geometry II

	Fraction of reflected neutrons in ΔE Source energy (Mev)					
ΔE(Mev)	4.5	1.0	0.1	0.04	0.025	0.01
$0-10^{-6}$	0.036	0.065	0.064	0.067	0.212	0.065
$10^{-6}-10^{-5}$	0.017	0.028	0.032	0.048	0.076	0.027
$10^{-5}-10^{-4}$	0.010	0.046	0.050	0.030	0.084	0.023
$10^{-4}-10^{-3}$	0.011	0.058	0.070	0.031	0.130	0.034
$10^{-3}-10^{-2}$	0.046	0.047	0.080	0.073	0.193	0.851
$10^{-2}-10^{-1}$	0.035	0.083	0.701	0.750	0.306	--
$10^{-1}-1$	0.208	0.676	--	--	--	--
1-10	0.638	--	--	--	--	--

Table 10. Energy spectrum of transmitted neutrons--geometry I

	Fraction of transmitted neutrons in ΔE Source energy (Mev)					
ΔE (Mev)	4.5	1.0	0.1	0.04	0.02	0.01
$0-10^{-6}$	0.031	0.085	0.262	Too few for significance		
$10^{-6}-10^{-5}$	0.012	0.034	0.106			
$10^{-5}-10^{-4}$	0.013	0.039	0.126			
$10^{-4}-10^{-3}$	0.018	0.056	0.159			
$10^{-3}-10^{-2}$	0.024	0.098	0.178			
$10^{-2}-10^{-1}$	0.038	0.115	0.168			
$10^{-1}-1$	0.139	0.572	--			
1-10	0.726	--	--			

Table 11. Energy spectrum of transmitted neutrons--geometry II

	Fraction of transmitted neutrons in ΔE Source energy (Mev)					
ΔE (Mev)	4.5	1.0	0.1	0.04	0.025	0.01
$0-10^{-6}$	0.099	Too few for significance				
$10^{-6}-10^{-5}$	0.016					
$10^{-5}-10^{-4}$	0.040					
$10^{-4}-10^{-3}$	0.028					
$10^{-3}-10^{-2}$	0.040					
$10^{-2}-10^{-1}$	0.049					
$10^{-1}-1$	0.174					
1-10	0.552					

evenly over the energy range between the source energy and thermal energies. The data for the transmitted neutron energy spectra were not statistically significant for most of the problems. The available data indicate, as would be expected, that the transmission energy spectra also exhibit a large peak near the source energy and a smaller peak at thermal energies.

Tables 12 to 15 give the angular spectra of the reflected and transmitted neutrons in the main runs. An interesting feature of the reflection spectra is that they show a striking constancy as a function of source energy. Because of the apparent insensitivity of the reflection angular spectra to changes in the source energy, an average reflection angular spectrum was calculated by averaging, over the six source energies in each geometry, the fraction of reflected neutrons in each cosine interval. The resulting reflection angular spectrum is compared in the tables with the cosine angular distribution. The reflection angular spectrum in these runs approximates a cosine distribution very closely.

The transmission angular spectra shown in the tables, are again, very poor statistically. The transmission angular spectra appear to be somewhat more peaked in the forward direction than the reflection angular spectra. This is probably due to the higher probability of transmission for those source neutrons that are approximately normally incident and to a significant forward peaking in the iron differential scattering cross section at higher energies.

Table 12. Angular spectrum of reflected neutrons--geometry I

	Fraction of reflected neutrons with cos θ_{i-1} in Δ cos θ							
	Source energy (Mev)							
$-\Delta$ cos (θ)	4.5	1.0	0.1	0.04	0.02	0.01	Average for all sources	Cosine distribution
0-0.1	0.017	0.013	0.014	0.009	0.016	0.014	0.014	0.010
0.1-0.2	0.060	0.047	0.046	0.042	0.035	0.065	0.049	0.030
0.2-0.3	0.079	0.063	0.060	0.054	0.050	0.061	0.061	0.050
0.3-0.4	0.097	0.096	0.089	0.079	0.085	0.071	0.086	0.070
0.4-0.5	0.113	0.091	0.112	0.105	0.074	0.067	0.094	0.090
0.5-0.6	0.110	0.103	0.133	0.120	0.090	0.114	0.112	0.110
0.6-0.7	0.115	0.132	0.106	0.121	0.157	0.126	0.126	0.130
0.7-0.8	0.137	0.131	0.124	0.143	0.128	0.130	0.132	0.150
0.8-0.9	0.134	0.139	0.148	0.165	0.193	0.151	0.155	0.170
0.9-1.0	0.137	0.184	0.170	0.162	0.171	0.201	0.171	0.190

Table 13. Angular spectrum of reflected neutrons--geometry II

	Fraction of reflected neutrons with cos θ_{i-1} in Δ cos θ Source energy (Mev)							
$-\Delta$ cos (θ)	4.5	1.0	0.1	0.04	0.025	0.01	Average for all sources	Cosine distribution
0-0.1	0.007	0.012	0.019	0.010	0.015	0.012	0.013	0.010
0.1-0.2	0.028	0.071	0.030	0.031	0.054	0.038	0.042	0.030
0.2-0.3	0.051	0.030	0.046	0.065	0.050	0.045	0.048	0.050
0.3-0.4	0.071	0.096	0.099	0.064	0.076	0.075	0.080	0.070
0.4-0.5	0.084	0.103	0.137	0.088	0.064	0.090	0.094	0.090
0.5-0.6	0.112	0.088	0.100	0.077	0.144	0.127	0.108	0.110
0.6-0.7	0.136	0.094	0.092	0.116	0.075	0.127	0.107	0.130
0.7-0.8	0.137	0.155	0.141	0.169	0.141	0.146	0.148	0.150
0.8-0.9	0.164	0.178	0.162	0.184	0.185	0.154	0.171	0.170
0.9-1.0	0.212	0.177	0.172	0.195	0.197	0.187	0.190	0.190

Table 14. Angular spectrum of transmitted neutrons--geometry I

	Fraction of transmitted neutrons with cos θ_{i-1} in Δ cos θ							
	Source energy (Mev)							
Δ cos θ	4.5	1.0	0.1	0.04	0.02	0.01	Average for all sources	Cosine distribution
0 - 0.1	0.006	0.003	0.004	Too few for			0.004	0.010
0.1-0.2	0.015	0.015	0.019	significance			0.016	0.030
0.2-0.3	0.022	0.018	0.010				0.017	0.050
0.3-0.4	0.052	0.036	0.077				0.055	0.070
0.4-0.5	0.075	0.069	0.085				0.076	0.090
0.5-0.6	0.086	0.099	0.100				0.095	0.110
0.6-0.7	0.135	0.143	0.163				0.147	0.130
0.7-0.8	0.166	0.161	0.141				0.156	0.150
0.8-0.9	0.194	0.209	0.224				0.209	0.170
0.9-1.0	0.248	0.245	0.174				0.222	0.190

Table 15. Angular spectrum of transmitted neutrons--geometry II

	Fraction of transmitted neutrons with cos θ_{i-1} in Δ cos θ Source energy (Mev)							
Δ cos θ	4.5	1.0	0.1	0.04	0.025	0.01	Average for all sources	Cosine distribution
0-0.1	0.004	Too few for significance						0.010
0.1-0.2	0.028							0.030
0.2-0.3	0.014							0.050
0.3-0.4	0.053							0.070
0.4-0.5	0.065							0.090
0.5-0.6	0.122							0.110
0.6-0.7	0.114							0.130
0.7-0.8	0.136							0.150
0.8-0.9	0.206							0.170
0.9-1.0	0.259							0.190

DISCUSSION

Physical Features of the Capture Distributions

The attenuation of neutrons in an array of iron and water slabs is characterized by the following physical properties:

1. At neutron energies above the thermal range, the energy changes accompanying neutron-iron and neutron-oxygen elastic collisions are relatively small (maximum of 5% for iron and 25% for oxygen).

2. At all neutron energies, the average energy change in neutron-proton collisions is large.

3. Iron inelastic scattering comprises about 40% of all iron collisions at 5 Mev and decreases with decreasing energy to a negligible rate at 0.85 Mev.

4. The neutron capture rate in iron is small at higher neutron energies and increases with decreasing neutron energy to a rate equal to 30 to 90% of all iron collisions at thermal neutron energies.

5. The capture cross section for water is much smaller than that of iron at all neutron energies.

6. The iron scattering cross section (excluding resonances) increases by a factor of about three between 5 Mev and thermal energies.

7. The scattering cross section of water increases from a value approximately equal to that of iron at 5 Mev to approximately six times that of iron at thermal energies.

As a result of these properties, the attenuation and capture of high energy neutrons in an array of iron and water slabs proceeds via three steps:

1. The energy of high energy neutrons (greater than 1 Mev) is reduced to about 1 Mev by inelastic scattering in iron and by neutron-proton collisions in water. Below this region (1 Mev), the cross section of water becomes larger than that of iron so that neutron-proton collisions begin to predominate.

2. The neutrons are then thermalized by elastic collisions with protons in the water.

3. The thermalized neutrons then diffuse to the iron where they are captured.

The position and energy changes of the neutrons in steps 1 and 2 are large, whereas the capture rate in these steps is small. On the other hand, most of the capture occurs in step 3, in which the energy remains relatively constant and the position changes are much smaller than in the first two steps.

On the basis of these known physical characteristics of the attenuation process, one would expect certain qualitative features to be present in the capture distribution curves for the various layers in the array. (Some of these features were outlined in the previous section, but will be repeated for completeness). These features are as follows:

1. First iron layer. The capture curve in this layer

should be low at the left face of the layer because of the large leakage rate of neutrons through this face (reflection). The curve then should increase rapidly with distance into the slab, reaching a maximum at the right face. This increase is the result of the capture of neutrons that are thermalized in the first water layer and diffuse back into the first iron layer.

2. First water layer. The capture curve should be lower at the left face of this layer than at the right face because of greater thermal neutron leakage through the left face (via the first iron layer) than through the right face (via the last four layers of the array). Between these two faces the capture curve should exhibit a maximum. This maximum is the result of the larger thermal neutron capture cross section in iron as compared to that of water. The iron layers on either side of the water layer act as thermal neutron "sinks" which deplete the thermal neutron population in the water near these iron surfaces. The water capture rates should be smaller than the capture rates in adjacent iron layers.

3. Second iron layer. The water layers adjacent to this iron layer act as "sources" of thermal neutrons. These thermalized neutrons diffuse into the iron and are rapidly absorbed. Consequently, peaks should occur in the iron capture curve at each surface of the layer. The probability that a thermal neutron will diffuse out of the assembly is approxi-

mately the same at both faces of the second iron layer, and, thus, the thermal neutron flux and the capture rate would be expected to be approximately the same at both faces of this layer. If a difference exists, the capture rate at the left face should be larger than that at the right face, because of a general decrease in the neutron population from left to right through the array as the source neutrons are captured. This attenuation of the neutron flux by the slabs and, consequently, the difference just described, should increase with increasing dimensions of the array and with decreasing source energy. Finally, the height of the capture curve at the left face of the second iron layer should be greater than that at the right face of the first iron layer. Approximately the same number of thermal neutrons should diffuse to each of these two surfaces from the first water layer, but the larger leakage (reflection) from the first iron layer should decrease the thermal neutron population in that layer as compared to the population in the second iron layer.

4. Second water layer. The capture curve in this layer should be similar to that in the first water layer with the exception that the capture rate at the right surface of the second water layer may be somewhat less than that at the left face of this layer. Attenuation in the first three layers of the array should cause the capture rate in the second water layer to be somewhat lower than that in the first water layer.

Both of these effects should be larger for larger geometries and for smaller source energies.

5. Third iron layer. The shape of the capture curve in this layer should be similar to that in the second iron layer. The capture rate at the left face of the third iron layer should be smaller than that at the right face of the second iron layer. This is due to attenuation of the thermal neutron flux by the first four layers. In addition, the capture rate at the right face of the third iron layer should be smaller than that at the left face because of attenuation and also because of leakage of the thermal neutrons through the third water layer (transmission). These features should be more pronounced for larger geometries and for smaller source energies. A minimum still should exist in the curve in the third iron layer because of the capture of thermal neutrons that diffuse back into the iron from the second and third water layers. The peak at the right face of the third iron layer should decrease more rapidly with increasing slab dimensions and decreasing source energy than the peak at the left face. Again, this is an attenuation effect.

6. Third water layer. A shallow maximum near the third iron layer would be expected in the capture curve in the third water layer. This maximum is caused by depletion of the thermal neutron population at the left face of the third water layer by diffusion into the adjacent iron "sink", and

depletion of the population at the right face of the third water layer by leakage (transmission) through the right face. This leakage should normally cause a larger decrease in the curve near the right face of the third water layer than diffusion into the iron causes at the left face. The maximum in the third water layer should become less pronounced with increasing slab size and decreasing source energy as the effect of attenuation through the third water layer becomes larger than the effect of the iron "sink".

These qualitative features were evident in the majority of the capture curves as fitted to the original data. (These curves are the solid curves in Figures 24 to 27). In several instances, however, the capture curves were not compatible with the qualitative expectations. For example, the capture rate in the third iron layer of geometry I exhibits a minimum, as expected, for source energies of 1.0, 0.04, and 0.02 Mev, but no minimum for source energies of 4.5, 0.1, and 0.01 Mev. There is no physical explanation for this behavior. The logical conclusion is that statistical fluctuations obscured the peak at the right surface of the third iron layer for certain problems. Examination of the solid curves in Figures 24 to 27 will show that exceptions to most of the expected qualitative features are present.

As discussed in previous sections, the original capture curves were adjusted in three ways: The data were smoothed

as a function of source lethargy, the capture rate in the iron at each iron-water interface was set to 9.74 times the capture rate in the water at the interface, and the parameters of the capture curves fitted to these adjusted points were smoothed as a function of source lethargy. (This last adjustment was relatively small compared to the first two). Capture curves calculated from these final smoothed parameters are shown as the dashed curves in Figures 24 to 27.

These final capture curves are, qualitatively, much superior to the original capture curves. The final curves exhibit the expected qualitative features with few exceptions. Those exceptions that do occur are not large and are of a relatively unimportant type. (For example, the capture rate at the left face of the third iron layer in geometry I is somewhat larger for some source energies than the capture rate at the right face of the second iron layer). It is interesting to note that the larger differences between the original curves and the adjusted curves occur in those instances in which the qualitative inconsistencies were most pronounced in the original curves.

These last statements must be qualified to some extent for sources of energies near the 25 kev resonance in the iron total cross section. For such sources, a resonance effect is present that is smoothed out in the data processing. This is discussed in the following paragraphs.

Resonance Effects

The variations of the capture probabilities as a function of source lethargy at constant x, as shown in Figures 22 and 23, exhibit rather large fluctuations for source energies of 0.04 Mev (U = 5.5) and 0.02 or 0.025 Mev (U = 6.0). This is particularly evident near slab surfaces. The 0.04 Mev points appear to be unusually low, and the 0.02 and 0.025 Mev points appear to be unusually high. This behavior is the result of resonances that exist in the iron total cross section. A positive resonance exists at about 0.03 Mev and a very large anti-resonance (minimum) exists in the cross section curve at 0.025 Mev. These resonances lead to either increased (for a positive resonance) or decreased (for an anti-resonance) reflection rates from the first iron slab and corresponding decreases or increases in the number of source neutrons that reach the water layers and that are subsequently thermalized and captured in the array. (This effect was described in the previous section).

In order to resolve adequately the effects of these cross section resonances upon the behavior of the capture rates as a function of source energy, it would be necessary to run a number of additional problems with source energies in the range 0.05 to 0.01 Mev. Such an examination was not within the scope of the present study. In lieu of this examination, it was decided to smooth the data as a function of source

lethargy, as described earlier, with, as a result, underestimations of the capture rates for 0.025 Mev sources and overestimations of the capture rates for 0.04 Mev sources.

In most practical problems, the fraction of source neutrons that will have energies near these resonances will be small, and the errors resulting from this lack of resolution of the resonance effects will not be serious. The existence of this deficiency certainly should be kept in mind, however, in using the results of this work.

Sample Problem

The following example will illustrate one manner in which the data and correlations presented in this paper might be employed.

Consider the problem of determining the capture distribution in a reactor thermal shield assembly that approximates geometry II from neutrons leaking out of a reactor core and impinging upon the thermal shield array. Normally, the angular spectrum of these neutrons will approximate a cosine or isotropic distribution, and the results presented in this paper should apply very well. Assume that the neutrons impinging upon the array have k different energies, or, that the energy spectrum of the neutrons can be broken up into k different effective energy groups. Assume further that the source strength, i.e., the neutron current into the array of

neutrons in energy group, i, is given by S_i (neutrons/in^{2}sec).

The probability of a neutron-neutron collision is extremely small so that neutrons in one energy group do not affect the results from neutrons in other energy groups. Therefore, the k energy groups can be treated as k different problems and the final results can be obtained simply by summing the contributions from the k groups.

For illustration, assume that one of the source energy groups has an effective energy of 2 Mev and a source strength of 10^5 neutrons/in^{2}sec. (The treatment of the other groups will proceed in an identical fashion.) From Figures 34 to 39 (or from the equations for the curves in these figures) we obtain the parameters for the capture distribution curves for a 2 Mev (U = 1.609) source:

First iron layer: $\alpha = 0.0279$, $\beta = 1.987$

First water layer: $A = 0.0373$, $B = 0.0920$, $C = -0.0892$

Second iron layer: $\alpha = 0.0956$, $\beta = 3.222$, $x_o = 0.519$

Second water layer: $A = 0.0239$, $B = 0.0755$, $C = -0.0778$

Third iron layer: $\alpha = 0.0787$, $\beta = 2.178$, $x_o = 0.665$

Third water layer: $A = 0.0105$, $B = 0.0425$, $C = -0.0520$

The corresponding capture probability curves are given by:

First iron layer: $p(x) = 0.0279\ e^{1.987x}$

First water layer: $p(x) = 0.0373+0.0920x - 0.0892x^2$

Second iron layer: $p(x) = 0.0956 \cosh 3.222(x-0.519)$

Second water layer: $p(x) = 0.0239+0.0755x - 0.0778x^2$

Third iron layer: $p(x) = 0.0787 \cosh 2.178(x-0.665)$

Third water layer: $p(x) = 0.0105+0.0425x - 0.0520x^2$

where x = 0 at the left face of each layer and x is in inches. Finally, the capture rates in the various layers from the 2 Mev source group are given by

$$\text{Capture rate} = 10^5\ p(x)\ \text{captures/in}^3\text{sec}$$

where the p(x) are given above. (Note that the origin of each capture curve can be translated to a common point by substituting $x' - x_d$ for x in each equation, where x' is the new position variable and x_d is the displacement of the left face of each slab in the ' coordinate system.)

These equations give the neutron capture rates throughout the thermal shield array. The subsequent determination of the heating that results from the capture gamma-rays is a major problem and one that is not solved easily; however, such problems have received considerable attention in the field of nuclear reactor shielding and many theoretical and empirical approaches have been used with varying degrees of success. A discussion of the problems involved and of some of the commonly used mathematical techniques for such gamma-ray shielding problems may be found in reference (25).

An adequate discussion of the problem of determining the heating rates from distributed neutron capture gamma-ray sources in multiregion configurations would be quite lengthy and is not appropriate here. It should be pointed out, however, that the specification of the capture distributions, i.e., the distribution of capture gamma-ray sources, in terms of a sum of exponential functions, or as a low order polynomial, is convenient for gamma-ray shielding calculations. Such functional forms for the gamma-ray source distributions often lead to closed solutions in terms of tabulated integrals for such shielding problems (25). This was the reason for the choice of the functional forms for the capture distribution curves that were used in this study.

CONCLUSIONS AND RECOMMENDATIONS

Conclusions

1. The problem of determining the neutron capture distribution in an array of iron and water slabs from neutrons impinging upon one face of the array was successfully attacked by means of Monte Carlo calculations with an IBM-650 digital computer.

2. Correlations of the parameters for fitted capture distribution curves were obtained as a function of source energy for two different geometries. This was done for cosine sources of energies between 0.01 Mev and 4.5 Mev.

3. The Monte Carlo results exhibited predictable qualitative characteristics to a very satisfactory degree. All of the features that would be expected in the capture curves, on the basis of physical considerations, were present in the final capture curves obtained in this study.

4. Large resonances in the iron total cross section affected the capture distributions in the array. Streaming of neutrons through the iron layers and into the water layers occurred for sources of energies near the large anti-resonance in the iron total cross section at 25 kev. This caused an increase in the neutron thermalization rate as compared to that for sources of other energies. A corresponding increase in the capture rate in the array and decrease in the reflection rate resulted.

5. Reflection and transmission fractions were obtained as a function of source energy for the two geometries that were examined. The effect of the 25 kev anti-resonance in the iron total cross section was clearly evident in these reflection data.

6. The angular distribution of reflected neutrons very closely approximated a cosine distribution, while the angular distribution of transmitted neutrons was somewhat more peaked in the forward direction.

7. The most important variables in these problems were the dimensions of the layers and the energy of the source neutrons.

8. The capture distributions appeared to be rather insensitive to changes in the source angular spectrum.

9. Calculated capture rates at certain points, particularly at surface points in interior iron layers, were very sensitive to statistical fluctuations in the Monte Carlo data. Known physical characteristics of the attenuation and capture processes were used to improve the Monte Carlo estimates. All such information should be used wherever possible to improve the Monte Carlo estimates. (It should be remembered that, since the statistical uncertainty decreases inversely as the square root of the number of histories, increasing the statistical accuracy of the data by increasing the number of histories is very inefficient.)

10. A modification of a technique due to J. R. Triplett et al. (14a) was used to treat collisions in the thermal energy range. This routine was checked against theoretically predictable and experimental answers for water with excellent results.

11. The rigorous determination of the statistical uncertainty of the final capture curves and correlations in this study was not practical; however, upper limit estimates were obtained. These upper limit estimates were small enough so that the data obtained are considered to be meaningful and useful.

12. Variance reducing techniques and program optimization are essential in Monte Carlo calculations with a machine such as the IBM-650. A large percentage of the work in the present study was expended in attempting to reduce the running times for the problems and the variances of the results.

13. Use of an IBM-650 computer for calculations such as these is practical, but, perhaps, only marginally so. Improvement of the program and the techniques used in this study would increase the versatility of the IBM-650 in such calculations; however, this effort might possibly be expended more profitably with a larger and faster machine should such be available.

14. The Monte Carlo method offers a versatile and, it is felt, an important tool with which to attack neutron transport

problems. Monte Carlo techniques and methods are becoming more standardized so that the novice can apply Monte Carlo effectively to a wide variety of problems. As experience in the field is accumulated and disseminated, the Monte Carlo method should become a calculational tool of increasing value. (This statement also applies to many problems other than those in neutron transport).

Recommendations

1. The machine used in this study had a 2000 word drum memory. This is to be replaced soon by a 4000 word drum. The program should be re-written for this new drum and optimized more efficiently. The source energy limitation also could be relaxed with a larger drum, and other refinements (e.g., more detailed treatment of iron inelastic scattering), which were impossible with the 2000 word memory, could be added.

2. Improvements in the Monte Carlo techniques should be sought continually in order to decrease the variances of the results obtained in a given amount of computing time.

3. Some means of testing the high energy portion of the program should be found. Work that may be pertinent is underway at present, and more is planned for the future, at the Iowa State University reactor. These studies might be used to check the reliability of answers produced by the Monte Carlo program.

4. The effect of geometry changes upon the capture dis-

tributions should be studied in detail. Some means should be found, if possible, of correlating this information in a useful manner. This task will probably be difficult, but the systemization of geometry effects must be accomplished before the present data will be of maximum usefulness.

5. Better resolution of the resonance effects in the capture distributions as a function of source energy should be obtained. The range of source energies between 0.01 Mev and 0.05 Mev should be examined in more detail.

6. The effect of temperature should be examined. It would be expected that the capture rates would not be sensitive to temperature changes; however, this should be verified.

7. The effect of errors in the cross section data used in this study should be determined. Examination of the effect of changing the energy variation of the capture cross sections would be particularly interesting. In addition, the total cross section data are rather uncertain in the thermal energy range. The effect of errors in these data should be studied. Finally, effects arising from smoothing the many small resonances in the iron cross section data as was done in this work should be studied.

8. The effect upon the capture distributions of uncertainties in the iron inelastic scattering physical model and in the iron inelastic scattering cross section and gamma emission probability data should be examined. These uncer-

tainties will be more important if the upper limit of the source energy is increased.

9. Quantitative studies should be made of the effect upon the statistical uncertainties of variations in the Monte Carlo techniques. For example, optimum values should be sought for the termination probability and the value of W_R in the Russian Roulette routine. In the present study, a termination probability of 0.5 and values of W_R between 0.1 and 0.3 appeared to give the most satisfactory results. However, no quantitative study of these effects was made. In addition, the effect upon the variances of such techniques as the uniform first collision weighting routine should be examined. (These statements also apply to new variance reducing techniques that might be added to the program).

10. Methods of determining the statistical reliability of the curves and correlations as presented in this work should be studied. The amount of improvement of the variances of the final answers as compared to the variances of the original data points should be established if possible.

ACKNOWLEDGEMENTS

The author would like to thank the people whose advice and assistance were sought during this study. Particularly, the contributions of the following are gratefully acknowledged: Dr. Herman O. Hartley of the Iowa State University Statistical Laboratory whose counsel was extended throughout the course of this study, Dr. Raymond W. Fahien of the Iowa State University Chemical Engineering Department whose critical comments and continual support are sincerely appreciated, Mr. Howard Jesperson of the Iowa State University Computing Laboratory whose assistance on both statistical and computing questions was sought on numerous occasions, and, finally, a special thanks is extended to Mr. Russel Altenberger of the Iowa State University Computing Laboratory who assisted the author continually in the use of the Computing Laboratory facilities, and whose assistance was invaluable in the programming of the IBM-650 programs written for this study.

REFERENCES CITED

1. Zerby, C. D. Transmission of obliquely incident gamma-radiation through stratified slab barriers. Volumes I and II. U. S. Atomic Energy Commission Report ORNL-2224 [Oak Ridge National Lab., Tenn.]. December, 1956.

2. Obenshain, F., Eddy, A. and Kuehn, H. Polyphemus a Monte Carlo study of neutron penetrations through finite water slabs. U. S. Atomic Energy Commission Report WAPD-TM-54 [Westinghouse Electric Corp. Bettis Plant, Pittsburgh]. January, 1957.

3. Cashwell, E. D., Everett, C. J. and Rechard, O. W. Practical manual on the Monte Carlo method for random walk problems. U. S. Atomic Energy Commission Report LA-2120 [Los Alamos Scientific Lab., N. Mex.]. December, 1957.

4. Monte Carlo method. Proceedings of a symposium held June 29, 30, and July 1, 1949, in Los Angeles, California, under the sponsorship of the RAND Corporation, and the National Bureau of Standards, with the cooperation of the Oak Ridge National Laboratory. U. S. Department of Commerce, National Bureau of Standards Applied Mathematics Series. No. 12. June, 1951.

5. Meyer, Herbert A., ed. Symposium on Monte Carlo methods. Held at the University of Florida, conducted by the Statistical Laboratory, sponsored by Wright Air Development Center of the Air Research and Development Command, March 16 and 17, 1954. New York, N. Y. John Wiley and Sons, Inc. [c1956].

6. Kahn, Herman. Applications of Monte Carlo. U. S. Atomic Energy Commission Report AECU-3259 [Technical Information Service Extension, AEC]. April, 1956.

7. Mayne, A. J. Monte Carlo methods for solving neutron problems. U. S. Atomic Energy Commission Report AWRE-0-18/55 [Gt. Brit. Atomic Weapons Research Establishment, Aldermaston, Berks, England]. July, 1955.

8. Weinberg, Alvin M. and Wigner, Eugene P. The physical theory of neutron chain reactors. Chicago, Illinois. The University of Chicago Press. [c1958].

9. Glasstone, Samuel and Edlund, Milton C. The elements of nuclear reactor theory. Toronto, Canada. D. Van Nostrand Company, Inc. [c1952].

10. Mood, Alexander McFarlane. Introduction to the theory of statistics. New York, N. Y. McGraw-Hill Book Co., Inc. 1950.

11. Hughes, Donald J. and Carter, Robert S. Neutron cross sections. Angular distributions. U. S. Atomic Energy Commission Report BNL-400 [Brookhaven National Lab., Upton, N. Y.]. June, 1956.

12. Halliday, David. Introductory nuclear physics. 2d ed. New York, N. Y. John Wiley and Sons, Inc. [c1955].

13. Troubetzkoy, E. S. Fast neutron cross sections of iron, silicon, aluminum, and oxygen. U. S. Atomic Energy Commission Report NDA 2111-3, Vol. C [Nuclear Development Corp. of America, White Plains, N. Y.]. November, 1959.

14a. Triplett, J. R., Leshan, E. J., Burr, F. R., Temme, M. and Thompson, G. T. RBU: a combined Monte Carlo reactor-burnup program for the IBM 709. Informal U. S. Atomic Energy Commission Research and Development report ATL-A-101 [Advanced Technology Labs. Div. of American-Standard, Mountain View, Calif.]. September, 1959.

14b. RAND Corporation. Million random digits. In RAND Corporation. Cumulative index of card tables. Table 0017. Santa Monica, Calif. Author. 1956.

15. Hughes, Donald J. and Schwartz, Robert B. Neutron cross sections. U. S. Atomic Energy Commission Report BNL-325 [Brookhaven National Lab., Upton, N. Y.]. 2d ed. July, 1958.

16. Gurney, Ronald W. The scattering of slow neutrons in polycrystalline media. Physical Review. 88: 466-467. 1952.

17. Storm, M. L., Hurwitz, H., Jr. and Roe, G. M. Gamma-ray absorption distributions for plane, spherical, and cylindrical geometrics. U. S. Atomic Energy Commission Report KAPL-783 [Knolls Atomic Power Lab., Schenectady, N. Y.]. July, 1952.

18. Kaplan, Irving. Nuclear physics. Cambridge, Mass. Addison-Wesley Publishing Co., Inc. [c1955].

19. Amster, Harvey J. The Wigner-Wilkins calculated thermal neutron spectra compared with measurements in a water moderator. Nuclear Science and Engineering. 2: 394-404. 1957.

20. Brown, H. Dean. Neutron energy spectra in water. U. S. Atomic Energy Commission Report DP-64 [Du Pont de Nemours (E. I.) and Co., Wilmington, Del.]. February, 1956.

21. Nelkin, M. S. and Cohen, E. R. Recent work in neutron thermalization [Official paper A/Conf.15/P/1839.] Second United Nations International Conference on the Peaceful Uses of Atomic Energy, Geneva, 1958. Proceedings. 16: 270-278. 1958.

22. Triplett, J. R. Data from the RBU Monte Carlo program. (Manuscript). U. S. Atomic Energy Commission, Ames Lab. Document Library. Research Notebook No. WWC-5. 1960.

23. Drozdov, S. I., Zaretsky, D. F., Kudrin, L. P., Sedelnikov, T. Kh. On the formation of a thermal-neutron spectrum. [Official paper A/Conf.15/P/2033.] Second United Nations International Conference on the Peaceful Uses of Atomic Energy, Geneva, 1958. Proceedings. 16: 223-232. 1958.

24. Murray, Raymond L. Nuclear reactor physics. Englewood Cliffs, N. J. Prentice-Hall, Inc. [c1957].

25. Rockwell, Theodore, III, ed. Reactor shielding design manual. New York, N. Y. McGraw-Hill Book Co., Inc. 1956.

26. RAND Corporation. One thousand deviates from N(0, 1). In RAND Corporation. Cumulative index of card tables. Table 0019. Santa Monica, Calif. Author. 1956.

27. Massey, Frank J., Jr. The Kolmogorov-Smirnov test for goodness of fit. Journal of the American Statistical Association. 46, No. 253: 68-78. March, 1951.

28. Lustig, H. Differential elastic neutron scattering cross section of oxygen. U. S. Atomic Energy Commission Report NDA 211-3, Vol. A [Nuclear Development Corp. of America, White Plains, N. Y.]. November, 1959.

29. Sullivan, William H. Trilinear chart of nuclides. 2d ed. Sponsored by the Oak Ridge National Laboratory and the Technical Information Service of the U. S. Atomic Energy Commission. Washington, D. C., U. S. Government Printing Office. January, 1957.

APPENDIX A

Distance between Collisions

The probability that a neutron with energy E will suffer an interaction while traveling through a homogeneous material[1] is known to be a constant per unit distance traveled. This constant depends only upon the energy of the neutron and upon the particular medium being traversed. The constant is the macroscopic total cross section and usually is designated by Σ_T.

If a beam of N uncollided neutrons with energy E impinges normally upon a small thickness, dy, of a material, then, on the average, a fraction, $\Sigma_T(E)\,dy$, of these will be removed from the incident beam as it passes through dy. Thus,

$$\frac{dN}{N} = \Sigma_T(E)\,dy$$

The solution of this equation gives the well-known exponential attenuation law for the fraction of uncollided neutrons at a distance y into a layer of material from an initial beam of N_o neutrons impinging normally upon that layer at y = 0.

$$\frac{N}{N_o} = e^{-\Sigma_T(E)\,y}$$

The probability that a neutron will travel uncollided

---

[1] The following statements apply equally well to a material with uniform inhomogeneities of a size that is small compared to the mean free path between collisions of the neutrons in the medium.

through a distance y in a material with total cross section, $\Sigma_T(E)$, and then collide in an infinitesimal thickness dy is, therefore,

$$p(y)\,dy = e^{-\Sigma_T(E)\,y}\,\Sigma_T(E)\,dy$$

The function, p(y), is the probability density function describing the position, y, for the first collision of a neutron starting at y = 0 and traveling along the direction y in a medium with total cross section $\Sigma_T(E)$. (Note that $\int_0^\infty p(y)\,dy = 1$ as required for the probability density function.)

If we measure distance along a direction x with which the direction y makes an angle θ, the probability distribution for the first collision as measured along x is simply

$$p(x)\,dx = \frac{\Sigma_T(E)}{\cos\,\theta}\; e^{-\frac{\Sigma_T(E)\;x}{\cos\,\theta}}\,dx$$

where x is the distance traveled in the direction x from the point of origin of the neutron (x = 0).

Now, consider a neutron with energy E_i traveling at an angle θ_i to the normal direction x of Figure 1 after having undergone an i^{th} collision at x_i. The distance measured along x to the $i + 1^{st}$ collision is distributed as follows:

$$p(\Delta x_{i+1}) = \frac{\Sigma_T(E_i)}{\cos\,\theta_i}\; e^{-\frac{\Sigma_T(E_i)\,\Delta x_{i+1}}{\cos\,\theta_i}} \qquad \text{(A.1)}$$

where Δx_{i+1} is the distance along the direction x between collisions i and i + 1. To specify the position of the $i + 1^{st}$ collision, we must pick a random Δx_{i+1} from the distribution

A.1 and then set

$$x_{i+1} = x_i + \Delta x_{i+1}$$

A common method of selecting a random sample from distribution A.1 is to use the "Golden Rule" described earlier. The resulting equation specifies Δx_{i+1} as

$$\Delta x_{i+1} = - \frac{\cos \theta_i \ln R}{\Sigma_T(E_i)}$$

where R is a random number selected from the interval (0, 1). The calculation of the necessary hundreds of thousands of logarithms for this study using this method would require very large amounts of computing time on the IBM-650. The following alternative method suggested by Dr. H. O. Hartley of the Iowa State University Statistical Laboratory was used.

If k random samples, y_i, are picked from k independent normal distributions with means μ_i and variances σ_i^2, the variate

$$u = \sum_{i=1}^{k} \left(\frac{y_i - \mu_i}{\sigma_i} \right)^2$$

has a chi-squared distribution with k degrees of freedom (10, p. 199),

$$p(u) = \frac{1}{(k/2 - 1)!} \frac{1}{2^{k/2}} u^{(k/2) - 1} e^{-\frac{1}{2}u} \quad (u > 0)$$

Now, take k = 2 and let the original distributions be N(0, 1); i.e., normal with means 0 and variances 1. We get

$$u = (y_1 + y_2)^2$$

$$p(u) = \tfrac{1}{2}e^{-\frac{1}{2}u} \quad (u > 0) \tag{A.2}$$

Let

$$Y = \tfrac{1}{2}u$$

$$dY = \tfrac{1}{2}du$$

The probability distribution function for Y is thus

$$p(Y) = e^{-Y} \quad (Y > 0) \tag{A.3}$$

i.e., Y is exponentially distributed.

To pick a random sample, Y_i, from an exponential distribution we pick two random samples, y_1 and y_2, from N(0, 1) and set

$$Y_i = \tfrac{1}{2}(y_1 + y_2) = \tfrac{1}{2}u_i$$

Y_i will then be a random sample from the distribution A.3.

A table of 300,000 such exponential deviates was calculated with the IBM-650, using a table of random normal deviates, i.e., random samples from N(0, 1), prepared by the RAND Corporation (26). The RAND table contains 100,000 normal deviates (available on 10,000 standard IBM cards) from which 50,000 exponential deviates were calculated using the RAND cards in serial order. The RAND normal deviate cards were then put in random order by sorting on four successive random digits that were punched into each card from a table of random digits also prepared by the RAND Corporation (14b). The normal deviates on each card were then put in random order, as they

entered the IBM-650, by means of control panel wiring and another 50,000 exponential deviates were calculated. This procedure was repeated until a total of 300,000 exponential deviates had been prepared. This table served as a source of random samples, u_i, from the distribution A.2.

The distribution of the exponential deviates in this table was checked by means of the following goodness-of-fit tests. These tests were made for each block of 50,000 exponential deviates.

Chi-squared test

Suppose that a sample of size n is drawn from a population with distribution f(Y). Let the Y axis be divided into k intervals ΔY_i, i = 1 to k, and let n_i be the number of observations falling in the interval ΔY_i. Let the probability of obtaining a sample in ΔY_i be designated by $p_i = \int_{Y_{i-1}}^{Y_i} f(Y')dY'$.

The variate -2 log λ, where $\lambda = n^n \prod_{i=1}^{k} \left(\frac{p_i}{n_i}\right)^{n_i}$, has a chi-squared distribution with k-1 degrees of freedom as n becomes large (10, p. 270).

Thus, if the value of -2 log λ is calculated that corresponds to a given sample and the distribution that is to be tested (the exponential distribution in this instance), a table of cumulative chi-squared distributions can be used to find the probability of obtaining a value of the deviate

$-2 \log \lambda$ that is larger than the one that is calculated, provided that the distribution being tested is the correct distribution for the sample. If this probability is small, then it is likely that the assumed distribution is incorrect.

For example, assume that the probability, $P(-2 \log \lambda' \geq -2 \log \lambda)$, of obtaining a value of $-2 \log \lambda$ larger than the one calculated, is 0.40. This means that one would expect that 40% of all samples of size n from the assumed distribution would have values of $-2 \log \lambda$ larger than that obtained for the sample being considered. Therefore, there is little reason, on the basis of the sample, to believe that the assumed distribution is incorrect. If, on the other hand, $P(-2 \log \lambda' \geq -2 \log \lambda)$ is, say, 0.05, one can conclude that either the sample is a very unusual one or, that the sample is not from the assumed distribution. The assumed distribution would be very suspect in this instance.

The results of the chi-squared goodness-of-fit tests for the six sets of 50,000 exponential deviates are given in Table 16 for $k = 21$.

Table 16. Results of the chi-squared goodness-of-fit tests for the calculated exponential deviates

Deviates	$-2 \log \lambda$	$P(-2 \log \lambda' \geq -2 \log \lambda)$
1-50,000	17.02	0.64
50,000-100,000	17.48	0.63
100,000-150,000	18.60	0.54
150,000-200,000	17.88	0.60
200,000-250,000	16.04	0.70
250,000-300,000	20.40	0.42

Kolmogorov-Smirnov test (27)

The procedure here is to plot on the same graph the cumulative distribution for the distribution to be tested and the observed cumulative distribution of the sample. Curves are then drawn at a distance $d_\alpha(n)$ above and below the assumed distribution, where values of $d_\alpha(n)$ are given as a function of significance level, α, and sample size, n, in reference (27). If the sample cumulative distribution passes outside the band between the two $d_\alpha(n)$ curves, the hypothesis that the sample is from the distribution being tested is rejected.

The value of $d_\alpha(n)$ for a sample size of 50,000 at the 5% level is 0.0061. (If repeated samples of size 50,000 are taken from a distribution, f(y), the sample cumulative distribution would be expected to lie wholly within $\pm$ 0.0061 of the cumulative distribution of f(y) for 95% of the samples). Table 17 shows the maximum deviation of the observed cumulative distribution from the cumulative exponential distribution for the six sets of exponential deviates that were calculated.

Table 17. Results of the Kolmogorov-Smirnov goodness-of-fit test for the calculated exponential deviates

Deviates	Maximum sample deviation	$d_\alpha(n)$ = maximum deviation for 5% significance level
1-50,000	0.0042	0.0061
50,000-100,000	0.0036	0.0061
100,000-150,000	0.0032	0.0061
150,000-200,000	0.0043	0.0061
200,000-250,000	0.0054	0.0061
250,000-300,000	0.0033	0.0061

APPENDIX B

Energy Change in Elastic Scattering Events

Consider an elastic collision between a neutron of mass m and a stationary nucleus of mass M. We make the following definitions:

E_{i-1} = the kinetic energy of the incoming neutron as measured in the laboratory system of coordinates

x = the distance from the neutron to the nucleus before the collision

X = the distance from the center-of-mass of the two particles to the nucleus before the collision

V^* = the magnitude of the neutron's velocity as measured in the center-of-mass system of coordinates

V_{i-1} = the magnitude of the incident neutron's velocity as measured in the laboratory system of coordinates

V_i = the magnitude of the scattered neutron's velocity as measured in the laboratory system of coordinates

V_c = the magnitude of the velocity of the center-of-mass of the two particles as measured in the laboratory system of coordinates

ψ = the scattering angle as seen from the laboratory system of coordinates

ψ^* = the scattering angle as seen from the center-of-mass system of coordinates.

The laboratory system of coordinates is defined as the system in which the nucleus is stationary before the collision.

The center-of-mass system of coordinates is defined by the requirement that the total momentum of the particles as measured in this coordinate system shall be zero.

Since no external forces act upon the two particle system and the masses and total energy are unchanged by the collision, it is easily shown (2) that the velocities of the neutron and the nucleus in the center-of-mass system are always oppositely directed and remain unchanged in magnitude by the collision.

The conditions that prevail before and after the collision in both coordinate systems are shown in Figures 42a and 42b (9, p. 137).

The vector diagram that describes the neutron velocity after the collision is given in Figure 43.

If the center-of-mass coordinate system is chosen so that its origin is at the center-of-mass of the two particles, we can write

$$(m + M)X = mx$$

or

$$X = \frac{mx}{M + m}$$

Now, take the time derivative

$$\dot{X} = \frac{m\dot{x}}{M + m}$$

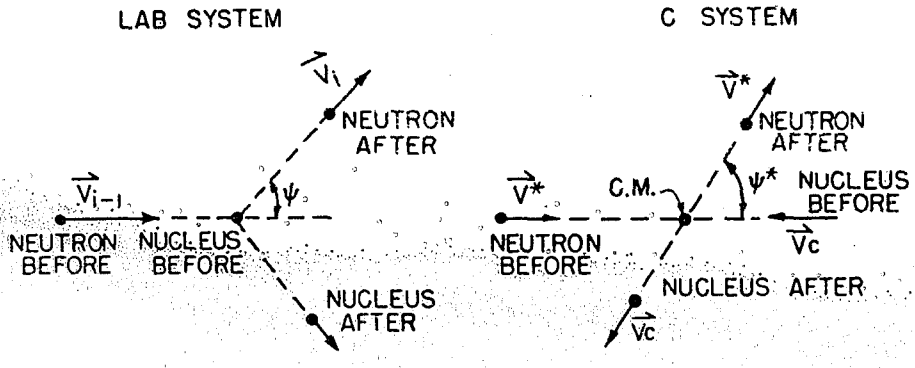

Figure 42a. A neutron-nucleus collision in the laboratory system of coordinates

Figure 42b. A neutron-nucleus collision in the center-of-mass system of coordinates

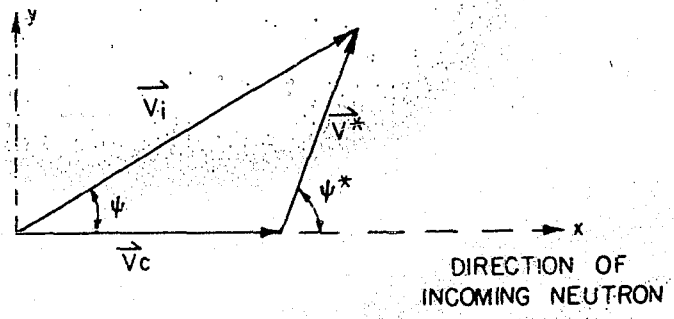

Figure 43. Vector diagram for a neutron-nucleus collision

If the nucleus is stationary in the laboratory system before the collision, the speed of the nucleus as seen from the center-of-mass system before the collision clearly must be the same as the speed of the center-of-mass as seen from the laboratory system. We can thus write

$$V_c = \dot{X} = \frac{m\dot{x}}{M + m} = \frac{m\ V_{i-1}}{M + m}$$

Recalling that the total momentum is zero in the center-of-mass system we have

$$mV^* = MV_c$$

or

$$V^* = \frac{M}{m} V_c = \frac{M\ V_{i-1}}{M + m}$$

We now refer to Figure 43 and equate components along the x-axis,

$$V_i \cos \psi = V^* \cos \psi^* + V_c$$

and, along the y-axis,

$$V_i \sin \psi = V^* \sin \psi^*$$

Squaring and adding these two equations we get

$$V_i^2 = V^{*2} + V_c^2 + 2V^*V_c \cos \psi^*$$

$$= V_{i-1}^2 \left[\left(\frac{M}{M+m} \right)^2 + \left(\frac{m}{M+m} \right)^2 + \frac{2Mm}{(M+m)^2} \cos \psi^* \right]$$

Finally, recalling that the kinetic energy is given by

$$E = \tfrac{1}{2} mV^2$$

we have

$$\frac{E_i}{E_{i-1}} = \frac{V_i^2}{V_{i-1}^2} = \frac{M^2 + m^2 + 2Mm \cos \psi^*}{(M+m)^2}$$

or

$$\frac{E_i}{E_{i-1}} = \frac{1 + a^2 + 2a \cos \psi^*}{(1+a)^2}$$

where $a = M/m$.

This equation gives the change in kinetic energy of a neutron with energy E_{i-1} upon being scattered through an angle ψ^* as measured in the center-of-mass system of coordinates. This expression is derived in terms of the center-of-mass scattering angle because, in general, the probability distribution of the scattering angle has a simpler functional form in the center-of-mass system than in the laboratory system. The energies in this last equation, however, are measured in the laboratory system.

APPENDIX C

Energy Change in Iron Elastic Scattering Events

When the nuclear mass is relatively large, an alternate equation for the energy change in elastic scattering events may be derived which is more convenient to use than that presented in Appendix B.

Taking the square root on both sides of the equation that was presented in Appendix B:

$$\sqrt{\frac{E_i}{E_{i-1}}} = \sqrt{\frac{1 + a^2 + 2a \cos \psi^*}{(1 + a)^2}}$$

Let

$$A = \sqrt{\frac{1 + a^2}{(1 + a)^2}}$$

$$z = \frac{2a \cos \psi^*}{1 + a^2} \quad (a = \frac{M}{m} = \text{nuclear mass/neutron mass})$$

to get

$$\frac{\sqrt{E_i}}{\sqrt{E_{i-1}}} = A\sqrt{1 + z}$$

We expand this latter expression in a Taylor's series to get, for small z,

$$\frac{\sqrt{E_i}}{\sqrt{E_{i-1}}} = A(1 + \frac{1}{2}z - \frac{1}{8}z^2)$$

with absolute error less than

$$\left|\frac{1}{16} z^3\right|$$

If the masses for iron and the neutron are substituted in these expressions, the energy change is given by

$$\frac{\sqrt{E_i}}{\sqrt{E_{i-1}}} = 0.982419 + 0.017738 \cos \psi^* - 0.000160135 \cos^2 \psi^*$$

with absolute error less than 0.00035%.

APPENDIX D

Conversion of the Center-of-Mass Scattering Angle to the Laboratory System

The vector diagram describing the velocity and scattering angle of an elastically scattered neutron is given in Figure 43.

As was shown in Appendix B, we can write,

$$V_i \cos \psi_i = V^* \cos \psi_i^* + V_c = \left(\frac{M}{M+m} \cos \psi_i^* + \frac{m}{M+m}\right) V_{i-1}$$

and

$$\frac{V_i^2}{V_{i-1}^2} = \frac{M^2 + m^2 + 2Mm \cos \psi_i^*}{(M + m)^2}$$

Therefore,

$$\cos \psi_i = \frac{1 + a \cos \psi_i^*}{\sqrt{1 + a^2 + 2a \cos \psi_i^*}}$$

where $a = M/m$ = nuclear mass/neutron mass.

APPENDIX E

Angle between a Scattered Neutron's Velocity and the Slab Normal

Consider a neutron with velocity $\vec{V}_{i-1}$ that is scattered through an angle ψ_i with resulting velocity $\vec{V}_i$ (all quantities are measured in the laboratory system of coordinates.) We define a coordinate system (x, y, z), as in Figure 44, such that x is in the direction of the normal of the array in Figure 1 and such that $\vec{V}_{i-1}$ is in the x-z plane. The velocity $\vec{V}_{i-1}$ makes an angle θ_{i-1} with the x-axis.

In general, the velocity $\vec{V}_i$ will be rotated through an azimuthal scattering angle ϕ_i about the direction of $\vec{V}_{i-1}$.

We wish to find the angle θ_i that the velocity $\vec{V}_i$ makes with the x-axis.

Consider a coordinate system (x', y', z') that is obtained by rotating the system (x, y, z) about the y-axis through an angle θ_{i-1} as in Figure 44 so that the x'-axis lies along the direction of $\vec{V}_{i-1}$. The components of $\vec{V}_i$ in the (x', y', z') system are:

$$V_{x'} = V_i \cos \psi_i$$

$$V_{y'} = V_i \sin \psi_i \sin \phi_i$$

$$V_{z'} = V_i \sin \psi_i \cos \phi_i$$

The transformation from the (x', y', z') system to the (x, y, z) system is:

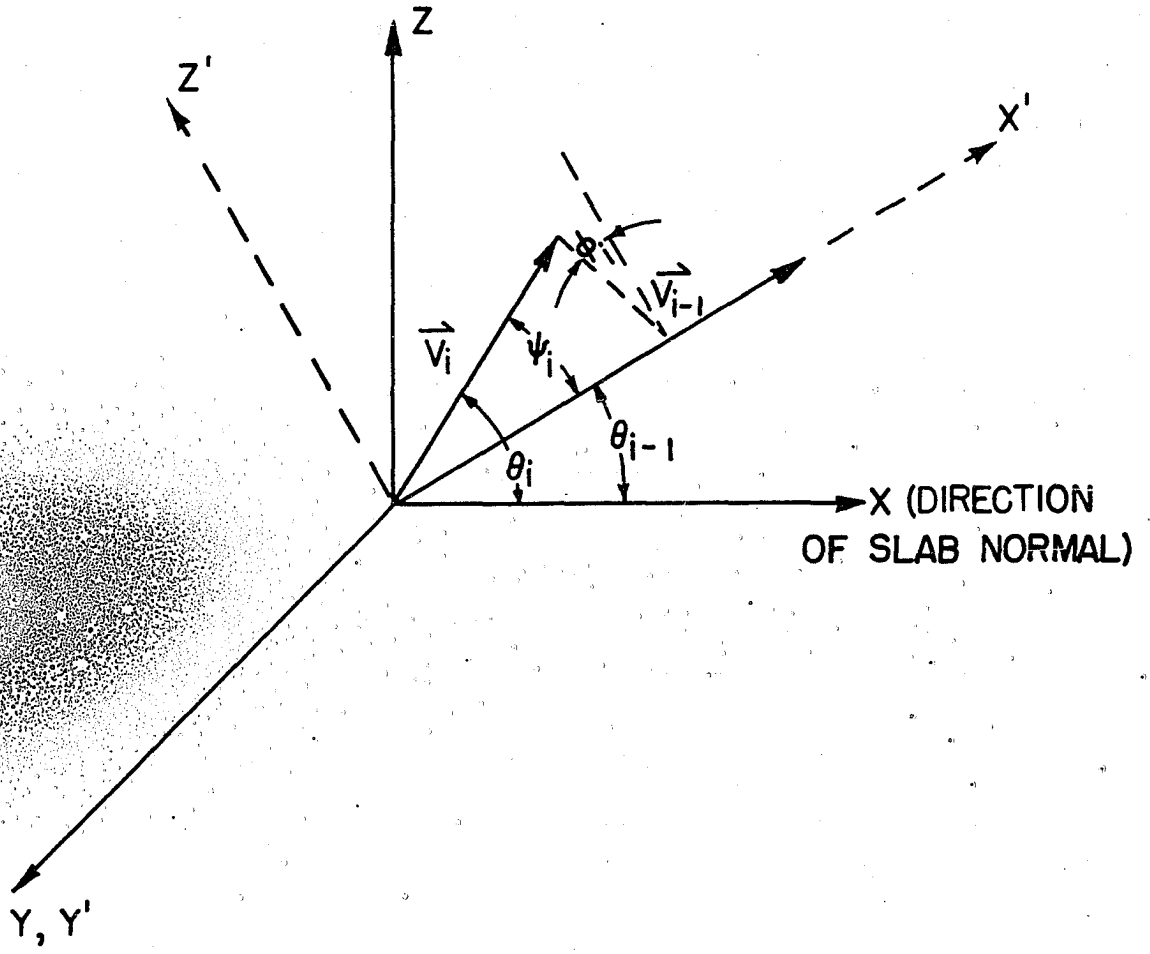

Figure 44. Angle between a scattered neutron's velocity and the x-axis

$$x = x' \cos \theta_{i-1} - z' \sin \theta_{i-1}$$

$$y = y'$$

$$z = x' \sin \theta_{i-1} + z' \cos \theta_{i-1}$$

Therefore,

$$V_x = V_{x'} \cos \theta_{i-1} - V_{z'} \sin \theta_{i-1}$$

$$V_y = V_{y'}$$

$$V_z = V_{x'} \sin \theta_{i-1} + V_{z'} \cos \theta_{i-1}$$

Substituting for $V_{x'}$, $V_{y'}$, and $V_{z'}$,

$$V_x = V_i \cos \psi_i \cos \theta_{i-1} - V_i \sin \psi_i \sin \theta_{i-1} \cos \phi_i$$

$$V_y = V_i \sin \psi_i \sin \phi_i$$

$$V_z = V_i \cos \psi_i \sin \theta_{i-1} + V_i \sin \psi_i \cos \theta_{i-1} \cos \phi_i$$

The cosine of θ_i is given by

$$\cos \theta_i = \frac{V_x}{V_i} = \cos \psi_i \cos \theta_{i-1} - \sin \psi_i \sin \theta_{i-1} \cos \phi_i$$

Note that, if ϕ_i is random on $(0, 2\pi)$, we may use equally well

$$\cos \theta_i = \cos \psi_i \cos \theta_{i-1} + \sin \psi_i \sin \theta_{i-1} \cos \phi_i$$

APPENDIX F

Probability Distribution for the Cosine of an Anisotropic Scattering Angle

Differential elastic scattering cross sections for this study were obtained from compilations made by Nuclear Development Corporation of America (13), (28). The angular distribution data in these compilations are represented in the form of Legendre expansion coefficients, f_L, defined by

$$\sigma_n(E, \psi^*) = \lambda\!\!\!^{-2} \sum_{L=0}^{\infty} \frac{(2L+1)}{2} f_L'(E) P_L(\cos \psi^*)$$

where

$\sigma_n(E,\psi^*)$ = differential elastic scattering cross section in the center-of-mass coordinate system (barns/steradian)

$\lambda\!\!\!^{-}$ = the de Broglie wave-length of the incident neutron divided by 2π

$P_L(x)$ = Legendre polynomial of order

$$L = \sum_{j=0}^{L} \frac{(-1)^j (2L - 2j)!}{2^L j!(L-j)(L-2j)!} x^{L-2j}$$

$$f_L = f_L'/f_o'$$

$$f_o' = \sigma_T(E)/2\pi\lambda\!\!\!^{-2}$$

Thus,

$$\sigma_n(E,\psi^*) = \frac{\sigma_T(E)}{2\pi} \sum_{L=0}^{\infty} \frac{(2L+1)}{2} f_L(E) P_L(\cos \psi^*) =$$

$$\frac{\sigma_T(E)}{4\pi} \sum_{L=0}^{\infty} (2L+1) f_L(E) P_L(\cos \psi^*)$$

We can transform this differential cross section expansion into a probability distribution for the cosine of the scattering angle as follows:

From the definition of the differential scattering cross-section we must have

$$\sigma_T(E) = \int_{\substack{\text{total} \\ \text{solid} \\ \text{angle}}} \sigma_n(E,\psi^*)\, d\Omega = 2\pi \int_0^{\pi} \sigma_n(E,\psi^*) \sin \psi^* d\psi^*$$

$$= \frac{\sigma_T(E)}{2} \int_{-1}^{1} \sum_{L=1}^{\infty} (2L+1) f_L(E) P_L(\cos \psi^*) d \cos \psi^*$$

$$= \frac{\sigma_T(E)}{2} \sum_{L=0}^{\infty} (2L+1) f_L(E) \int_{-1}^{1} P_L(\cos \psi^*)\, d \cos \psi^*$$

The last step in this equation is permissable because of the convergence properties of the Legendre polynomials.

It is easily shown that

$$\int_{-1}^{1} P_L(x) dx = 0 \text{ for } L \neq 0$$

$$= 2 \text{ for } L = 0$$

Therefore,

$$\sigma_T(E) = \sigma_T(E)/f_o$$

or,

$$f_o = 1$$

Thus, the probability density function for cos ψ^* is:

$$p(\cos \psi^*) = \frac{2\pi}{\sigma_T(E)} \sigma_n(E, \cos \psi^*) = \frac{1}{2} \sum_{L=0}^{\infty} (2L+1) f_L(E) P_L(\cos \psi^*)$$

Note that

$$\int_{-1}^{1} p(\cos \psi^*) \, d \cos \psi^* = 1$$

For energies in the range of interest in the present study (0 to 4.5 Mev), the differential cross section expansions were limited to a maximum of nine terms (13); i.e.,

$$p(\cos \psi^*) = \frac{1}{2} \sum_{L=0}^{8} (2L+1) f_L(E) P_L (\cos \psi^*)$$

This equation was put in the following more convenient form for use in the calculations.

$$p(x) = \sum_{j=0}^{8} A_j x^j$$

where $$x = \cos \psi^*$$

The first nine Legendre polynomials and the corresponding coefficients, A_j, used in the calculations are as follows:

$$P_o(x) = 1$$

$$P_1(x) = x$$

$$P_2(x) = \frac{1}{2} (3x^2 - 1)$$

$$P_3(x) = \frac{1}{2} (5x^3 - 3x)$$

$$P_4(x) = \frac{1}{8}(35x^4 - 30x^2 + 3)$$

$$P_5(x) = \frac{1}{8}(63x^5 - 70x^3 + 15x)$$

$$P_6(x) = \frac{1}{16}(231x^6 - 315x^4 + 105x^2 - 5)$$

$$P_7(x) = \frac{1}{16}(429x^7 - 693x^5 + 313x^3 - 35x)$$

$$P_8(x) = \frac{1}{128}(6435x^8 - 12{,}012x^6 + 6930x^4 - 1260x^2 + 35)$$

$$A_0 = (\frac{1}{2} f_0 + \frac{27}{16} f_4 + \frac{595}{256} f_8) - (\frac{5}{4} f_2 + \frac{65}{32} f_6)$$

$$A_1 = (\frac{3}{2} f_1 + \frac{165}{16} f_5) - (\frac{21}{4} f_3 + \frac{525}{32} f_7)$$

$$A_2 = (\frac{15}{4} f_2 + \frac{1365}{32} f_6) - (\frac{270}{16} f_4 + \frac{21{,}420}{256} f_8)$$

$$A_3 = (\frac{35}{4} f_3 + \frac{4725}{32} f_7) - \frac{770}{16} f_5$$

$$A_4 = (\frac{315}{16} f_4 + \frac{117{,}810}{256} f_8) - \frac{4095}{32} f_6$$

$$A_5 = \frac{693}{16} f_5 - \frac{10{,}395}{32} f_7$$

$$A_6 = \frac{3003}{32} f_6 - \frac{204{,}204}{256} f_8$$

$$A_7 = \frac{6435}{32} f_7$$

$$A_8 = \frac{109{,}395}{256} f_8$$

APPENDIX G

Random Samples from the Maxwellian Velocity Distribution

The velocities of the molecules of an ideal gas at thermal equilibrium will be distributed according to the Maxwell velocity distribution (18),

$$p(V)\,dV = \frac{n(V)}{n}\,dV = 4\pi\left(\frac{M}{2\pi k_B T}\right)^{3/2} V^2 e^{-MV^2/2k_B T}\,dV \quad \text{(G.1)}$$

where n is the total number of particles per unit volume, $n(V)\,dV$ is the number of particles per unit volume with velocities between V and V + dV, and p(V) is the probability density function for the velocity V.

Consider the problem of selecting random samples from this distribution. Define a variable, X, by

$$X = \sqrt{\frac{M}{2k_B T}}\,V$$

The probability density function for X is obtained by substituting for V in equation G.1.

$$p(X) = \frac{4}{\sqrt{\pi}}\,X^2\,e^{-X^2}\,dX$$

Now, we truncate this distribution at X = 3.2 (i.e., we neglect the less than 0.03% of the velocities that lie beyond this point), and divide the X axis from 0 to 3.2 into 16 intervals of 0.2 each. The probability that X will lie in a given interval, $X_{i-1} \leq X \leq X_i$, is

$$P_i = C_i - C_{i-1} = \int_0^{X_i} p(X)\,dX - \int_0^{X_{i-1}} p(X)\,dX$$

where

$$C_i = \int_0^{X_i} p(X)\,dX$$

is the cumulative distribution at X_i.

Table 18 gives the cumulative distribution for each of the X divisions (22).

Table 18. Cumulative distribution, $C_i = \int_0^{X_i} p(X)\,dX$, for the density function $p(X) = \frac{4}{\sqrt{\pi}} X^2 e^{-X^2}$

X_i	C_i
0.2	0.01735
0.4	0.07890
0.6	0.19226
0.8	0.34459
1.0	0.51064
1.2	0.66464
1.4	0.78926
1.6	0.87859
1.8	0.93587
2.0	0.96894
2.2	0.98621
2.4	0.99440
2.6	0.99794
2.8	0.99933
3.0	0.99984
3.2	0.99999

A random sample is picked from the distribution G.1 by comparing a random number, R_3, from the interval (0, 1), with the cumulative distributions in Table 18. The X value that

corresponds to the first C_i that is larger than or equal to R_3 is a random sample from the X distribution. Note that since $P(R \leq R_3) = R_3$ each X is selected with the correct probability. The corresponding random sample, V_i, from the distribution G.1 is given by

$$V_i = \sqrt{\frac{2k_B T}{M}} X_i$$

If the particles involved have mass M in amu, and T is given in °K

$$V_i = 0.0012897 \sqrt{\frac{T}{M}} X_i$$

where V is in units of 10^5 meters per second. (This unit for V was chosen for convenience in the fixed point calculations with the IBM-650 program).

APPENDIX H

Energy and Direction Changes for Elastic Scattering at Low Energies

When a neutron-nucleus elastic scattering event occurs at a neutron energy such that the neutron's velocity is comparable to the velocity of the bombarded nucleus due to its thermal motion, the equations presented in Appendices B, C, D, and E are no longer valid. At such energies, it becomes necessary to take into account the velocity of the nucleus and to correct for the chemical binding effects that become relatively more important as the energy of the incident neutron decreases.

The following modifications in the elastic scattering treatment used at higher energies (Appendices B to E) were suggested by J. R. Triplett et al. (14a), (22) for elastic scattering events at thermal energies.

First, a correction is made for the effect of chemical binding by allowing the effective nuclear mass to increase with decreasing energy of the incident neutron.

In addition a velocity increment, ΔV, is added vectorially to the scattered neutron's center-of-mass velocity as determined in the manner of Appendix B. This velocity increment is isotropically directed in the center-of-mass system of coordinates and has a magnitude selected at random from the Maxwellian velocity distribution for the particular nucleus

involved in the collision. The vector diagram for this process is shown in Figure 45. The outgoing neutron's velocity is taken to be the resultant of this addition. The following definitions will be used:

x = the direction of the slab normal

$\vec{V}$ = the lab system velocity of the incident neutron (y and z are chosen such that $\vec{V}$ is in the x-z plane)

$\vec{V}_c$ = the velocity, as measured in the lab system of coordinates, of the neutron-nucleus center of mass

θ_{i-1} = the angle that the incoming neutron's velocity makes with the slab normal

$\vec{V}_n$ = the outgoing neutron's lab system velocity as determined with the method of Appendix B

$\vec{V}_n^*$ = the outgoing neutron's velocity (via Appendix B) as measured in the center-of-mass system

$\vec{\Delta V}$ = the velocity increment added to $\vec{V}_n^*$ to correct for the nuclear thermal motion

$\vec{V}_e$ = the emergent neutron's velocity as measured in the lab system

θ_i = the angle between $\vec{V}_e$ and the x-axis

ψ = the angle between $\vec{V}$ and $\vec{V}_n$

ψ^* = the angle between $\vec{V}$ and $\vec{V}_n^*$

The direction cosines of $\vec{V}_c$ are:

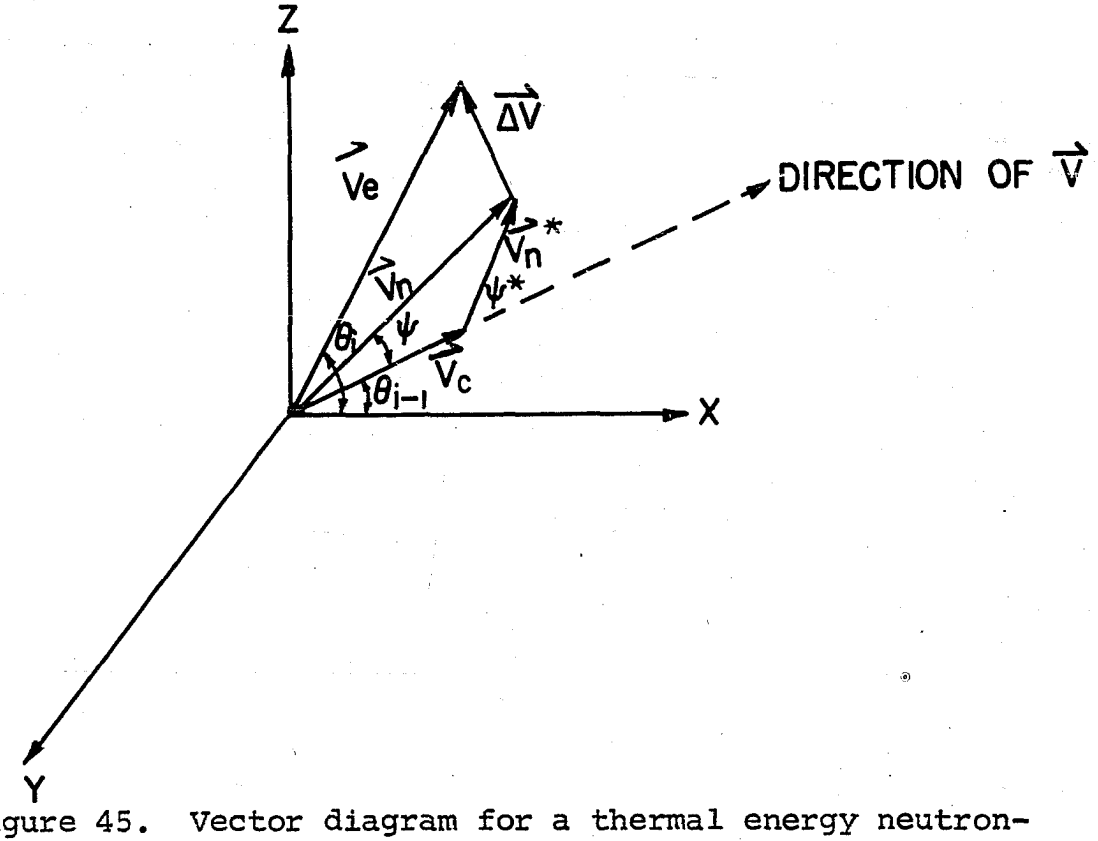

Figure 45. Vector diagram for a thermal energy neutron-nucleus collision

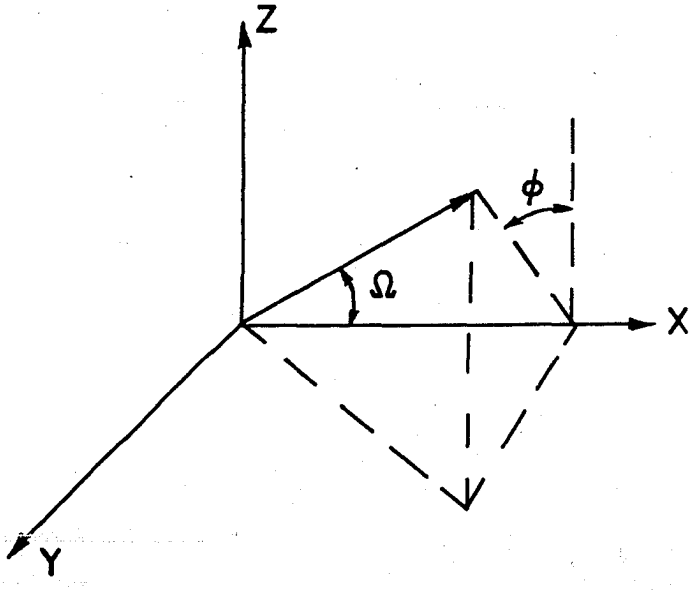

Figure 46. Two-angle designation of an isotropically distributed direction

$$\alpha = \cos \theta_{i-1}$$

$$\beta = 0$$

$$\gamma = \sin \theta_{i-1}$$

Elastic scattering at low energies (with the method of Appendix B) is isotropic in the center-of-mass system of coordinates. Therefore, the direction of $\vec{V}_n^*$ can be specified by an angle, Ω, the cosine of which is uniformly distributed on (-1, 1), and an azimuthal angle, ϕ, that is uniformly distributed on (0, 2π) (see Figure 46). The direction cosines of $\vec{V}_n^*$ are thus specified by

$$\alpha'' = \cos\Omega = 2R_1 - 1$$

$$\beta'' = \sin\Omega \sin \phi = \sqrt{1-(2R_1-1)^2} \sin \phi$$

$$\gamma'' = \sin\Omega \cos \phi = \sqrt{1-(2R_1-1)^2} \cos \phi$$

where R_1 is a number chosen at random from the interval (0, 1) and ϕ is selected at random from (0, 2π).

The incremental velocity, $\vec{\Delta V}$, is also isotropically directed in the center-of-mass system and its direction cosines are specified by

$$\alpha''' = 2R_2 - 1$$

$$\beta''' = \sqrt{1-(2R_2-1)^2} \sin \omega$$

$$\gamma''' = \sqrt{1-(2R_2-1)^2} \cos \omega$$

where R_2 is random on (0, 1) and ω is random on (0, 2π).

The magnitude of $\vec{\Delta V}$ is given by (Appendix G)

$$\Delta V = 0.0012897 \sqrt{\frac{T}{M}} \; X$$

where T is the temperature (°K), M is the mass of the nucleus (amu), and X is chosen at random from a probability table as described in Appendix G.

We can now make the vector addition.

The cosine of the angle between $\vec{V}$ and $\vec{V}_n^*$ is given by

$$\mu = \cos \psi^* = \alpha\alpha'' + \beta\beta'' + \gamma\gamma''$$

Let α', β', γ' be the direction cosines of $\vec{V}_n$.

From Appendix B,

$$V_c = \frac{mV}{M+m} = \frac{V}{1+a}$$

$$V_n^* = \frac{MV}{M+m} = \frac{aV}{1+a}$$

$$V_n = \frac{V\sqrt{1+a^2+2a\mu}}{1+a} = \frac{VC}{1+a}$$

where

$$C = \sqrt{1+a^2+2a\mu}$$

$$a = \frac{M}{m} = \text{nuclear mass/neutron mass}$$

Equating components along the x-axis,

$$V_n \alpha' = V_c \alpha + V_n^* \alpha''$$

Therefore

$$\alpha' = \frac{V_c}{V_n}\alpha + \frac{V^*}{V_n}\alpha'' = \frac{\alpha + a\alpha''}{C}$$

Similarly,

$$\beta' = \frac{\beta+a\beta''}{C}$$

$$\gamma' = \frac{\gamma+a\gamma''}{C}$$

The vectors $\vec{V}_n$ and $\Delta\vec{V}$ can now be written in the following form:

$$\vec{V}_n = (V_n\alpha', V_n\beta', V_n\gamma') =$$

$$\frac{V_n}{c} (\alpha + a\alpha'', \beta + a\beta'', \gamma + a\gamma'')$$

$$\vec{\Delta V} = (\Delta V\alpha''', \Delta V\beta''', \Delta V\gamma''')$$

The resultant vector, $\vec{V}_e$, is, therefore

$$\vec{V}_e = (V_{e_x}, V_{e_y}, V_{e_z}) = \vec{V}_n + \vec{\Delta V}$$

where

$$V_{e_x} = \frac{V_n}{c} (\alpha + a\alpha'') + \Delta V\alpha'''$$

$$V_{e_y} = \frac{V_n}{c} (\beta + a\beta'') + \Delta V\beta'''$$

$$V_{e_z} = \frac{V_n}{c} (\gamma + a\gamma'') + \Delta V\gamma'''$$

The magnitude of $\vec{V}_e$ is given by

$$V_e^2 = V_{e_x}^2 + V_{e_y}^2 + V_{e_z}^2 = \frac{V^2c^2}{(1+a)^2} + \Delta V^2 + \frac{2V\Delta V}{1+a} [(\alpha+a\alpha'')\alpha''' +$$

$$(\beta+a\beta'')\beta''' + (\gamma+a\gamma'')\gamma''']$$

To find the angle between $\vec{V}_e$ and the x-axis, we equate components along the x-axis,

$$V_e \cos \Theta_i = V_n\alpha' + \Delta V\alpha'''$$

or finally,

$$\cos \Theta_i = [\frac{V(\alpha + a\alpha'')}{1 + a} + \Delta V\alpha'''] / V_e$$

These equations, with the appropriate effective mass for the nucleus, were used to establish energy and direction changes for neutron collisions at thermal energies.

In the present calculations, the nuclear mass was con-

sidered to be a function of the incident neutron's energy only for the case of hydrogen collisions. Collisions with iron will in general, change the direction, but will not drastically affect the energy (some exceptions to this occur at very low energies). Furthermore, the large capture cross section of iron, particularly at very low energies, means that the number of low energy iron collisions is relatively small. The low total cross section of oxygen compared to hydrogen also assures that the fraction of low energy collisions that are with oxygen is small. Thus, neglecting the chemical binding effects in thermal collisions with iron and oxygen should introduce only small errors.

On the other hand the increase of the effective mass of hydrogen with decreasing neutron energy must be taken into account. As discussed in detail in the main part of this paper, the effective mass scheme that seemed to give the best results in the calculations was approximately the following:

$$M_H = 2a_H - 1$$

where M_H is the effective mass that was used for hydrogen and a_H is the effective proton mass reported in reference (23). A graph of a_H at 298°K is given as a function of incident neutron energy in Figure 47 (22).

In summary, the energy and direction changes for collision number i occurring at low energy are given by

$$E_i = \tfrac{1}{2} m V_e^2$$

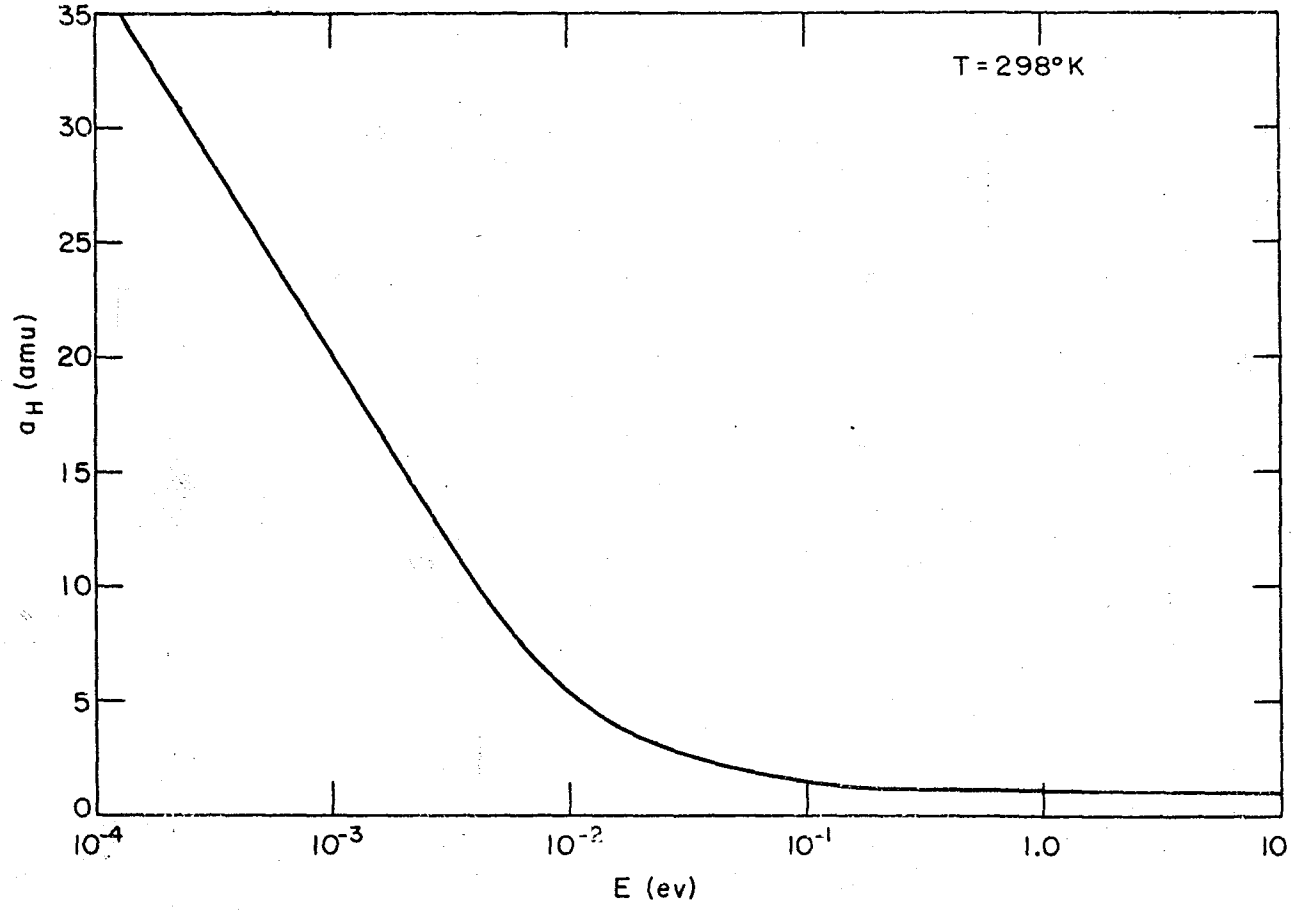

Figure 47. Effective scattering mass of proton in water vs neutron energy

$$V_e^2 = \frac{V^2C^2}{(1+a)^2} + \Delta V^2 + \frac{2V\Delta V}{1+a}\left[(\alpha + a\alpha'')\alpha''' + (\beta + a\beta'')\beta''' + (\gamma + a\gamma'')\gamma'''\right]$$

$$\cos\theta_i = \left[\frac{V(\alpha + a\alpha'')}{1+a} + \Delta V\alpha'''\right]/V_e$$

$$V^2 = \frac{2E_{i-1}}{m}$$

$$\alpha = \cos\theta_{i-1}$$

$$\beta = 0$$

$$\gamma = \sin\theta_{i-1}$$

$$\alpha'' = 2R_1 - 1$$

$$\beta'' = \sqrt{1 - (\alpha'')^2}\sin\phi$$

$$\gamma'' = \sqrt{1 - (\alpha'')^2}\cos\phi$$

$$\alpha''' = 2R_2 - 1$$

$$\beta''' = \sqrt{1 - (\alpha''')^2}\sin\omega$$

$$\gamma''' = \sqrt{1 - (\alpha''')^2}\cos\omega$$

$$C^2 = 1 + a^2 + 2a\mu$$

$$\mu = \alpha\alpha'' + \beta\beta'' + \gamma\gamma''$$

$$\Delta V = 0.0012897\sqrt{\frac{T}{M}}\ X$$

where R_1 and R_2 are random numbers from (0, 1), ϕ and ω are random angles from (0, 2π), and X is a random variable selected from a probability table as described in Appendix G.

APPENDIX I

Rejection Technique for Picking Random Samples from a Distribution

Consider a random variable X, $a \leq X \leq b$, with probability distribution function $y = f(x)$ defined on the interval (a, b) as shown in Figure 48. Assume that it is desired to select random samples of X such that the selected samples will have the distribution f(x) as the number of samples becomes large. The following rejection method for doing this was proposed by von Neumann (4).

1. Define a rectangle that completely contains f(x), such as the rectangle M'ab in Figure 48.
2. Select a point (X, Y) at random from this rectangle.
3. If Y is smaller than f(X), accept X as a sample from f(x). If Y lies above f(X), reject X and repeat 2 and 3.

To see that the accepted values of X have the proper distribution, we consider the probability of obtaining and accepting a given X value. If the point in step 2 is selected at random, the abscissa will be uniformly distributed on (a, b) and the ordinate will be uniformly distributed on (0, M'). The probability of selecting an X value that is in a small interval Δx is clearly $\Delta x/(b-a)$, while the probability that the selected ordinate will lie below f(X) is simply $f(X)/M'$. The probability of selecting an X in Δx at x and of accepting

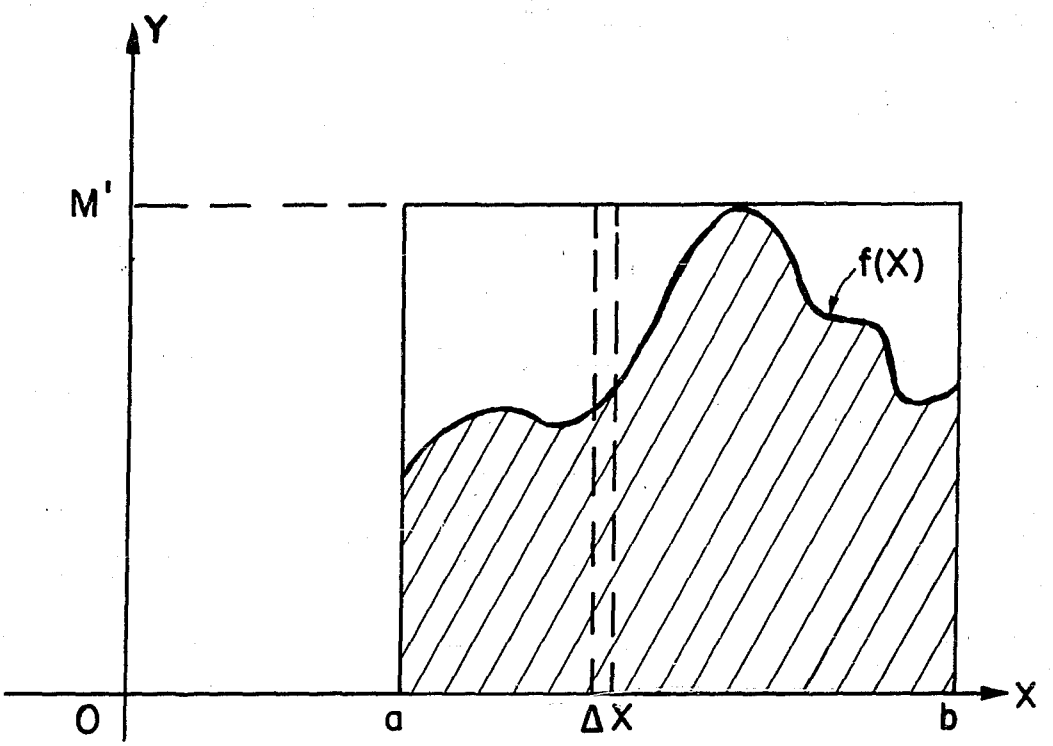

Figure 48. Rejection technique for picking random samples from a distribution

this value is given by the product of these two independent probabilities or

P(selecting X in Δx at x and accepting it as a sample) = $f(X)\ \Delta x/M'(b-a)$

i.e., the acceptance probability is proportional to f(X). Therefore, the accepted values will have the distribution f(x) as the number of samples becomes large.

The rejection technique was used in the present study to select the cosine of the scattering angle in anisotropic elastic scattering events. The probability distribution for the cosine of the scattering angle (in the center-of-mass system of coordinates) when a neutron of energy E_{i-1} suffers an anisotropic scattering event is given by

$$p(\cos \psi_i^*) = \sum_{k=1}^{K} A_k(E_{i-1}) \cos^k \psi_i^*$$

The rejection method for picking a cosine from this distribution is as follows:

1. Let M' = the maximum value of $p(\cos \psi_i^*)$ for $-1 \leq \cos \psi_i^* \leq 1$.
2. Select two random numbers R_1 and R_2 from the interval (0, 1).
3. Let $X = 2R_1 - 1$
4. Calculate $p(X) = \sum_{k=1}^{K} A_k X^k$
5. If $M'R_2 \leq p(X)$, let $\cos \psi_i^* = X$. If $M'R_2 > p(X)$, repeat steps 2 through 5.

Obviously, the utility of this method depends upon its efficiency, i.e., upon the average number of trials that must be made in order to obtain a sample. The average number of trials per sample may be derived as follows (6).

The probability that a given trial will be successful or the probability that the randomly selected point will lie in the shaded area of Figure 48, is equal to the ratio of the area of the shaded portion of Figure 48 to the area of the rectangle M'-a-b, i.e.,

$$P(\text{success in one trial}) = \int_a^b f(x)\,dx/M'(b-a) = E$$

Since f(x) is a probability density function,

$$\int_a^b f(x)\,dx = 1$$

Therefore,

$$E = \frac{1}{M'(b-a)}$$

and the probability that a given trial will fail is 1-E.

We may now write the probability of n-1 failures followed by a success, i.e., the probability of n trials for a sample of X.

$P(n) = (1-E)^{n-1}E$ = the probability density function for the number of trials needed to obtain an X

The expected number of trials needed to obtain an X value from f(x) is, therefore,

$$\bar{n} = \sum_{n=1}^{\infty} np(n) = \sum_{n=1}^{\infty} nE(1-E)^{n-1} = \sum_{n=1}^{\infty} -E \frac{d(1-E)^n}{dE}$$

$$= -E \frac{d}{dE} \sum_{n=1}^{\infty} (1-E)^n$$

Now,

$$\sum_{n=1}^{\infty} (1-E)^n = \frac{1}{1-(1-E)} - 1 = \frac{1-E}{E}$$

and the expected number of trials is:

$$\bar{n} = -E \frac{d}{dE} \left(\frac{1-E}{E}\right) = \frac{1}{E} = M'(b-a)$$

In selecting cosines of scattering angles in the present work, the expected number of trials was between 1 and 14, depending upon the material and the energy of the incident neutron. The majority of selections had an expected number of trials between 1.5 and 4.

APPENDIX J

Generation of Cosines of Angles That Are Random on $(0, 2\pi)$

The azimuthal angle, ϕ, in a neutron scattering event usually is assumed to be uniformly distributed between 0 and 2π. One obvious method of obtaining such a random angle would be to let $\phi = 2\pi R$, where R is random on (0, 1). However, since only the cosine of the azimuthal angle is required in the present calculations, we can make use of a convenient technique suggested by von Neumann (4) to circumvent the lengthy cosine sub-routine. The method proceeds as follows:

1. Choose two numbers, r_1 and r_2, at random from (0, 1).
2. If $r_1^2 + r_2^2 > 1$, reject r_1 and r_2 and select two new random numbers.
3. If $r_1^2 + r_2^2 \leq 1$, let $\cos \phi = c \dfrac{2r_1 r_2}{r_1^2 + r_2^2}$

where c is plus or minus one with probability 1/2. The efficiency of this process is $\frac{\pi}{4}$. The resulting population of cosines will have the same distribution as the cosines of angles chosen at random from $(0, 2\pi)$.

This method was used to prepare a table of approximately 150,000 cosines of random angles. The random numbers employed were from the RAND table of random digits (14b). Each random number consisted of six digits. When the RAND table was exhausted, the random digit cards were put in random order by

sorting on four random digits (not used in the calculations) in each card. The digits from each card then were put in random order as they entered the IBM-650 via control panel wiring, and the RAND table was reused to calculate a new set of cosines. The cosines were punched out 10 per card in the form .xxxxxxx on standard IBM cards. Two of these cosines were punched into each random input card to be used as cos ϕ and cos ω as described earlier.

Chi-squared and Kolmogorov-Smirnov goodness-of-fit tests were made, as described in Appendix A, for the cosines. The results of these tests are shown in Tables 19 and 20.

Table 19. Chi-squared goodness-of-fit test of cosine deviates (k=21)

Deviates	$-2 \log \lambda$	$P(-2 \log \lambda' \geq -2 \log \lambda)$
1-25,000	7.79	0.98
25,000-50,000	8.01	0.97
50,000-75,000	13.21	0.86
75,000-100,000	7.68	0.98
100,000-150,000	8.37	0.97

Table 20. Kolmogorov-Smirnov goodness-of-fit test of cosine deviates

Deviates	Maximum deviation of sample	Maximum deviation at 5% significance level
1-25,000	0.0058	0.0083
25,000-50,000	0.0030	0.0083
50,000-75,000	0.0074	0.0083
75,000-100,000	0.0047	0.0083
100,000-150,000	0.0023	0.00626

APPENDIX K

Emission Probabilities for Iron Inelastic Scattering Gamma-Rays

Inelastic scattering occurs in iron at incident neutron energies above 0.85 Mev. In such events kinetic energy is not conserved. The incident neutron is absorbed by the nucleus and immediately re-emitted with substantially reduced energy. The energy lost by the neutron leaves the nucleus in an excited state. The excitation energy of this nucleus then is given off in the form of gamma-rays.

Cross sections for the production of inelastic scattering gamma-rays in iron have been compiled by Nuclear Development Corporation (13). These cross sections were used to prepare a table of emission probabilities as a function of incident neutron energy for the six inelastic scattering gammas of interest in this study (energies less than 5 Mev). The probability of emission for a given gamma-ray of energy E_γ is given by

$$P(E_\gamma) = \frac{\sigma_\gamma(E_{i-1})}{\sigma_{in}(E_{i-1})}$$

where σ_γ is the cross section for production of the gamma-ray, σ_{in} is the total inelastic scattering cross section for iron, and E_{i-1} is the energy of the incident neutron. The resulting probabilities are given in Table 21.

The energy range in which iron inelastic scattering

Table 21. Emission probabilities for iron inelastic scattering gamma-rays (13)

Energy of incident neutron (Mev)	Gamma energy (Mev)					
	0.845	2.09	2.66	2.95	3.01	3.38
0.897	1.0000	0	0	0	0	0
0.943	1.0000					
0.991	1.0000					
1.042	1.0000					
1.096	1.0000					
1.15	1.0000					
1.21	1.0000					
1.27	1.0000					
1.34	1.0000					
1.41	1.0000					
1.48	1.0000					
1.55	1.0000					
1.63	1.0000					
1.72	1.0000					
1.81	1.0000					
1.90	1.0000					
2.00	1.0000					
2.10	1.0000					
2.21	0.9989	0.0011				
2.32	0.9927	0.0073				
2.44	0.9810	0.0190				
2.56	0.9634	0.0366				
2.69	0.8303	0.0648	0.1049			
2.83	0.7354	0.0987	0.1659			
2.97	0.6123	0.1379	0.1946	0.0552		
3.13	0.5333	0.1630	0.2148	0.0859	0.0030	
3.29	0.4796	0.1828	0.2250	0.0985	0.0141	
3.46	0.4357	0.1941	0.2276	0.1084	0.0201	0.0141
3.64	0.4129	0.2017	0.2219	0.1150	0.0215	0.0269
3.82	0.4046	0.2075	0.2006	0.1196	0.0277	0.0401
4.02	0.3978	0.2079	0.1792	0.1290	0.0287	0.0573
4.23	0.4049	0.2055	0.1484	0.1408	0.0342	0.0662
4.44	0.4061	0.2070	0.1210	0.1553	0.0390	0.0717
4.67	0.4080	0.1998	0.0941	0.1707	0.0458	0.0816

occurs was broken up into six intervals or groups. Table 21 was then used to prepare a set of inelastic gamma-ray emission probabilities for each energy group. Each of these sets includes, of course, only those inelastic scattering gammas that are possible for the given energy group. These probabilities are given in Table 22.

Table 22. Averaged emission probabilities for iron inelastic scattering gamma-rays

Energy of incident neutron (Mev)	Gamma energy (Mev)					
	0.845	2.09	2.66	2.95	3.01	3.38
0-2.21	1.0000	0	0	0	0	0
2.21-2.69	0.9840	0.0160	0	0	0	0
2.69-2.97	0.7828	0.0718	0.1354	0	0	0
2.97-3.13	0.6123	0.1379	0.1946	0.0552	0	0
3.13-3.46	0.5065	0.1729	0.2199	0.0922	0.0085	0
3.46-4.02	0.4128	0.2028	0.2073	0.1180	0.0245	0.0346
4.02-4.65	0.4063	0.2040	0.1212	0.1556	0.0397	0.0732

Table 22 was used, as described in the program section, to select the energy change, E_γ, in iron inelastic scattering events.

APPENDIX L

Cross Section Data

Most of the cross section data that were used in this study were obtained from a comprehensive compilation that has been made by the Nuclear Development Corporation of America (13), (28). In the NDA work, the energy range between 100 ev and 4.67 Mev was divided into 215 intervals. The following data from this compilation, in the energy range 100 ev to 4.67 Mev, were used in the present study:

Iron: Total cross section, inelastic scattering cross section, radiative capture cross section, inelastic scattering gamma-ray production cross sections, expansion coefficients for the differential elastic scattering cross section (see Appendix F)

Oxygen: Total cross section, expansion coefficients for the differential elastic scattering cross section (see Appendix F)

The total cross section for hydrogen at all energies and the total cross sections for iron and water at thermal energies were obtained from (15). At energies above 1 ev the total cross section for water was assumed to be equal to the sum of the cross sections for the hydrogen and oxygen nuclei in water.

The radiative capture cross section for hydrogen was

assumed to vary inversely as the square root of the incident neutron's energy (1/V variation) from a value of 0.33 barns at 0.025 ev (15). The capture cross section of iron for incident neutron energies of 0 to 100 ev was assumed to vary as $1/V$ from a value of 2.53 barns at 0.025 ev (15). The capture cross section for oxygen is negligible at all energies.

The energy range from 0 to 100 ev was broken up into 20 groups for the hydrogen data and into 9 groups for the other data. These low energy groups were not changed in the group combinations that will now be described.

For each of the energy groups that have been described (215 from the NDA compilation, plus 20 for hydrogen data and 9 for other data), the following constants were calculated:

1. The expansion coefficients, A_j (see Appendix F), for the differential elastic scattering probabilities of iron and oxygen.

2. The maximum values, M', of the differential elastic scattering probabilities for iron and oxygen (see Appendix I).

3. The macroscopic total cross sections for iron and water.

4. The capture probabilities for hydrogen and iron (capture probability = capture cross section/total cross section) at energies above thermal.

5. The inelastic scattering probability for iron (inelastic scattering probability = inelastic scattering cross

section/total cross section).

A tabulation of these data was made and on the basis of this table, 128 of the energy groups were combined with the remaining 96 in such a manner so that the variation of the cross section data over the range of each energy interval was small. This combination resulted in a tabulation of the data in 96 energy groups from 0 to 4.67 Mev for all of the data except those for hydrogen. The hydrogen data were tabulated into 107 energy groups (because of the larger number of thermal groups for the hydrogen data). These final tabulations were the ones used in the program.

The final data tabulations were used to establish the following energy regions in which the elastic scattering angle distributions, $p(\cos \psi^*)$, have different functional forms (see Appendix F):

Iron: $E_{i-1} < 0.0221$ Mev $= E_{iso_{Fe}}$, elastic scattering is isotropic in the center-of-mass coordinate system, i.e., $p(\cos \psi^*) = \frac{1}{2}$

$E_{iso_{Fe}} < E_{i-1} < 0.601$ Mev $= E_{II_{Fe}}$, $p(\cos \psi^*) = \sum_{j=0}^{3} A_j \cos^j \psi^*$

$E_{i-1} > E_{II_{Fe}} = 0.601$ Mev, $p(\cos \psi^*) = \sum_{j=0}^{8} A_j \cos^j \psi^*$

Oxygen: $E_{i-1} < 0.172$ Mev $= E_{iso_O}$, scattering is isotropic in the center-of-mass system, i.e., $p(\cos \psi^*) = \frac{1}{2}$

$$E_{iso_0} < E_{i-1} < 3.29 \text{ Mev} = E_{II_0},\ p(\cos \psi^*) = \sum_{j=0}^{3} A_j \cos^j \psi^*$$

$$E_{i-1} > E_{II_0} = 3.29 \text{ Mev},\ p(\cos \psi^*) = \sum_{j=0}^{5} A_j \cos^j \psi^*$$

where E_{i-1} is the energy of the incident neutron.

APPENDIX M

Physical Constants

Mass of the iron nucleus = 55.86400 amu (29)

Mass of the oxygen nucleus = 16.00000 amu

Mass of the proton = 1.007593 amu (18)

Mass of the neutron = 1.008982 amu (18)

Molecules of water per cubic centimeter at 298°K =

3.334×10^{22} molecules/cm^3

Atoms of iron per cubic centimeter at 298°K $\cong 1.695 \times 10^{23}$

atoms/cm^3

Boltzmann constant = $k_B = 1.38042 \times 10^{-16}$ erg/°K (18)

APPENDIX N

Curve Fitting Procedures

General remarks

Consider the problem of fitting a function, $y = p(x)$, to a set of observations, $\bar{p}(x_i)$, $i = 1$ to N. The best fit will be obtained for the set of parameters such that the following error function is minimized:

$$Q = \sum_{i=1}^{N} [y(x_i) - \bar{p}(x_i)]^2 = \sum_{i=1}^{N} [y(x_i)^2 + \bar{p}(x_i)^2 - 2y(x_i)p(x_i)]$$

$$= \sum_{i=1}^{N} [y(x_i)]^2 - 2\sum_{i=1}^{N} \bar{p}(x_i)y(x_i) + \sum_{i=1}^{N} [\bar{p}(x_i)]^2$$

where $y(x_i)$ is the value of $y = p(x)$ at $x = x_i$.

The conditions that must hold for Q to be a minimum may be written

$$\frac{\partial Q}{\partial \delta} = 2\sum_{i=1}^{N} \frac{\partial y(x_i)}{\partial \delta} y(x_i) - 2\sum_{i=1}^{N} \frac{\partial y(x_i)}{\partial \delta} \bar{p}(x_i) = 0$$

or

$$\sum_{i=1}^{N} \frac{\partial y(x_i)}{\partial \delta} [y(x_i) - \bar{p}(x_i)] = 0 \qquad \text{(N.1)}$$

where δ represents a parameter of $p(x)$. Thus, N.1 represents a set of k equations where k is equal to the number of parameters in $p(x)$. The solutions of this set of equations give the parameters for the best fit.

In general, this set of equations cannot be solved

explicitly for the best fit parameters. The methods used in the present study to obtain the best set of parameters will be discussed individually for the various functions used.

Water layers

Let $y(x_i) = A + Bx_i + Cx_i^2$. The equations N.1 are linear in A, B, and C, and the solutions for the three parameters may be obtained explicitly.

$$A = [g(bf - d^2) - a(hf - ld) + b(hd - lb)]/D$$

$$B = [N(hf - ld) - g(af - bd) + b(al - hb)]/D$$

$$C = [N(lb - hd) - a(al - hb) + g(ad - b^2)]/D$$

where

$$D = N(bf - d^2) - a(af - db) + b(ad - b^2)$$

and

$$a = \sum_{i=1}^{N} x_i$$

$$b = \sum_{i=1}^{N} x_i^2$$

$$d = \sum_{i=1}^{N} x_i^3$$

$$f = \sum_{i=1}^{N} x_i^4$$

$$g = \sum_{i=1}^{N} \bar{p}(x_i)$$

$$h = \sum_{i=1}^{N} x_i \bar{p}(x_i)$$

$$1 = \sum_{i=1}^{N} x_i^2 \bar{p}(x_i)$$

First iron layer

The function to be fitted is

$$p(x) = \alpha e^{\beta x}$$

The equations N.1 can be solved explicitly for α (because of the linearity in α), but not for β. One method of obtaining the best fit parameters is to make a first guess, β_1, for β, and to expand the function $e^{(\beta_1 + \Delta\beta)x}$ in a Taylor's series, where $\Delta\beta$ is to be found so that $\beta_1 + \Delta\beta = \beta$ = the best fit. By inserting only the first two (linear) terms of this expansion, equations N.1 can be solved for α and $\Delta\beta$. These values are approximate, of course, because of the higher order terms that are thrown out. A new guess, $\beta_2 = \beta_1 + \Delta\beta$, for β is then inserted in the place of β, and the process is repeated. Succeeding values of β_j, as the process is repeated, will converge to the best fit value for β. (Note that, given a value for β, the corresponding best α can be obtained explicitly in each instance).

Unfortunately, this method is slow. The method was employed in some of the earlier work in this study, but the convergence was inconveniently slow in most instances and almost prohibitively so in others. Therefore, a grid examination technique was used in the majority of the curve fitting calcu-

lations. (All of the curve fitting described in this appendix was done with programs written especially for this project in the FORTRANSIT coding system.) The grid method proceeds as follows:

1. A first guess for β, and initial values for a, b, and c (see below) are inserted into the program. The best fit value for α, corresponding to the first guess for β, is then calculated (via N.1) from

$$\alpha = \sum_{i=1}^{N} \bar{p}(x_i) e^{\beta x_i} / \sum_{i=1}^{N} e^{2\beta x_i}$$

and the corresponding value of Q is calculated from

$$Q = \sum_{i=1}^{N} [y(x_i) - \bar{p}(x_i)]^2$$

where $y(x_i) = \alpha e^{\beta x_i}$

2. The previous value for β is then multiplied by (1 + ab) and, using this new β, new values for α and Q are calculated.

If the new Q is smaller than the previous Q, this step (step 2) is repeated.

If the new value of Q is larger than the previous value of Q, (1 + ab) is replaced by (1 - ab) and step 2 is repeated using (1 - ab) instead of (1 + ab).

If multiplying β by both (1 + ab) and (1 - ab) leads to a larger value for Q (poorer fit), the program goes to step 3.

3. The current value of b is replaced by cb, ($0 < c < 1$), and step 2 is repeated.

This method becomes unwieldy if convergence to more than 4 or 5 significant figures is desired; however, in the present study, this method was much faster than the expansion method described previously. Calculating time required to fit ten observed points was normally between 5 and 10 minutes for four significant figures in the parameters.

Second and third iron layers

The function to be fitted is

$$p(x) = \alpha \cosh \beta(x-x_o)$$

A grid method similar to that used for the first iron layers was used in fitting this function. The method proceeds as follows:

1. First guesses for β and for x_o are inserted into the program along with values for a, b, and c. The best α is then calculated from

$$\alpha = \sum_{i=1}^{N} \bar{p}(x_i) \cosh \beta(x_i-x_o) / \sum_{i=1}^{N} \cosh^2\beta(x_i-x_o)$$

and Q is calculated from

$$Q = \sum_{i=1}^{N} [y(x_i) - \bar{p}(x_i)]^2$$

where $y(x_i) = \alpha \cosh \beta(x_i-x_o)$.

2. The previous value of β is multiplied by (1 + ab) and, using this new β, new values for α and Q are calculated.

If the new value of Q is smaller than the old value of Q, this step is repeated.

If the new value of Q is larger than the old value of Q, $(1 + ab)$ is replaced by $(1 - ab)$ and step 2 is repeated using $(1 - ab)$.

If multiplying the previous value of β by both $(1 + ab)$ and $(1 - ab)$ leads to a larger value for Q, the program goes to step 3.

3. The previous value of x_o is multiplied by $(1 + ab)$ and, using this new x_o, new values for α and Q are calculated.

If the new value for Q is smaller than the old value of Q, this step is repeated.

If the new value of Q is larger than the old value of Q, $(1 + ab)$ is replaced by $(1 - ab)$ and step 3 is repeated using $(1 - ab)$.

If multiplying the previous value of x_o by both $(1 + ab)$ and $(1 - ab)$ leads to a larger value for Q, the program goes back to step 2.

Steps 2 and 3 are repeated until all changes [via $(1 \pm ab)$] in the parameters β and x_o lead to poorer fits (larger Q). The program then goes to 4.

4. The current value of b is replaced by cb $(0 < c < 1)$ and steps 2 and 3 are repeated.

Typical computing times required with this method to obtain the best fit parameters to four significant figures for ten observed points were between 10 and 40 minutes.